Doctor of Philosophy

Effective design of promising photoanode using modified α-Fe_2O_3 thin film for improving photoelectrochemical water splitting

The Graduate School

of the University of Ulsan

Department of civil and Environmental Engineering

Zohrehsadat Masoumilari

Effective design of promising photoanode using modified α-Fe_2O_3 thin film for improving photoelectrochemical water splitting

Supervisor: Professor Lee, Byong-Kyu

A Dissertation

Submitted to

The Graduate School of the University of Ulsan in partial Fulfillment of the Requirements for the Degree of

Doctor of Philosophy in Environmental Engineering

by

Zohrehsadat Masoumilari

Department of Civil and Environmental Engineering

Ulsan, Korea

9 Dec. 2021

Effective design of promising photoanode using modified α-Fe_2O_3 thin film for improving photoelectrochemical water splitting

This certified that this dessertation of

Zohrehsadat Masoumilari is approved

Committee Chairman: .....

Prof. Seok-Young Oh

Committee Member: .....

Prof. Sung-Deuk Choi

Committee Member: .....

Prof. Eun-Woo Shin

Committee Member: .....

Prof. Hung-Suck Park

Committee Member: .....

Prof. Byeong-Kyu Lee

Department of civil and Environmental Engineering

Ulsan, South Korea
December 2021

ACKOWLEDGMENT

This Ph.D. was only possible due to the University of Ulsan, which was granted the full fund scholarship for me. I was lucky to be tutored throughout by prof. Byeong-Kyu Lee. I would like to thank my professor for availability, support, encouragement, and consideration. I would like to thank my committee members including prof. Seok-Young Oh (Chairman), Prof. Sung-Deuk Choi, Prof. Eun-Woo Shin, and Prof. Hung-Suck Park for taking time out of their busy schedule to serve in my committee, review my dissertation and provide valuable comments and suggestions on my work. I also would like to thank other professor in department of Civil & Environmental Engineering for their help and supported during my Ph.D. course. I would also like to thank member of Air Environmental and Energy Research Laboratory who kindly helped and shared their knowledge and living experience when I stayed in Korea. I would like to show my gratefulness to my mother, my sister, and my uncle for providing me with support and continuous encouragement throughout my years of study. Finally, I would like to special thanks to my husband, Meysam Tayebi, for supporting me step by step through the process of researching and writing this thesis. This accomplishment would not have been possible without them. You are my motivation for keeping moving forward.

Ulsan, December 9th, 2021

Zohrehsadat Masoumilari

Contents

Table of Figures

Abstract

Solar energy is one of the most abundant and stable natural resources, which could be an ideal alternative to traditional fossil fuels. Many research groups up today work in the production and utilization of renewable energy to replace fossil fuels. The photoelectrochemical (PEC) systems as an approaching way to address the global energy crisis can successfully convert the abundant solar energy harvesting into the storable chemical fuel. The PEC hydrogen production via water splitting can efficiently enable energy production to zero carbon emissions, which employs semiconducting materials as photoelectrodes for the direct conversion of solar energy into storable hydrogen. The photoanode used in such a system should have a suitable band position and harvest more portion of solar light spectrum along with superb stability for water oxidation while having a reasonable cost. Hematite (α-Fe_2O_3) is one of the most promising metal oxides which have been used as a photoanode in PEC cells. It is not only highly naturally abundant, environmentally friendly, and low cost, but it also has a narrow bandgap (1.9-2.2 eV) and photochemical stability. However, the drawbacks of α-Fe_2O_3 (i.e., the short hole diffusion length (L_D is around 2-4 nm) and poor conductivity) result in inconformity in the energy level of conduction band compared to the energy level of the H_2/H^+ reduction reaction. To decrease these drawbacks affecting the PEC performance of α-Fe_2O_3, various techniques have been examined. In this thesis, doping technique particularly using metals and heterojunction with other semiconductors have been widely applied to obtain improved PEC performance, and highlights the challenges faced in the design of visible light active water splitting photocatalysts.

Thesis Outline

The purpose of this thesis is the design of stable, low-cost, and efficient photoanode to improve photoelectrochemical (PEC) water splitting.

Chapter 1 contains an overall description of the fossil fuel environmental impacts, the effects of photoelectrochemical application on carbon emissions, suitable semiconductor materials for photoelectrodes, and the different modification processes to enhance the PEC performance. Further, the hematite (α-Fe_2O_3) as a photoactive material that explain the reasons of the choice. **Chapter 2** includes the role of doping molybdenum (Mo) to enhance the PEC water splitting performance of the α-Fe_2O_3 photoanode. The effect of heterojunction α-Fe_2O_3 photoanode with two-dimensional material specifically TMDs (MoS_2 nanosheets) was systematically investigated in **Chapter 3**. The complex of heterojunction with doping (W:α-Fe_2O_3/MoS_2) and multi-heterojunction (α-Fe_2O_3/$BiVO_4$/MoS_2) were studied in **Chapter 4**, which shows more effective PEC performance. Finally, **Chapter 5** concludes the research and proposes the future work.

Chapter 1-Introduction

1.1. Climate change and renewable energy

Owing to widespread global challenges in the energy sector, it is critical to identify the role of global energy demand is increasing rapidly because of population growth and economic development. As of now, there are approximately 7.8 billion people living on Earth. The united nation (UN) says the world population will plateau at 10.9 billion by the end of the century. The other groups forecast earlier and smaller peaks, with the global population reaching 9.7 billion by 2070 and then declining [1]. Fossil fuels, such as coal, oil, and natural gas, have been used for decades to provide most of the global primary energy, which leads to an imbalance in the carbon cycle resulting in an excess amount of carbon in the atmosphere in the form of greenhouse gases such as carbon dioxide (CO_2) and methane (CH_4).

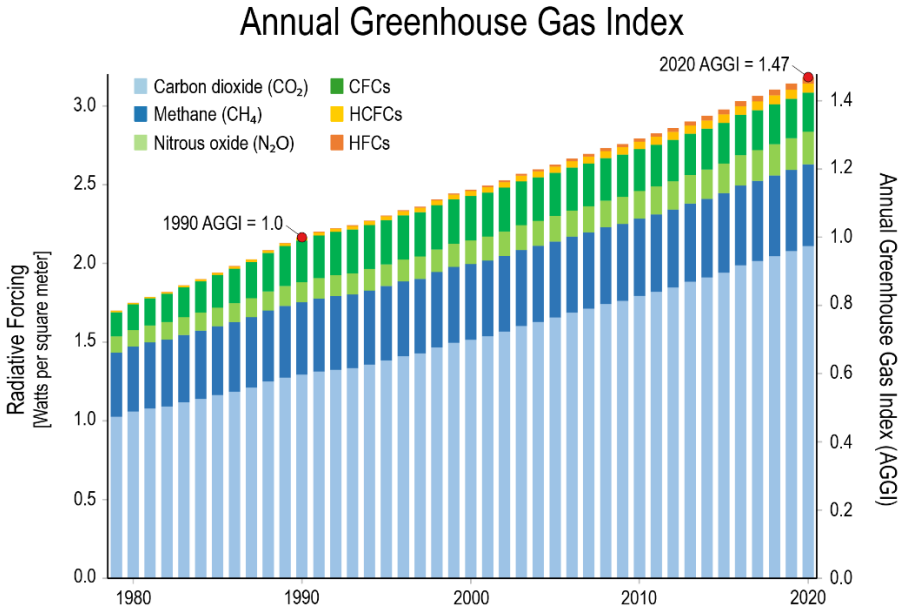

Fig. 1.1. Annual Greenhouse Gas Index (U.S. Global Change Research Program)

As shown in Fig. 1.1, the atmospheric abundance and radiative forcing of the three main long-lived greenhouse gases (CO_2, CH_4, and N_2O) continue to increase. While the combined radiative forcing of these and all other greenhouse gases included in the AGGI rose 47% from 1990 to 2020 (by ~1.02 watts per square meter), carbon dioxide has accounted for about 80% of this increase (~0.82 watts per square meter), which makes it by far the biggest contributor to increases in climate forcing since 1990.

A fundamental solution to ever-growing concerns on global warming, air pollution, and energy security is to replace the current carbon-rich fossil fuels with renewable and environment-friendly carbon-free or carbon-neutral energy sources [2]. Therefore, sustainable energy resources and conversion routes are becoming increasingly important to reduce our dependence on fossil fuels and mitigate environmental concerns [3]. Fig. 1.2 provides a brief view of the energy reserves available on the earth, which demonstrates the dominant position of solar energy among all renewable and non-renewable energy sources. The total sum of recoverable energy from all the reserves is around 1% of the solar energy supplied to the earth surface by the sun [4].

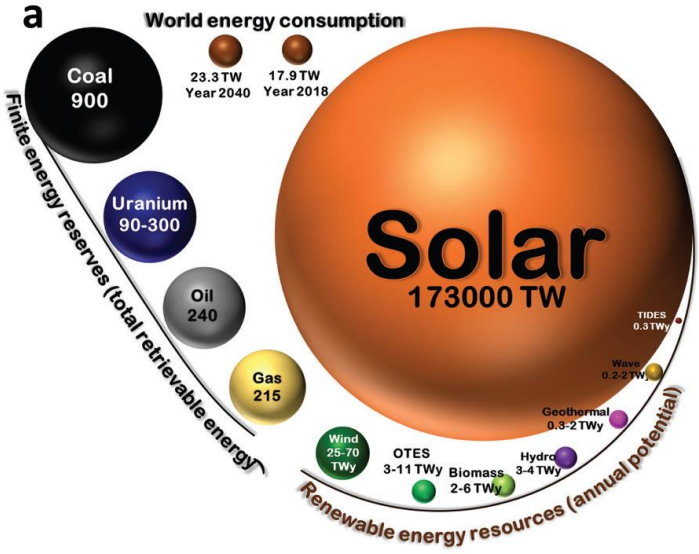

Fig. 1.2. Comparison of solar energy with other energy resources [4].

The amount of solar energy reaching the Earth's surface (roughly 1.3 × 105 TW) is more than three orders of magnitude greater than the current global energy consumption, although the intensity of solar radiation fluctuates with time and region and is often intense at locations distant from areas where energy is intensively utilized [5].

1.2. Solar hydrogen (H_2) production

To achieve a sustainable society with an energy mix primarily based on solar energy, we need methods of storing energy from sunlight as chemical fuels. Many routs exist for the conversion of water and sunlight into hydrogen:

- Photoelectrochemical (PEC) water splitting,
- Photocatalytic (PC) water splitting,
- Coupled photovoltaic-electrolysis systems,
- Photobiological methods
- Molecular artificial photosynthesis
- Plasma-chemical conversion
- Mechano-catalytic, magnetolysis, radiolysis, etc.

Nowadays, most researchers focus on the first method, photoelectrochemical water splitting, with semiconductor photoelectrodes. There are several reasons why this approach is appealing. One of the main advantages is that solar water splitting using sunlight irradiation has been widely believed to be a clean way to produce hydrogen energy without CO_2 emission [6]. A second advantage is that it can be carried out at room temperature, i.e., there is no need for large-scale solar concentrators that would limit its application to large central facilities in sunny regions of the world. A third advantage is that a photoelectrochemical water splitting device can be constructed entirely

from inorganic materials. This offers a degree of chemical robustness and durability that is difficult to achieve for organic or biological systems.

1.3. Photoelectrochemical (PEC) water splitting

Photoelectrochemical cell (PEC) for water splitting is a key technology of the future for hydrogen production. Despite the widespread attention that has been received, this technology still has many hurdles to overcome and uncharted territories to explore. Ultimately, the photon to hydrogen conversion efficiency has yet to be increased to such a level that commercial applications could become viable [7]. The concept of photoelectrochemical water splitting dates back to 1972 since Honda and Fujishima found that TiO_2 photoelectrodes showed promising PEC water splitting properties [8]. The water splitting reaction is already well established in nature. For instance, green plants and cyanobacteria used this water splitting machinery to run the very important photosynthetic process. Engineering artificial photosynthetic systems to afford the efficient and economical conversion of abundant solar energy into chemical fuel is an important step towards the realization of a sustainable carbon-neutral society [9]. The PEC water splitting processes take place with several steps as follows, which shows in Fig. 1.3.

1. Absorption of solar radiation by the photoelectrode, followed by charge carrier generation because of photoexcitation of electrons in the valence band of photoelectrode.
2. Separation and transport of charge carriers to the electrode surface by the internal or external bias applied through the circuit.
3. Oxidation of water at the anode by the photoexcited holes. Simultaneously, transport of H^+ ions from the anode to the cathode, and transport of the photoexcited electrons to the cathode through an external circuit, followed by the reduction of H^+ ions into hydrogen gas at the cathode by the photoexcited electrons [10].

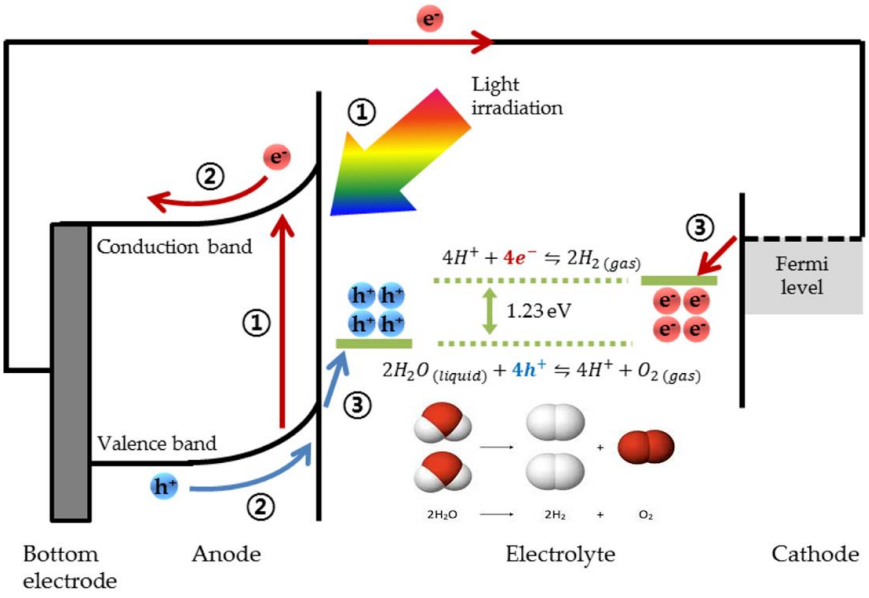

Fig. 1.3. Schematic representation of the photoelectrochemical (PEC) water splitting process [10].

At the heart of PEC water splitting system for harvesting solar energy is the semiconductor material, which transforms absorbed solar photons into excited electronic states (both electrons and holes) [11].

1.4. Materials for PEC water splitting devices

The U.S. Department of Energy has projected the cost of producing hydrogen gas through PEC water splitting must reach approximately $2.10 per kg (in 2007 dollars) to become economically competitive and has laid out multiple scenarios and pathways to reach this target [12]. To realize the final goal of industrializing solar hydrogen production, several challenges need to be addressed. As an example, active photocatalysts currently tend to contain Ta and various noble metals. These should be replaced with inexpensive, abundant elements such as fourth-period transition metals. Semiconductor photocatalysts that are active for water splitting can be classified into two categories: compound materials based upon transition metal cations that do not have d-electrons in their outmost orbitals and those based on metal cations whose outmost d-orbitals are fully

occupied [13]. An ideal water splitting photoelectrodes requires semiconductor materials that possess the following characteristics: (I) suitable band-gap energy and band positions. (II) efficient charge carrier separation and transportation in the semiconductor. (III) strong catalytic activity and stability [9].

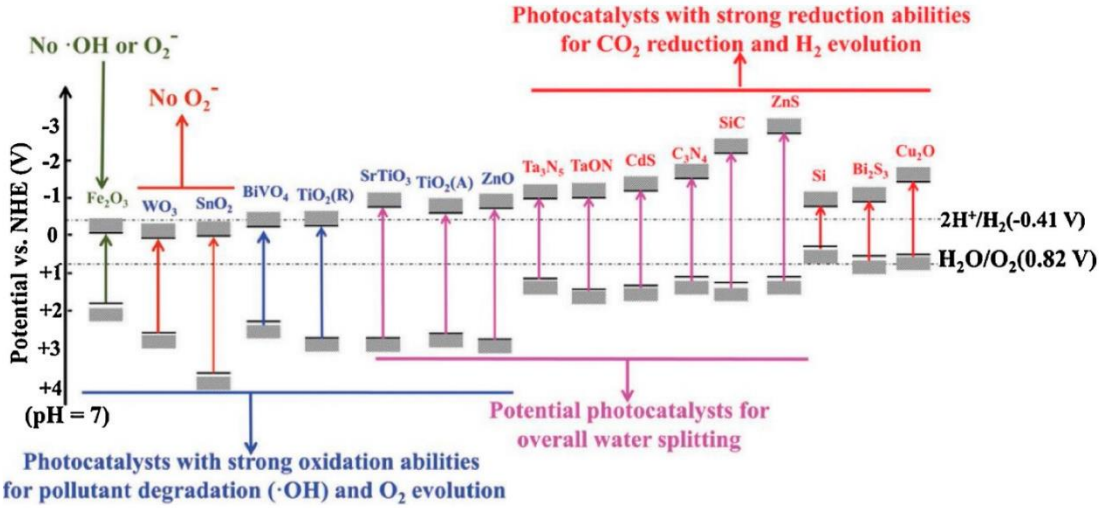

Fig. 1.4. Band structure and potential application of various semiconductors [14].

In Fig. 1.4, band structure and potential application of various semiconductors are summarized. Our strategy consists of identifying the semiconducting metal oxides with bandgaps that are smaller than TiO_2. Therefore, we have focused our attention on Iron oxide.

1.5. Hematite α-Fe_2O_3

Iron oxides are common compounds, which are widespread in nature. Moreover, iron oxides are nontoxic and environment friendly. Therefore, iron oxides are presently used in many industrial processes and are studied for application in many research fields. Among iron oxides, hematite (α-Fe_2O_3) is the most stable phase and abundant mineral on Earth. Thus, from the scalability point of view, α-Fe_2O_3 is the top material for energy-related technologies applications. α-Fe_2O_3 is a very promising material for photo-electrochemical water splitting due to its widespread availability,

extraordinary chemical stability in oxidative environment and sufficiently broad visible light absorption [15]. It is an n-type semiconductor with a suitable band gap of 2.1 eV, which allows the absorption of a large portion of the terrestrial solar spectrum. Iron oxide, Fe_2O_3, exists in amorphous as well as crystalline polymorphs (α, β, γ, and ε). The crystalline α-Fe_2O_3 is thermodynamically most stable and most common oxide form in red-brown color. The Fe^{3+} and O^{2-} ions in α-Fe_2O_3 are arranged in a corundum structure. The O^{2-} anions are positioned in a hexagonal closed packed lattice along the (001) direction whereas the Fe^{3+} cations take up the two third of the octahedral interstices in the (001) base plane and the tetrahedral sites remain vacant (Fig.1.5.a) [16]. α-Fe_2O_3 has a suitable bandgap energy (E_g~2.0–2.2 eV) which can theoretically generate a photocurrent density of >12 mA/cm^2 under AM 1.5 solar spectrum (100 mWcm^2). It has lower valence band position (+2.3 V vs. NHE at pH 0) than the water oxidation potential (1.23 V_{RHE}), which makes it a potential photocatalytic material for water oxidation (Fig. 1.5.b) [17].

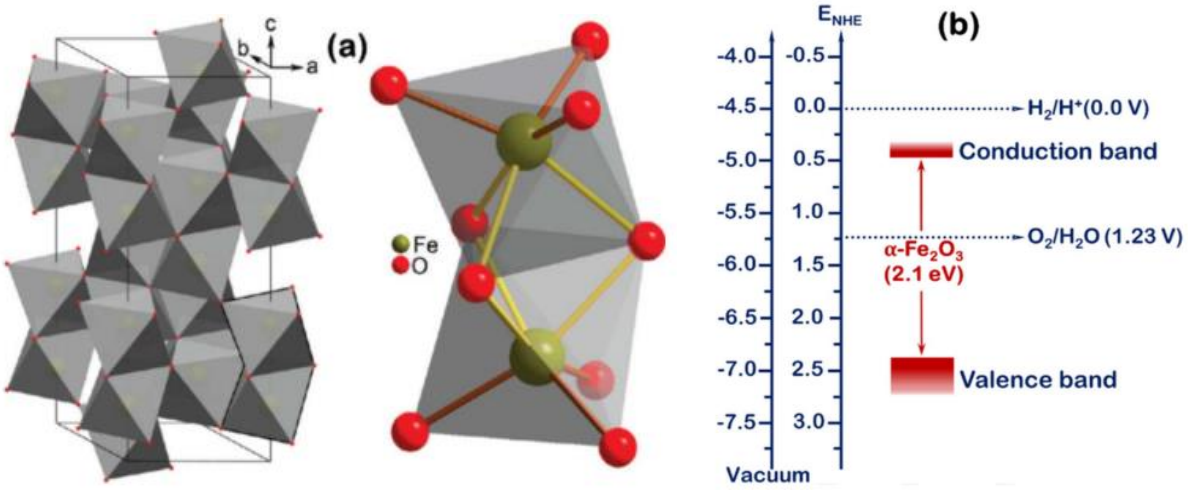

Fig. 1.5. (a) The unit cell (left) of α-Fe_2O_3 shows the octahedral face sharing Fe_2O_9 dimers forming chains in the c direction. A detailed view (right) of one Fe_2O_9 dimer shows how the electrostatic repulsion of the Fe^{3+} cations produce long (yellow) and short (brown) Fe-O (b) Energy band structure of α-Fe_2O_3 at pH=0 relative to NHE as well as the vacuum level, and the water redox energy levels [18].

Table 1 summarizes the advantages and disadvantages of α-Fe_2O_3. Despite all the desired characteristics of α-Fe_2O_3 as a photoanode for water oxidation, its PEC performance is usually

much lower than the limit in practice because of its extremely short hole diffusion length (2-4 nm), low electrical conductivity, and instability in acidic media. Moreover, the more positive conduction band position of α-Fe_2O_3 relative to the hydrogen reduction potential gives a low photovoltage and requires a large external bias voltage to make effective solar water splitting. Typically, onset potential of hematite is in the range of 0.8~1.0 V_{RHE} which is far positive compared with the Fermi-level position of hematite (~0.4 V_{RHE}), indicating a significant potential drop occurring at the α-Fe_2O_3 water interface [19]. Therefore, it is a need to develop elaborated multiple modification strategies to overcome all these barriers and have an efficient PEC water splitting system.

Table 1: Summarizes the advantages and disadvantages of α-Fe_2O_3

Advantages	Disadvantages
● Ideal band gap energy (~ 2.1 ev) ● Earth - abundant ● Stable in alkaline media ● Maximal solar-to-hydrogen (STH) conversion efficiency is 15.3% ● Environmentally benign	● Positive conduction band edge ● high current onset potential ● Short hole diffusion length (2 ~ 4 nm) ● Slow water oxidation kinetics of crystalline hematite.

1.6. Strategies to enhance photoelectrochemical properties of α-Fe_2O_3

The development of suitable techniques to fabricate high efficiency α-Fe_2O_3 photoelectrode for PEC water spitting is crucial. To date, there are many methods, which have been developed to prepare α-Fe_2O_3 photoelectrodes for use in solar water oxidation (Fig. 1.6). First, the morphologies of α-Fe_2O_3 photoelectrode such as shape, size, and particle contact strongly effect on their interfacial energetics, kinetics, and charge transport properties as well as reactive sites [20]. Second, nanocomposites provide a powerful route to overcome limitations in the current studies of single material systems for water splitting, where the photoelectrochemical performance of

photoelectrode can be significantly improved by the choice of proper interactions of constituents [21].

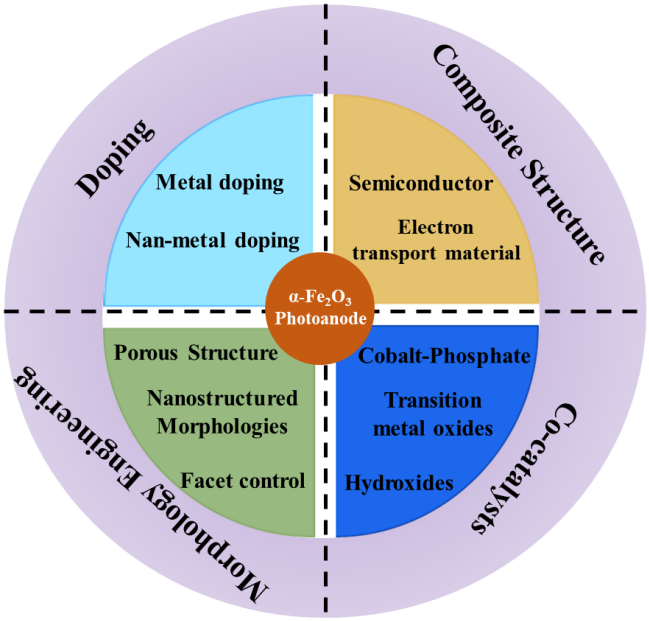

Fig. 1.6. Strategies to enhance photoelectrochemical properties of α-Fe_2O_3

Third, doping with the metal (such as W, Cu, Zn, Ti, Mo, Ag, etc.) or nonmetal (such as P and N) materials can change the electrical and optical properties of α-Fe_2O_3 [22]. Finally, decoration of α-Fe_2O_3 with various oxygen evolution catalysts (OECs) such as Co–Pi, Co_3O_4, CoO, and NiFe improves the kinetic for oxygen evolution and provides unique active sites for catalytic reactions, thereby strongly enhanced the photocurrent density [20].

References:

[1] D. Adam, How far will global population rise? Researchers can't agree, Nature Publishing Group, 2021.
[2] I. Roger, M.A. Shipman, M.D. Symes, Earth-abundant catalysts for electrochemical and photoelectrochemical water splitting, Nature Reviews Chemistry, 1 (2017) 0003.
[3] B.R. Cladek, S.M. Everett, M.T. McDonnell, M.G. Tucker, D.J. Keffer, C.J. Rawn, Local structure and distortions of mixed methane-carbon dioxide hydrates, Communications Chemistry, 4 (2021) 6.
[4] J.H. Kim, D. Hansora, P. Sharma, J.-W. Jang, J.S. Lee, Toward practical solar hydrogen production – an artificial photosynthetic leaf-to-farm challenge, Chemical Society Reviews, 48 (2019) 1908-1971.
[5] K. Welter, N. Hamzelui, V. Smirnov, J.P. Becker, W. Jaegermann, F. Finger, Catalysts from earth abundant materials in a scalable, stand-alone photovoltaic-electrochemical module for solar water splitting, Journal of Materials Chemistry A, 6 (2018) 15968-15976.
[6] S. Chen, T. Takata, K. Domen, Particulate photocatalysts for overall water splitting, Nature Reviews Materials, 2 (2017) 17050.
[7] K.-H. Ye, H. Li, D. Huang, S. Xiao, W. Qiu, M. Li, Y. Hu, W. Mai, H. Ji, S. Yang, Enhancing photoelectrochemical water splitting by combining work function tuning and heterojunction engineering, Nature Communications, 10 (2019) 3687.
[8] D. Huang, L. Li, K. Wang, Y. Li, K. Feng, F. Jiang, Wittichenite semiconductor of Cu3BiS3 films for efficient hydrogen evolution from solar driven photoelectrochemical water splitting, Nature Communications, 12 (2021) 3795.
[9] C. Jiang, S.J.A. Moniz, A. Wang, T. Zhang, J. Tang, Photoelectrochemical devices for solar water splitting – materials and challenges, Chemical Society Reviews, 46 (2017) 4645-4660.
[10] S.Y. Jeong, J. Song, S. Lee, Photoelectrochemical Device Designs toward Practical Solar Water Splitting: A Review on the Recent Progress of BiVO4 and BiFeO3 Photoanodes, Applied Sciences, 8 (2018) 1388.
[11] K. Sivula, R. van de Krol, Semiconducting materials for photoelectrochemical energy conversion, Nature Reviews Materials, 1 (2016) 15010.
[12] E. Samuel, B. Joshi, M.-W. Kim, M.T. Swihart, S.S. Yoon, Morphology engineering of photoelectrodes for efficient photoelectrochemical water splitting, Nano Energy, 72 (2020) 104648.
[13] K. Maeda, K. Domen, New Non-Oxide Photocatalysts Designed for Overall Water Splitting under Visible Light, The Journal of Physical Chemistry C, 111 (2007) 7851-7861.
[14] X. Li, R. Shen, S. Ma, X. Chen, J. Xie, Graphene-based heterojunction photocatalysts, Applied Surface Science, 430 (2018) 53-107.
[15] P.C.K. Vesborg, T.F. Jaramillo, Addressing the terawatt challenge: scalability in the supply of chemical elements for renewable energy, RSC Advances, 2 (2012) 7933-7947.
[16] K. Sivula, R. Zboril, F. Le Formal, R. Robert, A. Weidenkaff, J. Tucek, J. Frydrych, M. Grätzel, Photoelectrochemical Water Splitting with Mesoporous Hematite Prepared by a Solution-Based Colloidal Approach, Journal of the American Chemical Society, 132 (2010) 7436-7444.
[17] S. Shen, S.A. Lindley, X. Chen, J.Z. Zhang, Hematite heterostructures for photoelectrochemical water splitting: rational materials design and charge carrier dynamics, Energy & Environmental Science, 9 (2016) 2744-2775.
[18] P. Sharma, J.-W. Jang, J.S. Lee, Key Strategies to Advance the Photoelectrochemical Water Splitting Performance of α-Fe2O3 Photoanode, ChemCatChem, 11 (2019) 157-179.
[19] K. Sivula, F. Le Formal, M. Grätzel, Solar Water Splitting: Progress Using Hematite (α-Fe2O3) Photoelectrodes, ChemSusChem, 4 (2011) 432-449.
[20] S. Chandrasekaran, L. Yao, L. Deng, C. Bowen, Y. Zhang, S. Chen, Z. Lin, F. Peng, P. Zhang, Recent advances in metal sulfides: from controlled fabrication to electrocatalytic, photocatalytic and photoelectrochemical water splitting and beyond, Chemical Society Reviews, 48 (2019) 4178-4280.
[21] Y. Li, X. Wei, B. Zhu, H. Wang, Y. Tang, T.C. Sum, X. Chen, Hierarchically branched Fe2O3@TiO2 nanorod arrays for photoelectrochemical water splitting: facile synthesis and enhanced photoelectrochemical performance, Nanoscale, 8 (2016) 11284-11290.
[22] J. Su, J. Wang, C. Liu, B. Feng, Y. Chen, L. Guo, On the role of metal atom doping in hematite for improved photoelectrochemical properties: a comparison study, RSC Advances, 6 (2016) 101745-101751.

Chapter 2-Doping

The band gap of hematite (α-Fe_2O_3) is 2.1eV which that shows visible photocatalytic activity; however, its electron-hole recombination rate is high and causes the less utilization of the generated electron-hole pairs. To overcome this drawback controlling of donor concentration by enriched metal dopant is implemented. In this chapter, two metals (Molybdenum (Mo) and Tungsten (W)) have been optimized as a metal doping to improve the electroconductivity of α-Fe_2O_3 photoanode. Further, characterization analyses and photoelectrochemical measurements are systematically investigated for both doped α-Fe_2O_3 photoanode. This chapter contains two sections as follow:

2.1. Molybdenum doping

2.2. Tungsten doping

Chapter 2 - Section 1- Doping Molybdenum (Mo)

The role of doping molybdenum (Mo) and back-front sides illumination in enhancing the charge separation of α-Fe_2O_3 nanorod photoanode toward solar water splitting

Abstract:

Hematite (α-Fe_2O_3) has abundant reserves and an appropriate bandgap of ~2.1 eV for H_2 production using water splitting. However, its potential application to solar water splitting is seriously limited by the extremely high charge recombination rate of the charge carriers. The present work investigated the photoelectrochemical (PEC) performance of molybdenum (Mo) doped α-Fe_2O_3 thin-film electrodes. The Mo doped α-Fe_2O_3 samples were prepared by a hydrothermal method and then loaded the different ratio of molybdenum to optimize the photo current density. Morphological characterization and crystal structure identification were measured by FE-SEM, RAMAN, XRD, XPS and UV-vis analyses. After doping Mo on the α-Fe_2O_3, the photocurrent density significantly enhanced. The optimized Mo amount doped α-Fe_2O_3 film (10% Mo-doped α-Fe_2O_3) had a photocurrent density of 0.75 and 1.2 $mA.cm^{-2}$ in the front and back side illumination at 0.6 V versus Ag/AgCl under 100 $mWcm^{-2}$ and a 1 M (pH=12) aqueous NaOH solution as the electrolyte respectively, which are ~ 10 and 17 times higher than that of the pure α-Fe_2O_3 photoanode. The doping of Mo onto pure α-Fe_2O_3 caused a donor concentration increase (1.3-fold), a space charge layer reduction (1.2-fold), and a flat band potential decrease (1.6-fold), which improved the photoelectrochemical efficiency.

2.1.1. Introduction

Many countries or communities face insufficient energy supply and suffer from air pollution problems mainly originated from fossil fuel combustion used for energy production. These problems of energy shortage and air pollution can be solved by utilizing renewable energy resources such as hydrogen. To produce hydrogen without using conventional methods such as cracking and refining fossil fuels like oils and coals will required the development of sustainable production methods using solar energy. One of the most promising and sustainable method for hydrogen production is using photocatalysts which can generate electron-hole-pairs after sunlight illumination. The photoelectrochemical (PEC) cells have ability to convert electromagnetic energy of sun light source, to split water into oxygen and hydrogen [1-5]. Metal oxide-based photocatalysts such as $BiVO_4$ [6, 7], WO_3 [8], ZnO [9, 10] and α-Fe_2O_3 [9, 11, 12] show special properties such as simple manufacture method, good stability in electrolyte solution, proper band gap energy, which is essential for producing electron-hole pairs, and low preparation cost[13-15]. Hematite (α-Fe_2O_3), a n-type metal oxide semiconductor with desirable bandgap (1.9−2.1 eV), has been extensively applied as a suitable photoanode material for PEC water splitting [1, 11, 16, 17]. However, its weak conductivity and very short hole diffusion length, which induces fast electron-hole recombination, have limited the use of the hematite semiconductor for improving PEC performance. Various strategies have been reported to improve the PEC performance of α-Fe_2O_3 such as nanostructures [18-20], doping (e.g., α-Fe_2O_3 doped Ti or BVO doped Mo) [21, 22], heterostructures (e.g., α-Fe_2O_3/BVO and α-Fe_2O_3/Cds) [23-26], and co-catalyst (e.g., apply Co-Pi on surface) [27, 28]. Optical and electronical properties of intrinsic semiconductors can improve by doping Metals in the role of impurity at their structure. In this trend, more free electron were generated and the donor concentration in semiconductor increase [29].

Herein, the effect of Mo doping was systematically studied over a range of Mo atomic percentage from 5 to 15% by optimizing the hydrothermal process time for preparing the α-Fe_2O_3 structure. The Mo-α-Fe_2O_3 film was heat treated for monoclinic crystallization on the surface of fluorine tin oxide (FTO). The influence of light illumination direction (back and front sides) onto the photoanode on the PEC performance was also investigated. Finally, the effect of Mo-doping on conductivity and charge carrier transport was studied by analyzing the Mott-Schottky plot and impedance of the α-Fe_2O_3 and Mo-α-Fe_2O_3 electrodes.

2.1.2. Experimental Section

2.1.2.1. Fabrication of Hematite (α-Fe_2O_3) films

Pristine α-Fe_2O_3 films with a nanorod (NR) structure were produced on conductive glass (FTO) substrate based on the previously reported hydrothermal method [30, 31]. At first, FTO glass was cleaned by acetone, ethanol and deionized (DI) water for 15 min in an ultrasonication bath. Then, 80 ml of an aqueous solution was prepared by 0.15 M ferric chloride ($FeCl_3.6H_2O$) and 1 M sodium nitrate ($NaNO_3$). Hydrochloric acid (HCl) was added dropwise to adjust the pH of the mixture to 1.5 PH. The cleaned FTO substrates were put at the bottom of a teflon container and 80 ml of the solution was decanted to the container. The container was placed in a stainless-steel autoclave that was then put in an oven at 100°C for 6 h to undergo an optimized hydrothermal process. In the aqueous solution, Fe^{3+} ions were interlocked with OH^- ions to produce iron oxide nuclei, as described by the following reaction (1):

$$Fe^{3+}{}_{(aq)} + 3OH^-{}_{(aq)} \longrightarrow \beta\text{-}FeOOH_{(s)} + H_2O_{(l/g)} \quad (1)$$

After washing the residues with deionized water, an identical yellowish layer of β-FeOOH was covered on the FTO. In the calcination step, the β-FeOOH was converted into α-Fe_2O_3. The

hematite electrode was put in a muffle furnace to be sintered in air at 550°C for 4 h. The chemical reaction goes through the phase transition, as shown in equation (2):

$$2\beta\text{-FeOOH}_{(s)} \longrightarrow \alpha\text{-}Fe_2O_{3\,(s)} + H_2O_{(l/g)} \quad (2)$$

2.1.2.2. Modification by doping with Molybdenum

After preparation of the hematite NR thin film, a drop casting method was applied to the aqueous solution containing molybdenum precursor to make Mo-doped hematite thin films. The precursor was ammonium heptamolybdate tetrahydrate ($(NH_4)6Mo_7O_{24}\cdot 4H_2O$) with different atomic percentages of Mo in 30 ml DI water, homogenized by applying ultrasonic wave for 1 h. The precursor solution was dropped on to the electrodes surface, then the films were put in an oven at 80ºC for drying, and the drop casting was repeated for 1, 3, 5 times optimized by measuring the PEC performance. Finally, the samples were placed in a furnace for heat treatment at 450ºC for 30 minutes.

2.1.2.3. Photoelectrochemical (PEC) Measurement:

PEC measurements were done by a standard three-electrode structure of the Hematite (pristine α-Fe_2O_3 and modified with molybdenum) films as the working electrode with a platinum wire counter electrode, Ag/AgCl reference electrode and 1 M NaOH as the electrolyte. The PEC measurements, electrochemical impedance evaluation, and open-circuit voltage decline were measured under an illumination of 100mW/cm^2 (AM 1.5) from a 300W Xe lamp from the front and back sides of the photoanode in the voltage range of -0.7 to 0.7 V (vs. Ag/AgCl). Electrochemical impedance spectroscopy (EIS) was conducted by using a potentiostat with the identical electrode formation. The Mott-Schottky plots were also conducted in PEC measurements under dark state.

2.1.3. Results and discussion

2.1.3.1. Samples characterization

Fig. 2.1.1 shows the FE-SEM images of the pristine and 10% Mo-doped hematite. The length and diameter of the NRs were approximately 80 nm and 500 nm, respectively, which are similar to previous reports [32, 33]. A broad view of the 10% Mo-α-Fe_2O_3 further confirmed the uniformity of the NRs. However, the 10% Mo-doped hematite NRs were separated without aggregation and higher harshness in the walls of the NRs compared with the pristine hematite (Fig. 2.1.1.b and d), which may have increased the light harvesting in the 10%Mo-α-Fe_2O_3 electrode as revealed in the UV-vis analyses (see Fig. 2.1.4b), which improved the PEC performance.

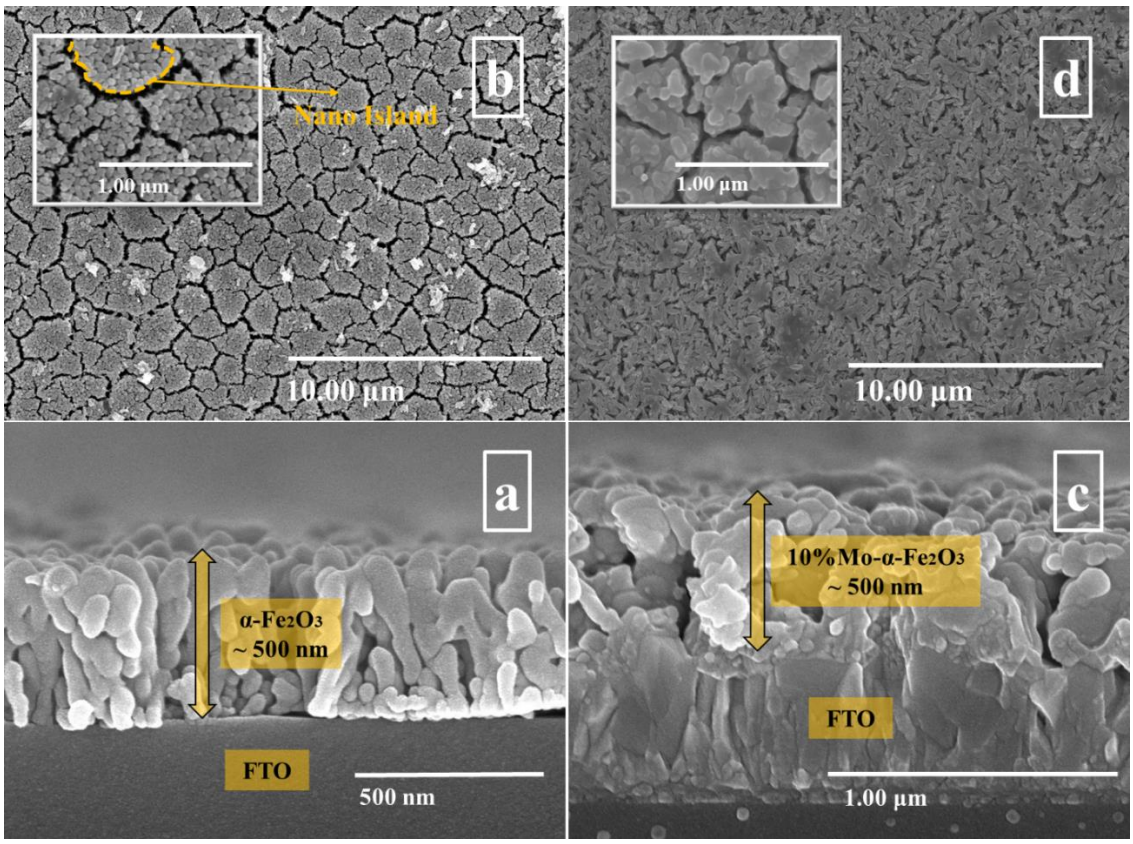

Fig. 2.1.1. Top-views (b and d) and cross-sectional (a and c), FE-SEM images of pristine hematite (a and b) and 10% Mo-doped hematite (c and d).

The X-ray diffraction (XRD) measurements were displayed to examine the crystallinity and phase

purity of hematite in both pristine and Mo-doped photoanodes (Fig. 2.1.2a). The peaks of all films can be indexed to α-Fe_2O_3 by using the JCPDS card No. 24-0072 catalog as a reference. Mo does not change the hematite structure. In the XRD patterns of all samples, the (110) plane confirms the presence of hematite (α-Fe_2O_3) for both pristine and Mo-doped samples. [34, 35]

The Raman spectra of α-Fe_2O_3 and Mo-α-Fe_2O_3 photoanodes are presented in Fig. 2.1.2b. The important peaks for bare hematite and Mo-doped photoanodes after calcination agree with the reported values of α-Fe_2O_3 [36]. The Raman peaks at about 610 cm^2 and 1318 cm^2 may represent surface disorder of the α-Fe_2O_3 films [37]

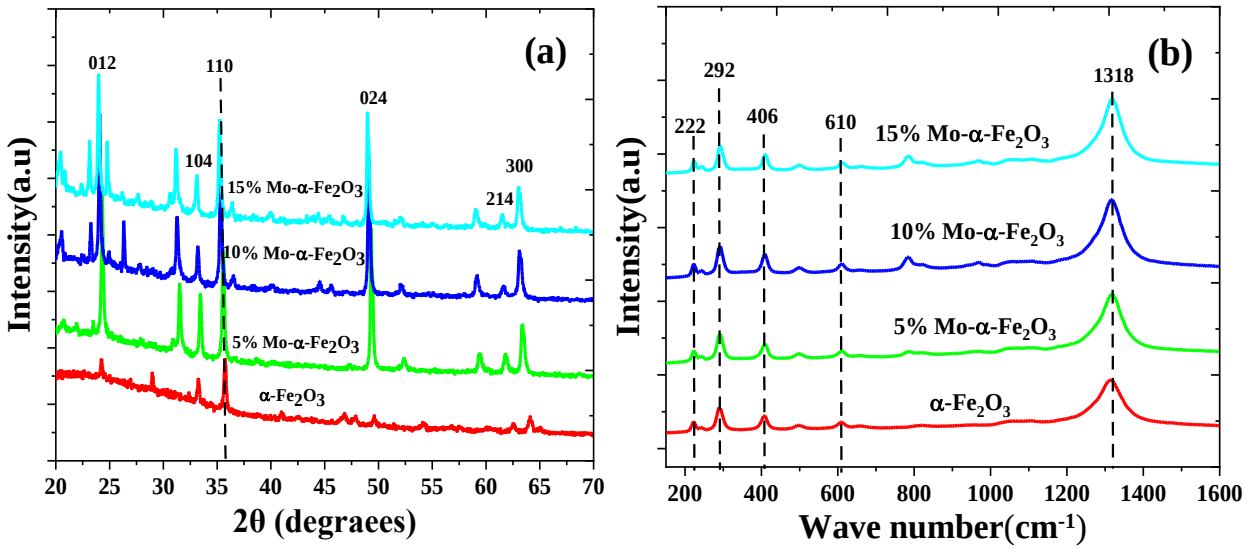

Fig. 2.1.2. (a) X-Ray diffraction patterns and (b) Raman spectra for pristine hematite and Mo-doped hematite.

Fig. 2.1.3a shows the XPS survey spectra of the α-Fe_2O_3 and Mo-α-Fe_2O_3 electrodes. Fe2p, O1 s and Mo3d peaks are clear in all samples. They are according to the main component elements of the α-Fe_2O_3 and 10%Mo-α-Fe_2O_3 structures. The Fe2p and O1s XPS peaks of pure α-Fe_2O_3 and 10% Mo- α-Fe_2O_3 samples are somewhat similar (Fig. 2.1.3b and c). Fig. 2.1.3d clearly shows the Mo 3d5/2 peak at 232.5 eV and the Mo 3d 3/2 XPS peak at 235.5 eV. This indicated that the Mo atoms in the hematite lattice were in the Mo^{+6} state and therefore could donate one free electron to

supply the electro conductivity of the film. [38, 39]

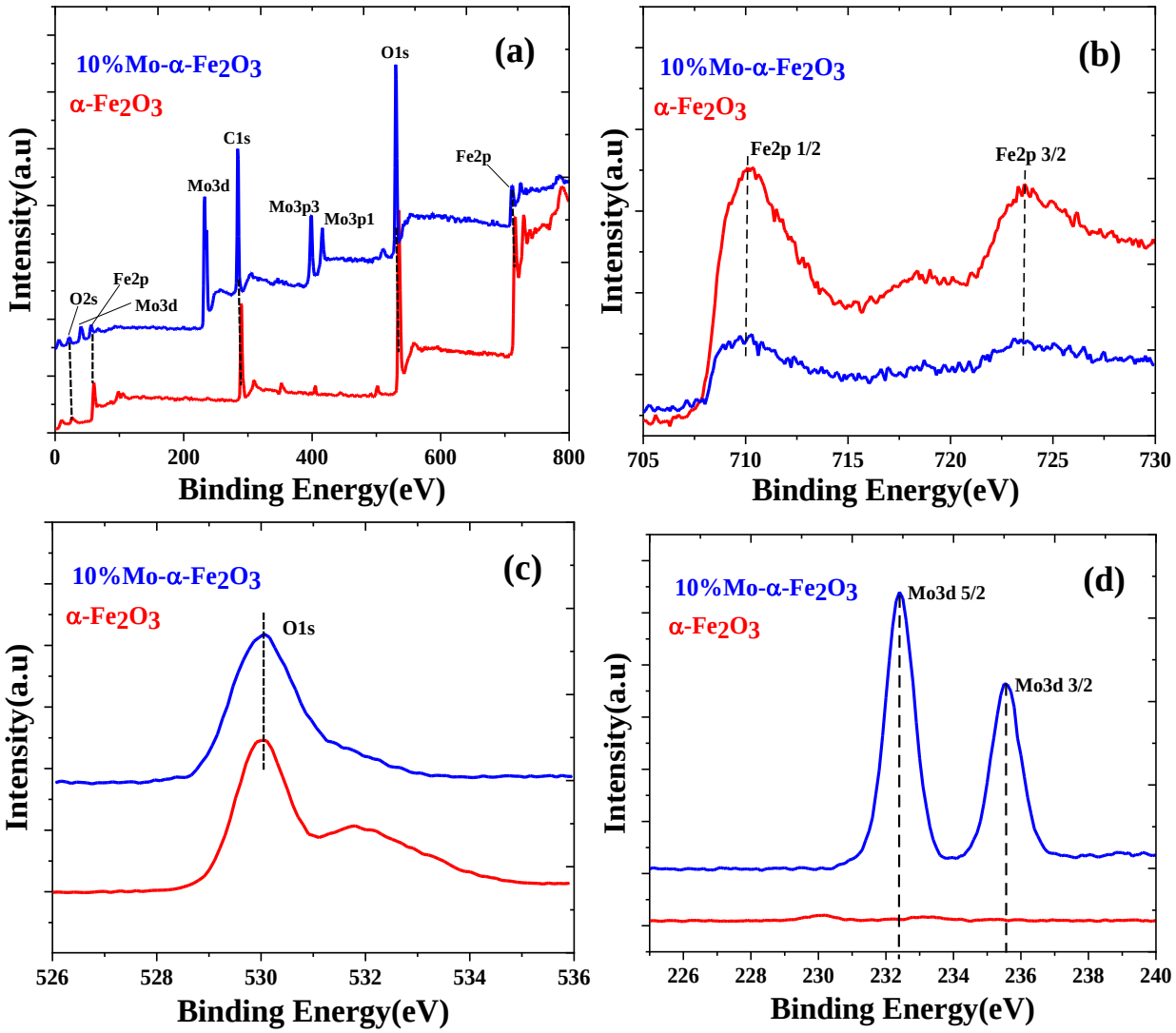

Fig. 2.1.3. (a) XPS survey spectra and high-resolution XPS spectra for (b) Fe 2p (c) O1s and (d) Mo3d for pristine and 10% Mo-doped hematite.

Fig. 2.1.4a shows UV–Vis reflectance spectra of the bare and doped hematite electrodes. The reflectance of the photoanode with Mo doping is increased in the visible light region. The optical band gap energies were estimated using the following equation (3).

$$F(hv)= (1-R(hv))^2/2R(hv) \quad (3)$$

Fig. 2.1.4 b and c was shown the band gap for α-Fe_2O_3 and Mo-doped α-Fe_2O_3 samples which decreased after doping Mo from 2.06 to 1.95 eV. Mo-doped α-Fe_2O_3 samples could absorb more

photons than the pristine α-Fe_2O_3 sample, and therefore generated more electron-hole pairs. The valence band (VB) edges of pure α-Fe_2O_3 and 10% Mo-doped α-Fe_2O_3 samples were estimated to be 2.2 eV, and 1.6 eV, respectively. The conduction band (CB) of the 10% Mo-doped sample was more negative than that of pure α-Fe_2O_3 (Fig. 2.1.4d). The identified band gap decreased to 1.95 eV by 10%Mo-doping α-Fe_2O_3, which is a unique electronic structure and confirms the improved photoelectrochemical efficiency under higher wave number (low energy) of visible light irradiation compared with that of pure α-Fe_2O_3 [13].

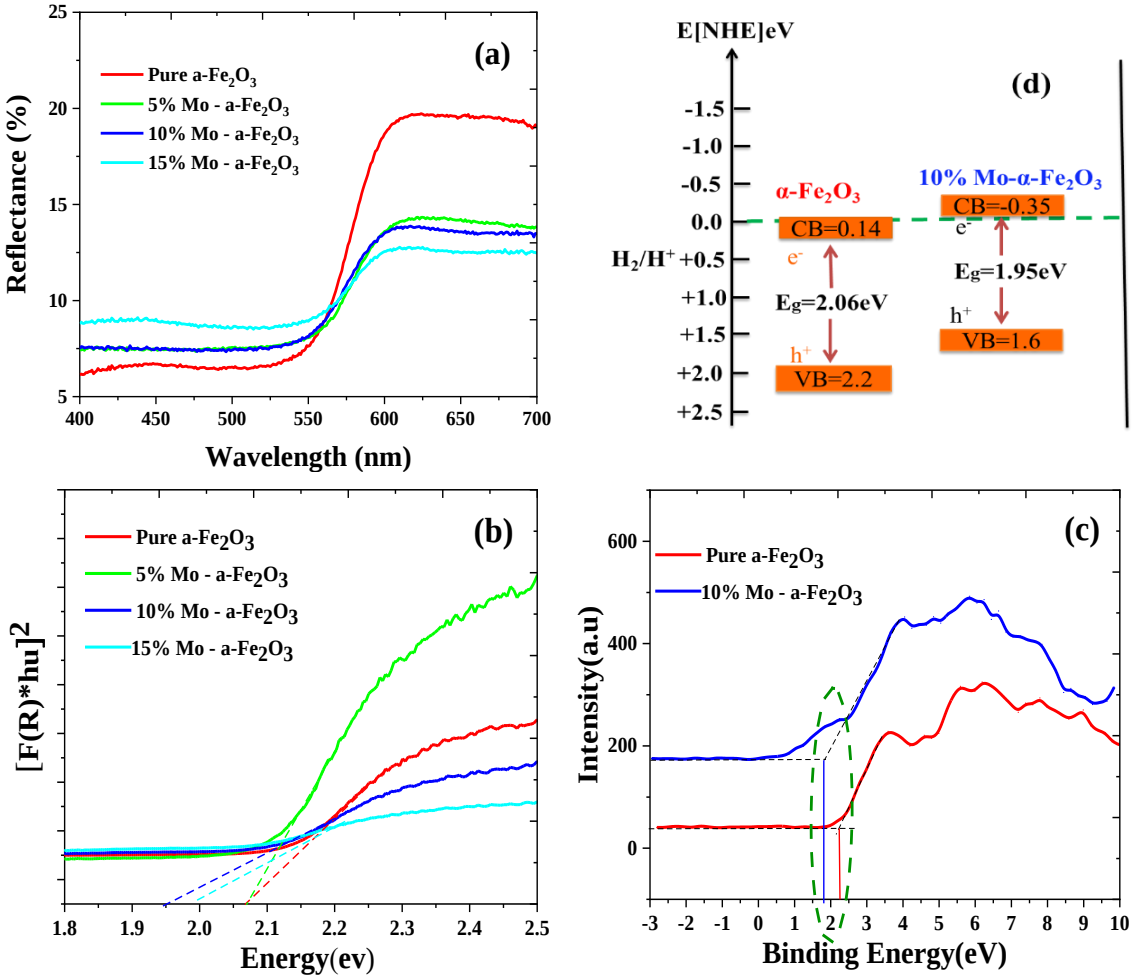

Fig. 2.1.4. (a) UV–vis reflectance spectra, (b) band gap energies, (c) VB, and (d) schematic illustration of the band gap structure of pristine and 10% Mo-modified hematite

2.1.3.2. Photoelectrochemical (PEC) properties

Linear sweep voltammetry (LSV) and chopped scan voltammetry for the pristine α-Fe_2O_3 and various Mo-α-Fe_2O_3 electrodes were measured under dark and light conditions at -0.6 ~ 0.6 V vs. Ag/AgCl (Fig. 2.1.5a and b). In the dark state, the photocurrent density was around zero. Bare α-Fe_2O_3 had a weak photo response in the photocurrent density and achieved ~75 μA.cm^{-2} at 0.6 V vs. Ag/AgCl with an onset potential of around 0.6 V vs. Ag/AgCl. The onset potential slightly shifted to less applied voltage and the photocurrent density was improved after doping Mo. The photocurrent density of the 10% Mo-α-Fe_2O_3 electrode was around 0.75 mA.cm^{-2}, which was greatly (10-fold) increased in compared to that of the pristine hematite electrode at front-side illumination of the electrodes at 0.6 V vs. Ag/AgCl.

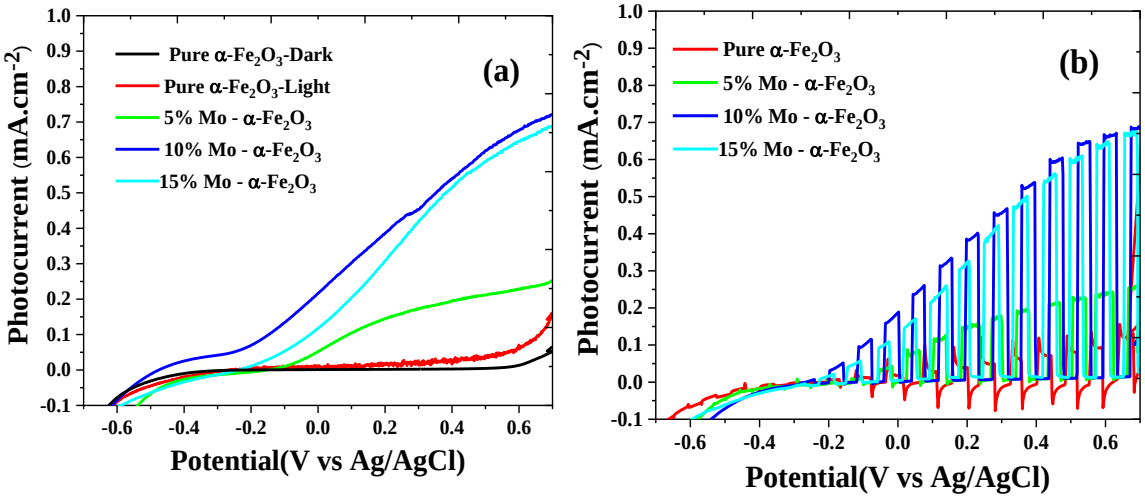

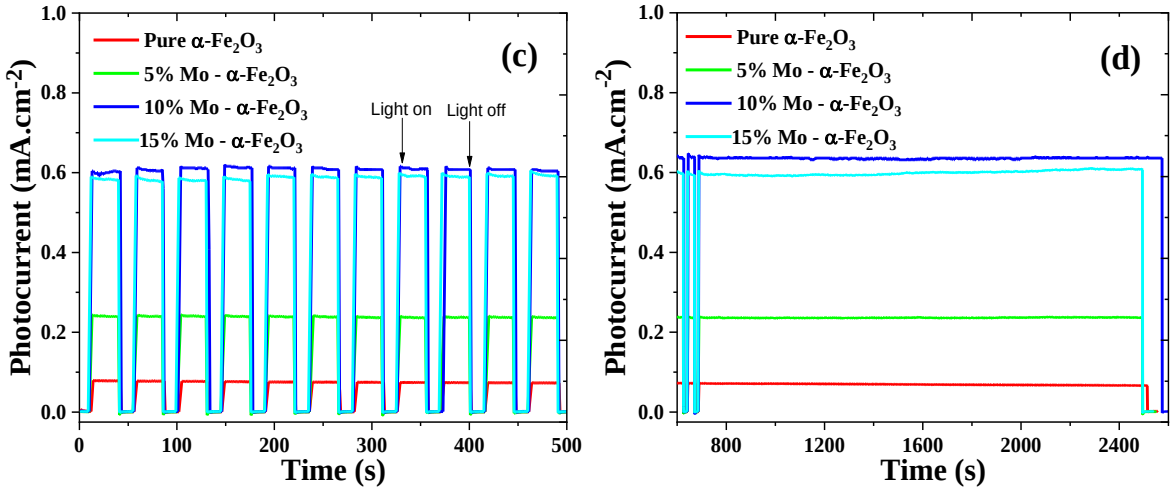

Fig. 2.1.5. (a) Photocurrent density vs. potential linear (b) chopped scan voltammetry (c) Photocurrent response and (d) photocurrent stability of different Mo- α-Fe_2O_3 films at a potential of 0.6 V (vs. Ag/AgCl) under 100 $mWcm^{-2}$, while the supporting electrolyte was a 1M (pH=12) aqueous solution of NaOH.

Fig. 2.1.5c and d compare the photocurrent response and stability over 10 cycles and 1800s, respectively, for pristine α-Fe_2O_3 and α-Fe_2O_3 NRs doped with Mo. The pristine α-Fe_2O_3 NRs exhibited a photocurrent density of around 0.1 mA cm^{-2} at 0.6 V vs. Ag/AgCl. After α-Fe_2O_3 was doped with Mo, the photocurrent of the hematite electrodes was greatly improved. The 10% Mo-α-Fe_2O_3 hematite NRs exhibited the highest photocurrent response. After 10 on-off cycles, the photoelectrode showed good stability even after 30-min light exposure without loss of the photocurrent.

The influence of light illumination direction onto the photoanode on the PEC performance was studied. The theory behind this approach is the variation in the degrees of accessibility of the charge carrier produced in various zones of the photoanode, as shown in Fig. 2.1.6a. When the light was irradiated from the back side of the pure and Mo-doped hematite, the photocurrent density was greatly increased. The identified photocurrent for 10% Mo-hematite with back-side light illumination reached around 1.2 mA cm^{-2}, which was twice that of the front-side one. Fig. 2.1.6b shows the schematics of electrons generated from the α-Fe_2O_3 thin film. It implies the transport process to the FTO under the visible light irradiation from the front and back sides. In

the back-side illumination, the electrons generated from the surface of α-Fe_2O_3 closer to the FTO. They have shorter diffusion length through the absorption depth than that of the front-side illumination. Thus, the photocurrent density and the electron transfer efficiency increases and it can control the PEC reaction kinetic [40, 41]

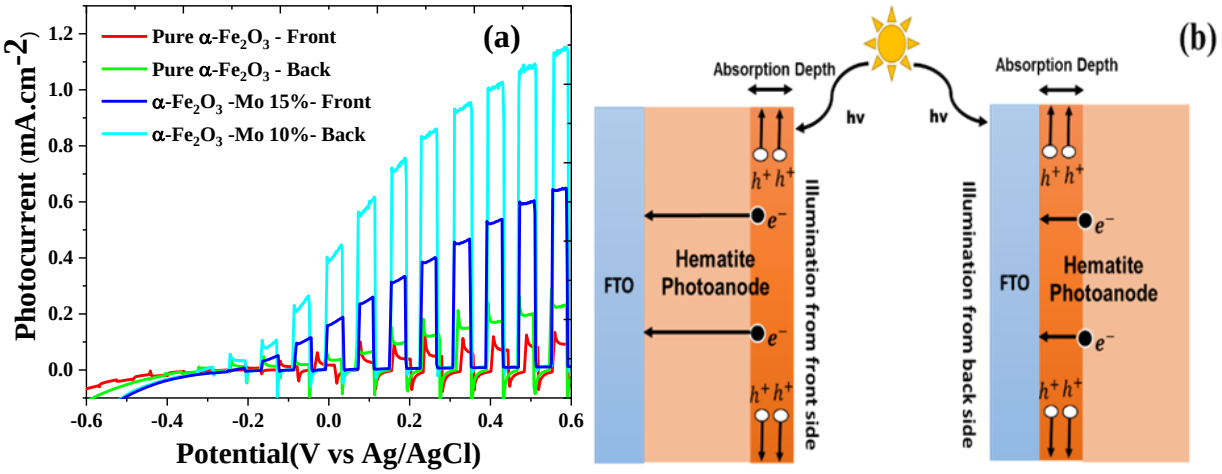

Fig. 2.1.6. (a) Chopped photocurrent density versus potential of different Mo- α-Fe_2O_3 films at a potential of 0.6 V (vs. Ag/AgCl) under 100 $mWcm^{-2}$ front and back sides illumination, while the supporting electrolyte was a 1M (pH=12) aqueous solution of NaOH, (b) Back and front side illumination mechanism

Impedance analysis **(**EIS) is characterized the charge transfer capability. As shown in Fig. 2.1.7a, the semicircle radius increases in the following order: 10%Mo-α-Fe_2O_3 < 15%Mo-α-Fe_2O_3 < 5%Mo-α-Fe_2O_3 < pure α-Fe_2O_3. A lower semicircle radius represents a better effect of charge carrier transfer by reducing resistance at the electrolyte/photoanode interface. The Mo-α-Fe_2O_3 structures effectively reduce its charge transfer resistance (R_{ct}) and hence their electrodes display higher conductivity for photogenerated carriers transport [42].

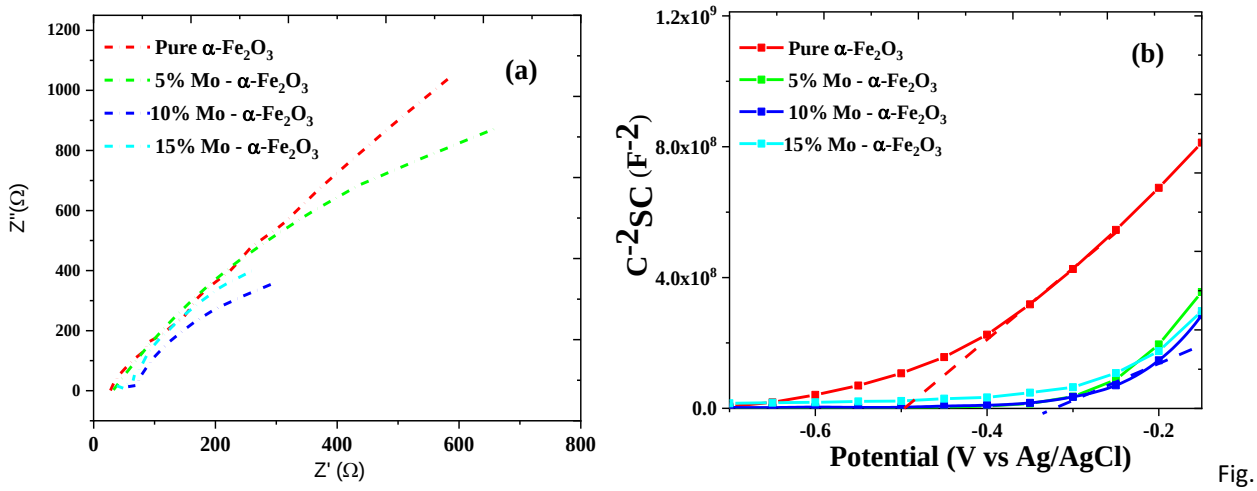

Fig. 2.1.7. (a) Nyquist EIS plots (b) Mott–Schottky and impedance plot of Mo- α-Fe2O3 thin films. The supporting electrolyte was a 1M aqueous solution of NaOH.

The width of the space charge layer (W_{SCL}) can be obtained by solving Poisson's equation, which depends on N_D and V_{fb}, as expressed in equation (4) [43].

$$W_{SCL} = \sqrt{\frac{2\varepsilon\varepsilon_0(V - V_{fb})}{eN_D}} \quad (4)$$

The W_{SCL} of the prepared 10% Mo-doped α-Fe_2O_3 film was around 17% lower than that of pure α-Fe_2O_3 because the film had a maximum N_D (N_D=6.88E+26 m^3) and a minimum band potential (V_{fb}=0.3 V) among the Mo-doped α-Fe_2O_3 films. This lower charge layer caused the fast and efficient charge separation that improved the PEC efficiency for the 10% Mo-doped α-Fe_2O_3 photoelectrode. The W_{SCL} obtained for the synthesized α-Fe_2O_3 was in good accordance with the reported W_{SCL} of scheelite- α-Fe_2O_3 ranging from 2 to 4 nm [44]. The donor concentration of the 10%Mo-doped α-Fe_2O_3 electrode was 6.88E+26 m^{-3}, which was around 1.3-fold higher than that of pure α-Fe_2O_3 (5.40E+26 m^{-3}). This result supports that the use of Mo-doped α-Fe_2O_3 can improve the electronic properties of pure semiconductors of α-Fe_2O_3. Fig. 2.1.8a show the donor density (N_D) and flat band potential (V_{fb}), which are two important parameters for the PEC performance, as a function of Mo percentage. Mo doping by substituting an electron-rich atom

into the α-Fe_2O_3 crystalline structure improved the donor density. As shown in Fig. 2.1.8a, with increasing Mo percentage in the α-Fe_2O_3 structure, the donor concentration increased and reached a maximum at 10% Mo (6.88E+26). The flat band potential after Mo doping shifted downward compared to that of bare α-Fe_2O_3 (V_{fb} =0.47 V for pure α-Fe_2O_3 and V_{fb}=-0.3 V for 10% Mo- α-Fe_2O_3), which revealed the lower overpotential required for oxygen evolution reaction [45].

The open circuit potential (OCP) was measured to further show the improvement in carrier-separation for the α-Fe_2O_3 and 10% Mo-α-Fe_2O_3 photoelectrodes. Fig. 2.1.8b shows the change in OCP (ΔOCP) versus light illumination time. The obtained ΔOCP for 10% Mo-α-Fe_2O_3 was much higher than that of pure α-Fe_2O_3, representing the production of more photogenerated electrons in 10% Mo - α-Fe_2O_3 resulting from the fewer recombination electron-holes.

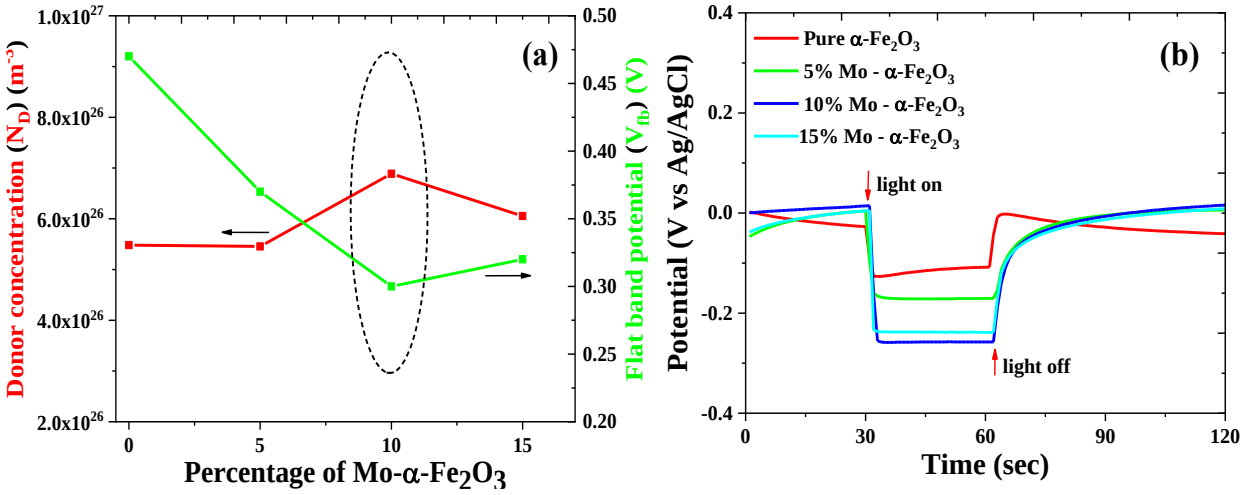

Fig. 2.1.8. (a) The relationship between Donor concentration (N_D) and V_{fb} and (b) change in open circuit potential (ΔOCP) value for Mo-α-Fe_2O_3 photoelectrodes.

2.1.3.3. Mechanism of PEC improvement

To understand the effect of Mo doping for enhanced PEC performance of α-Fe_2O_3, the schematic form of bond structure has been shown in Figs. 2.1.9a and b. Herein, we investigated the activity of α-Fe_2O_3 before and after doping Mo systematically. The band gap of hematite is 2.1eV which

that shows visible photocatalytic activity; however, its electron-hole recombination rate is high and causes the less utilization of the generated electron-hole pairs. To circumvent this drawback controlling of donor concentration using enriched electron elements such as Mo is implemented. As shown schematically in Fig. 2.1.9, the energy band bending (qV_D) increased after Mo doping to α-Fe_2O_3. As a result of this large band bending, after light irradiation a large portion of holes transfer to the electrode-electrolyte interface and subsequently the recombination rate decreased within bulk of 10% Mo-α-Fe_2O_3 compared to α-Fe_2O_3. Furthermore, the electron mobility in bulk α-Fe_2O_3 improved considerably after Mo doping. This leads photogenerated electron shuttled to the FTO and collected more efficiently on the FTO surface before recombination. Therefore, the photocurrent density increases in 10% Mo-α-Fe_2O_3 electrode compared to the pure α-Fe_2O_3. Based on the above-mentioned considerations, the population of electrons in donor level is an exponential function of the difference between the conduction band energy and the Fermi energy. Furthermore, after Mo doping population of electrons will be increase because donor concentration increases, and the Fermi level of the electrode shifts upward as following equation (6).

$$E_f = E_i + kT^*\ln (N_D/n_i) \quad (6)$$

Where k is Boltzmann's constant, N_D, n_i, E_i are the donor concentration, the electron concentration without doping and Fermi level position without doping. However, in α-Fe_2O_3 electrode as shown in Fig. 2.1.9a, due to low donor concentration, the fermi level is in lower position compared to 10% Mo-α-Fe_2O_3. It is clearly observed in Fig. 2.1.9 that the electrons can easily move to CB in 10% Mo-α-Fe_2O_3 because of higher electron population in donor level close to after light illumination. However, in pure α-Fe_2O_3 electrode the number of electrons that can move from VB to CB is reduced because of electrons need higher energy to transfer.

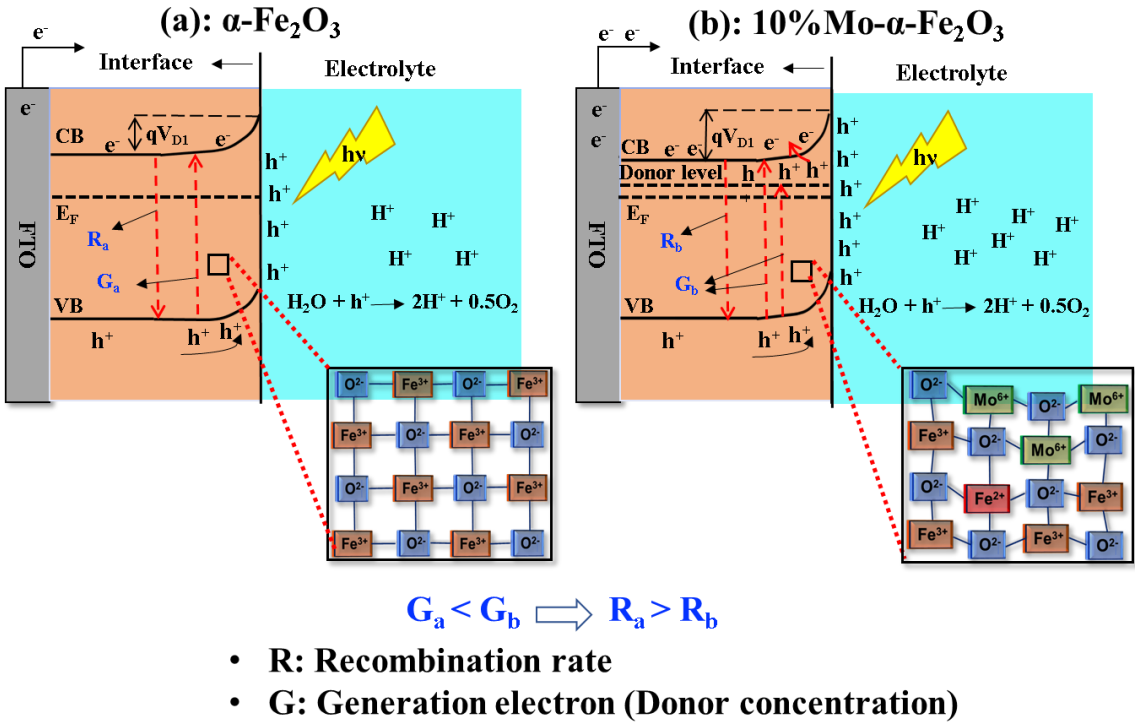

Fig. 2.1.9. Schematic band diagrams illustrating the main assumption charge-carrier behaviors following light excitation in (a) pure α-Fe_2O_3 electrode and (b) 10%Mo-α-Fe_2O_3 electrode in contact with 1M NaOH electrolyte.

2.1.4. Conclusions

Mo-doped α-Fe_2O_3 photoanode films were successfully fabricated by using the hydrothermal method and optimizing the bath time of the hydrothermal process and the ratio of Mo doping. The easy dissolution of Mo into the α-Fe_2O_3 structure for successful doping was confirmed by SEM, RAMAN, UV-vis, XPS and XRD analyses. The 10% Mo-α-Fe_2O_3 electrodes showed greatly improved PEC performance, which comprised 10-fold higher photocurrent density than that of pure α-Fe_2O_3. Combined analyses of Mott-Schottky plots and electrochemical impedance spectroscopy (EIS) confirmed that the W_{SCL} of 10% Mo-doped α-Fe_2O_3 was around 17% lower than that of pure α-Fe_2O_3. In addition, 10% Mo-α-Fe_2O_3 showed a maximum N_D (N_D=6.88E+26 m^3) and a minimum band potential (V_{fb}=0.3 V) among the Mo-doped α-Fe_2O_3 samples, which greatly enhanced the PEC performance of the α-Fe_2O_3 photoanodes.

Reference

[1] K. Sivula, F. Le Formal, M.J.C. Grätzel, Solar water splitting: progress using hematite (α-Fe2O3) photoelectrodes, 4 (2011) 432-449.
[2] M.J.n. Grätzel, Photoelectrochemical cells, 414 (2001) 338.
[3] M. Tayebi, B.-K. Lee, The Effects of W/Mo-co-doped BiVO4 Photoanodes for Improving Photoelectrochemical Water Splitting Performance, Catalysis Today, (2020).
[4] G.S. Das, J.P. Shim, A. Bhatnagar, K.M. Tripathi, T. Kim, Biomass-derived carbon Quantum Dots for Visible-Light-induced photocatalysis and Label-free Detection of fe (iii) and Ascorbic acid, Scientific reports, 9 (2019) 1-9.
[5] S.J. Park, G.S. Das, F. Schütt, R. Adelung, Y.K. Mishra, K.M. Tripathi, T. Kim, Visible-light photocatalysis by carbon-nano-onion-functionalized ZnO tetrapods: degradation of 2, 4-dinitrophenol and a plant-model-based ecological assessment, NPG Asia Materials, 11 (2019) 1-13.
[6] M. Tayebi, A. Tayyebi, T. Soltani, B.-K.J.N.J.o.C. Lee, pH-Dependent photocatalytic performance of modified bismuth vanadate by bismuth ferrite, 43 (2019) 9106-9115.
[7] M. Tayebi, A. Tayyebi, B.-K. Lee, Photocharged molybdenum-doped BiVO4 photoanodes for simultaneous enhancements in charge transport and surface passivation, Solar Energy, 191 (2019) 427-434.
[8] J. Choi, T. Song, J. Kwon, S. Lee, H. Han, N. Roy, C. Terashima, A. Fujishima, U. Paik, S.J.A.S.S. Pitchaimuthu, WO3 nanofibrous backbone scaffolds for enhanced optical absorbance and charge transport in metal oxide (Fe2O3, BiVO4) semiconductor photoanodes towards solar fuel generation, 447 (2018) 331-337.
[9] Z. Kang, H. Si, S. Zhang, J. Wu, Y. Sun, Q. Liao, Z. Zhang, Y.J.A.F.M. Zhang, Interface Engineering for Modulation of Charge Carrier Behavior in ZnO Photoelectrochemical Water Splitting, (2019) 1808032.
[10] M. Tayebi, A. Tayyebi, Z. Masoumi, B.-K. Lee, Photocorrosion suppression and photoelectrochemical (PEC) enhancement of ZnO via hybridization with graphene nanosheets, Applied Surface Science, 502 (2020) 144189.
[11] G. Liu, Y. Zhao, K. Wang, D. He, R. Yao, J.J.A.S.C. Li, Engineering, Ultrasmall NiFe-Phosphate Nanoparticles Incorporated α-Fe2O3 Nanoarrays Photoanode Realizing High Efficient Solar Water Splitting, 6 (2018) 2353-2361.
[12] M. Mishra, D.-M.J.A.C.A.G. Chun, α-Fe2O3 as a photocatalytic material: A review, 498 (2015) 126-141.
[13] B. Sathyaseelan, E. Manikandan, V. Lakshmanan, I. Baskaran, K. Sivakumar, R. Ladchumananandasivam, J. Kennedy, M. Maaza, Structural, optical and morphological properties of post-growth calcined TiO2 nanopowder for opto-electronic device application: Ex-situ studies, Journal of Alloys and Compounds, 671 (2016) 486-492.
[14] R. Marschall, Semiconductor Composites: Strategies for Enhancing Charge Carrier Separation to Improve Photocatalytic Activity, Advanced Functional Materials, 24 (2014) 2421-2440.
[15] M. Tayebi, M. Kolaei, A. Tayyebi, Z. Masoumi, Z. Belbasi, B.-K. Lee, Reduced graphene oxide (RGO) on TiO2 for an improved photoelectrochemical (PEC) and photocatalytic activity, Solar Energy, 190 (2019) 185-194.
[16] S.Y. Chiam, M.H. Kumar, P.S. Bassi, H.L. Seng, J. Barber, L.H.J.A.a.m. Wong, interfaces, Improving the efficiency of hematite nanorods for photoelectrochemical water splitting by doping with manganese, 6 (2014) 5852-5859.
[17] T. Hisatomi, H. Dotan, M. Stefik, K. Sivula, A. Rothschild, M. Graetzel, N.J.A.M. Mathews, Enhancement in the performance of ultrathin hematite photoanode for water splitting by an oxide underlayer, 24 (2012) 2699-2702.
[18] Y. Hou, F. Zuo, A. Dagg, P. Feng, Visible light-driven α-Fe2O3 nanorod/graphene/BiV1–x Mo x O4 core/shell heterojunction array for efficient photoelectrochemical water splitting, Nano letters, 12 (2012) 6464-6473.
[19] P. Sharma, M. Zachariah, S. Ehrman, R. Shrivastava, S. Dass, V. Satsangi, S.E.C. Michael Zachariah, S.D.C. Rohit Shrivastava, P.S.T. Vibha R Satsangi, A photoelectrochemical (PEC) study on graphene oxide based hematite thin films heterojunction (R-GO/Fe2O3), APS Meeting Abstracts, 2013.
[20] K. Zhang, X. Shi, J.K. Kim, J.S. Lee, J.H. Park, Inverse opal structured α-Fe 2 O 3 on graphene thin films: enhanced photo-assisted water splitting, Nanoscale, 5 (2013) 1939-1944.
[21] D. Yan, J. Liu, Z. Shang, H.a. Luo, Ti-doped α-Fe 2 O 3 nanorods with controllable morphology by carbon layer coating for enhanced photoelectrochemical water oxidation, Dalton transactions, 46 (2017) 10558-10563.
[22] A. Kleiman-Shwarsctein, Y.-S. Hu, A.J. Forman, G.D. Stucky, E.W. McFarland, Electrodeposition of α-Fe2O3 doped with Mo or Cr as photoanodes for photocatalytic water splitting, The Journal of Physical Chemistry C, 112 (2008) 15900-15907.
[23] S. Bai, H. Chu, X. Xiang, R. Luo, J. He, A. Chen, Fabricating of Fe2O3/BiVO4 heterojunction based photoanode modified with NiFe-LDH nanosheets for efficient solar water splitting, Chemical Engineering Journal, 350 (2018) 148-156.

[24] D. Sharma, S. Upadhyay, A. Verma, V.R. Satsangi, R. Shrivastav, S. Dass, Nanostructured Ti-Fe2O3/Cu2O heterojunction photoelectrode for efficient hydrogen production, Thin Solid Films, 574 (2015) 125-131.
[25] R. Yin, M. Liu, R. Tang, L. Yin, CdS Nanoparticle-Modified α-Fe 2 O 3/TiO 2 Nanorod Array Photoanode for Efficient Photoelectrochemical Water Oxidation, Nanoscale research letters, 12 (2017) 520.
[26] J.H. Kim, J.-W. Jang, Y.H. Jo, F.F. Abdi, Y.H. Lee, R. Van De Krol, J.S. Lee, Hetero-type dual photoanodes for unbiased solar water splitting with extended light harvesting, Nature communications, 7 (2016) 13380.
[27] M. Diab, T. Mokari, Thermal decomposition approach for the formation of α-Fe2O3 mesoporous photoanodes and an α-Fe2O3/CoO hybrid structure for enhanced water oxidation, Inorganic chemistry, 53 (2014) 2304-2309.
[28] Y.B. Park, J.H. Kim, Y.J. Jang, J.H. Lee, M.H. Lee, B.J. Lee, D.H. Youn, J.S. Lee, Exfoliated NiFe Layered Double Hydroxide Cocatalyst for Enhanced Photoelectrochemical Water Oxidation with Hematite Photoanode, ChemCatChem, 11 (2019) 443-448.
[29] J. Guo, X. Yang, S. Bai, X. Xiang, R. Luo, J. He, A.J.J.o.c. Chen, i. science, Effect of Mo doping and NiFe-LDH cocatalyst on PEC water oxidation efficiency, 540 (2019) 9-19.
[30] N. Beermann, L. Vayssieres, S.E. Lindquist, A.J.J.o.t.E.S. Hagfeldt, Photoelectrochemical studies of oriented nanorod thin films of hematite, 147 (2000) 2456-2461.
[31] T. Lindgren, H. Wang, N. Beermann, L. Vayssieres, A. Hagfeldt, S.-E.J.S.E.M. Lindquist, S. Cells, Aqueous photoelectrochemistry of hematite nanorod array, 71 (2002) 231-243.
[32] J. Su, J. Wang, C. Liu, B. Feng, Y. Chen, L.J.R.A. Guo, On the role of metal atom doping in hematite for improved photoelectrochemical properties: a comparison study, 6 (2016) 101745-101751.
[33] Y. Ling, G. Wang, D.A. Wheeler, J.Z. Zhang, Li, Yat, , Sn-doped hematite nanostructures for photoelectrochemical water splitting. Nano letters11 (2011) 2119-2125.
[34] A. Cots, R.J.A.C.B.E. Gómez, Ytterbium modification of pristine and molybdenum-modified hematite electrodes as a strategy for efficient water splitting photoanodes, 219 (2017) 492-500.
[35] F. Bouhjar, L. Derbali, B. Marí, B.J.S.E.M. Bessaïs, S. Cells, Photo-deposition of cobalt-phosphate group modified hematite for efficient water splitting, 195 (2019) 241-249.
[36] G. Rahman, O.-S.J.M.C. Joo, Physics, Electrodeposited nanostructured α-Fe2O3 thin films for solar water splitting: Influence of Pt doping on photoelectrochemical performance, 140 (2013) 316-322.
[37] S.J.J.o.M.R. Shen, Toward efficient solar water splitting over hematite photoelectrodes, 29 (2014) 29-46.
[38] A. Cots, D. Cibrev, P. Bonete, R.J.J.o.S.S.E. Gomez, Photoelectrochemical behavior of molybdenum-modified nanoparticulate hematite electrodes, 22 (2018) 149-156.
[39] A. Cots, D. Cibrev, P. Bonete, R.J.C. Gómez, Hematite nanorod electrodes modified with molybdenum: photoelectrochemical studies, 4 (2017) 585-593.
[40] P.S. Bassi, L. Xianglin, Y. Fang, J.S.C. Loo, J. Barber, L.H.J.P.C.C.P. Wong, Understanding charge transport in non-doped pristine and surface passivated hematite (Fe 2 O 3) nanorods under front and backside illumination in the context of light induced water splitting, 18 (2016) 30370-30378.
[41] F. Le Formal, S.R. Pendlebury, M. Cornuz, S.D. Tilley, M. Grätzel, J.R.J.J.o.t.A.C.S. Durrant, Back electron–hole recombination in hematite photoanodes for water splitting, 136 (2014) 2564-2574.
[42] S.J. Hong, S. Lee, J.S. Jang, J.S. Lee, Heterojunction BiVO4/WO3 electrodes for enhanced photoactivity of water oxidation, Energy & Environmental Science, 4 (2011) 1781-1787.
[43] M. Tayebi, A. Tayyebi, B.-K.J.C.T. Lee, Improved photoelectrochemical performance of molybdenum (Mo)-doped monoclinic bismuth vanadate with increasing donor concentration, 328 (2019) 35-42.
[44] J. Feng, Z. Wang, X. Zhao, G. Yang, B. Zhang, Z. Chen, Y.J.T.J.o.P.C.C. Huang, Probing the Performance Limitations in Thin-Film FeVO4 Photoanodes for Solar Water Splitting, 122 (2018) 9773-9782.
[45] J. Krysa, M. Zlamal, S. Kment, M. Brunclikova, Z.J.M. Hubicka, TiO2 and Fe2O3 films for photoelectrochemical water splitting, 20 (2015) 1046-1058.

Chapter 2 - Section 2 - Doping Tungsten (W)

Investigate the effect of tungsten (W) doping on photoelectrochemical (PEC) properties of hematite (α-Fe_2O_3)

Abstract:

To decrease these drawbacks affecting the PEC performance of α-Fe_2O_3, various techniques have been examined. For instance, doping techniques particularly using metals, have been widely applied to obtain improved PEC performance by increasing the conductivity, lifetime of charge carriers, hole diffuse length and crystallinity. This study reports a new and facile construction method for improving the PEC performance of the α-Fe_2O_3 photoanode. Here, α-Fe_2O_3 is newly developed with W by using a simple and low-cost drop casting method, then systematically investigated to get elucidate the metal doping effects. The present study demonstrates that W is such a good dopant for improving the activity of the α-Fe_2O_3 photoanodes by enhancing the charge carrier mobility. Subsequently, optimizing the tungsten content was shown to lead a significant enhancement in PEC performance for 0.5% W doped α-Fe_2O_3 had a photocurrent density of ~ 0.5 $mA.cm^{-2}$ at 1.23 V_{RHE} under 100 $mWcm^{-2}$ and a 1 M (pH~14) aqueous NaOH solution as the electrolyte respectively, which are ~7 times higher than that of the pure α-Fe_2O_3 photoanode (~0.07 $mA.cm^{-2}$ at 1.23 V_{RHE}).

2.2.1. Introduction

Although, half a century has passed since discovery of photoelectrochemical water splitting by Honda and Fujishima, its conversion efficiency is not enough for practical applications [1]. Direct water splitting requires relatively high energy (<1.23 V) which can be assisted by semiconductor materials with a suitable band position for hydrogen evolution reaction (HER) and oxygen evolution reaction (OER) [2-4]. Efficient PEC semiconductors should have following virtues: (I) suitable conduction and valence bands position; (II) effectively separating and transferring electron-hole; (III) absorption light in a wide range. Among these semiconductors, hematite (α-Fe_2O_3) is considered as a promising candidate for water splitting because of its favorable band gap (2.1 eV), low cost, non-toxicity, and excellent chemical stability [5, 6]. However, α-Fe_2O_3 suffers from a short hole diffusion length (2-3 nm) and quick electron-hole recombination rate leading to low energy conversion efficiency [7]. To address these limitations and improve solar conversion efficiency, enormous efforts have been focused on the development of hematite nanostructures and the modification of their electronic structure via elemental doping [8].

Herein, we demonstrate the design and synthesis of tungsten-doped hematite (W doped α-Fe_2O_3) photoanode by a hydrothermal and drop casting methods. The photoelectrochemical measurements indicate that significantly enhanced photocurrent and lowered turn-on voltage for W doped α-Fe_2O_3 photoanodes as compared with pure α-Fe_2O_3. Further, the synergistic effects between Ti-doping result describe that in lower electron-holes recombination rates and enhance the charge separation due to the improved conductivity by doping tungsten as a metal dopant in the α-Fe_2O_3 photoanode.

2.2.2. Experimental Section

2.2.2.1. Preparation of W doped αFe$_2$O$_3$ photoanode

Akageneite (β-FeOOH) thin film was fabricated on fluorine tin oxide (FTO) using a hydrothermal method. An aqueous solution was prepared by mixing 1 M sodium nitrate ($NaNO_3$) and 0.15M ferric chloride ($FeCl_3.6H_2O$) as a precursor and then adding hydrochloric acid (HCl) to adjust the pH to 1.5. Next, the FTO was washed with a mixture of deionized water, acetone, and anhydrous ethanol in equal volumes, and then placed at the bottom of a Teflon container and had 80ml precursor poured over it. The autoclave was then left in an oven at 100°C for six hours. After this, the residues on the coated FTO were washed with deionized water, and β-FeOOH appeared in the form of a yellowish layer. The samples were placed in a furnace at 550°C for 3 h to produce α-Fe_2O_3 thin film. The α-Fe_2O_3 photoanode was doped with Tungsten (W) through a simple and low-cost drop casting method with W containing species with different amounts of $N_{10}H_{42}W_{12}O_{42}$ in 30ml deionized water. Finally, the W doped α-Fe_2O_3 photoanodes with W content (atomic percentage) were optimized by loading 500µl of the 0.25, 0.5, or 1 % atomic ratio of W precursor on the surface of the α-Fe_2O_3 photoanode, and the resulting photoanodes were labeled 0.25W:αFe_2O_3, 0.5W:αFe_2O_3 and 1W:αFe_2O_3, respectively.

2.2.2.2. Characterization Equipment

The morphologies and structures of the samples were characterized by using scanning electron microscopy (SEM, Model Quanta 250 FEG) and transmission electron microscopy (TEM, JEOL, JEM-2100F). The structures and crystallinities of the different catalytic films were characterized by X-ray diffraction (XRD). The X-ray source was Bruker D8Advance with monochromatic Cu Kα radiation (λ=1.5406 Å) in the 2θ range of 10–55°. A Raman spectrum was used with the laser line at 785 nm as the excitation source at room temperature (Bruker, model: Senteraa 2009,

Germany). The chemical states of the component elements in the film samples were investigated using Thermo Scientific Sigma Probe spectrometer with a monochromatic AlKα source (photon energy 1486.6 eV), spot size of 400 μm, energy step size of 1.0 eV and pass energy of 200 eV. The optical properties of the photoanodes were measured by Perkin Elmer UV-Vis-NIR model Lambda 950. Finally, photoluminescence (PL) spectra were detected at room temperature using an Edinburgh F-4600 NF900 (FLS920) fluorescence spectrophotometer at an excitation of 400 nm. Electron paramagnetic resonance (EPR) measurements in the X-band (9.64 GHz) were performed using a CW/Pulse EPR System(QM09).

2.2.2.3. Photoelectrochemical (PEC) Measurement

The PEC measurements were obtained using a standard three-electrode structure. The pure α-Fe_2O_3 and modified W:α-Fe_2O_3 photoelectrodes were used as working electrodes and a platinum wire was used as a counter electrode with an Ag/AgCl reference electrode in 1 M NaOH electrolyte. The applied bias was also displayed in RHE scale using the following relationship (Eq.1):

$$V_{RHE} = V_{Ag/AgCl} + 0.197 + 0.059\ pH \quad (1)$$

The PEC performance was measured under an illumination of 100mW/cm^2 (AM 1.5) from a 300W Xe lamp from the front side of the photoanodes in the voltage range from -0.3 to 1.5 V (vs. RHE). Electrochemical impedance spectroscopy (EIS) was conducted by using a potentiostat with the identical electrode formation. The Mott-Schottky plots were also conducted in PEC measurements under dark state. Finally, to investigate the conversion ratio of the incident photon to electron, Incident Photon-to-electron Conversion Efficiency (IPCE) measurements were also conducted using different filters in this system at 1.23V(vs. RHE) under an illumination of 100mW.cm^{-2}.

2.2.3. Results and Discussion

2.2.3.1. Structural characterization

Field emission scanning electron microscope (FESEM) images illustrate the oval shaped α-Fe_2O_3 nanostructure on the FTO (Fig. 2.2.1). As shown in Fig. 2.2.1c, the surface agglomeration in the 1W:α-Fe_2O_3 photoanode significantly decreased its light harvesting and photocurrent density.

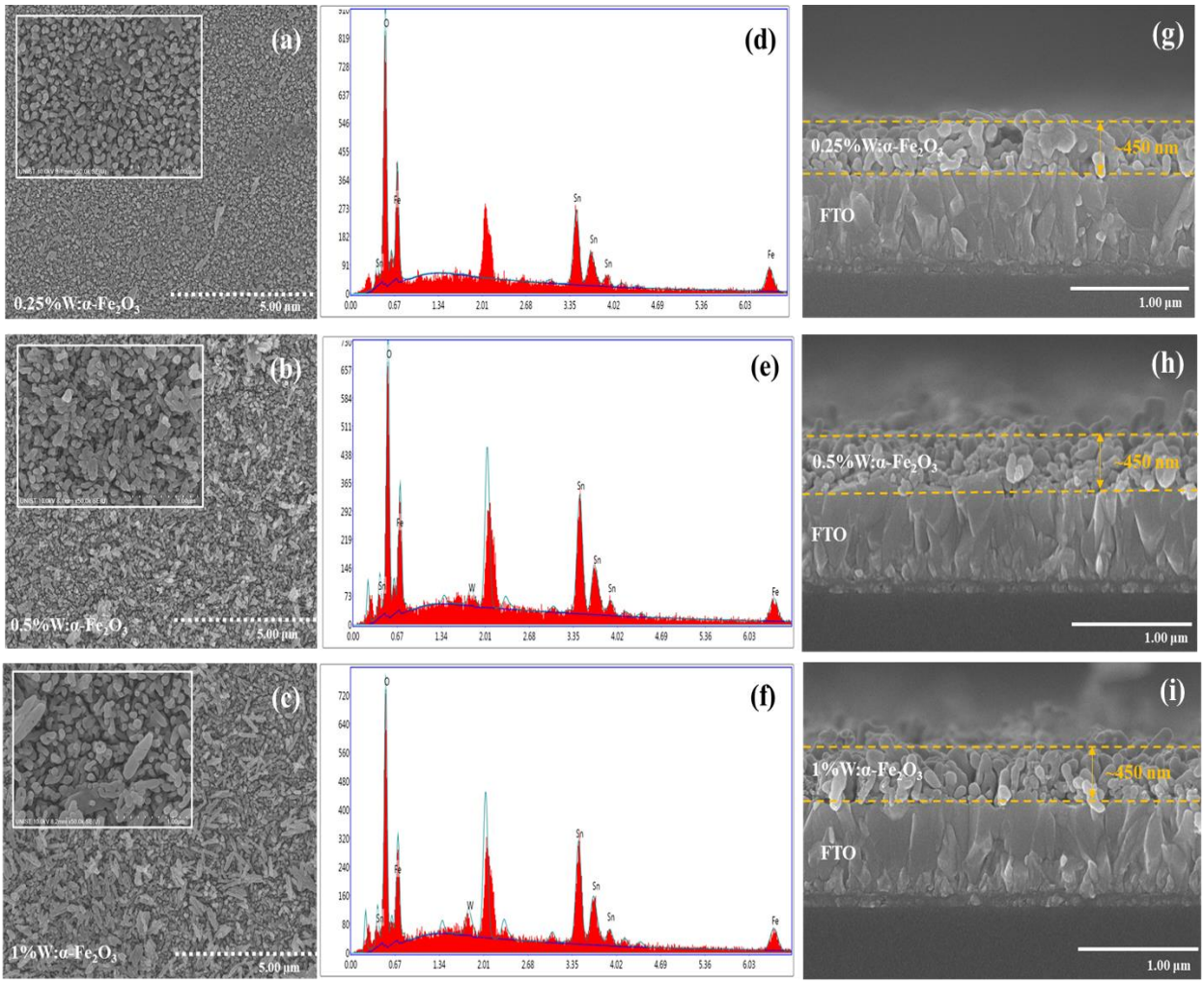

Fig. 2.2.1. (a-c) Top-view, (d-f) EDX, and (g-i) cross section of 0.25W:α-Fe_2O_3, 0.5W:α-Fe_2O_3, and 1W:α-Fe_2O_3.

However, the 0.25W:α-Fe_2O_3 with the less dopant condensation showed a slight change in surface morphology (Fig. 2.2.1a), leading to its detection even at a low absorption range in optical characterization analysis (Fig. 2.2.2). The thickness of all W doped α-Fe_2O_3 samples is estimated

by SEM cross-section which is in order of around 450 nm without any significant changes in the α-Fe_2O_3 morphology (Fig. 2.2.1 (h-I)).

The phase purities and crystallographic structures of the prepared pure α-Fe_2O_3 and W:α-Fe_2O_3 thin films were confirmed by using X-ray diffraction (XRD) patterns (see Fig. 2.2.2a). The diffractions at 34, 37, 62 and 64° respectively corresponded to the (104), (110), (214), and (300) planes of the α-Fe_2O_3 structure (PDF 02-0915) in all the samples and no additional XRD peak could be observed. Thus, the XRD data reveals that the crystal structure of α-Fe_2O_3 was not changed after doping W and no extra peaks appear in XRD, so it can be confirmed that the role of W is doping [9-11]. Fig. 2.2.2b shows the Raman spectra of pure α-Fe_2O_3 and W:α-Fe_2O_3 photoanodes to further clarify the structural features. All the characteristic peaks of the α-Fe_2O_3-based samples show well crystallized features of the hematite. The spectral range between 200 and 650 cm^{-1} contains the most intensive peaks of α-Fe_2O_3, while the peak recorded at 1315 cm^{-1} with a higher intensity is determined to be a second harmonic vibration [12].

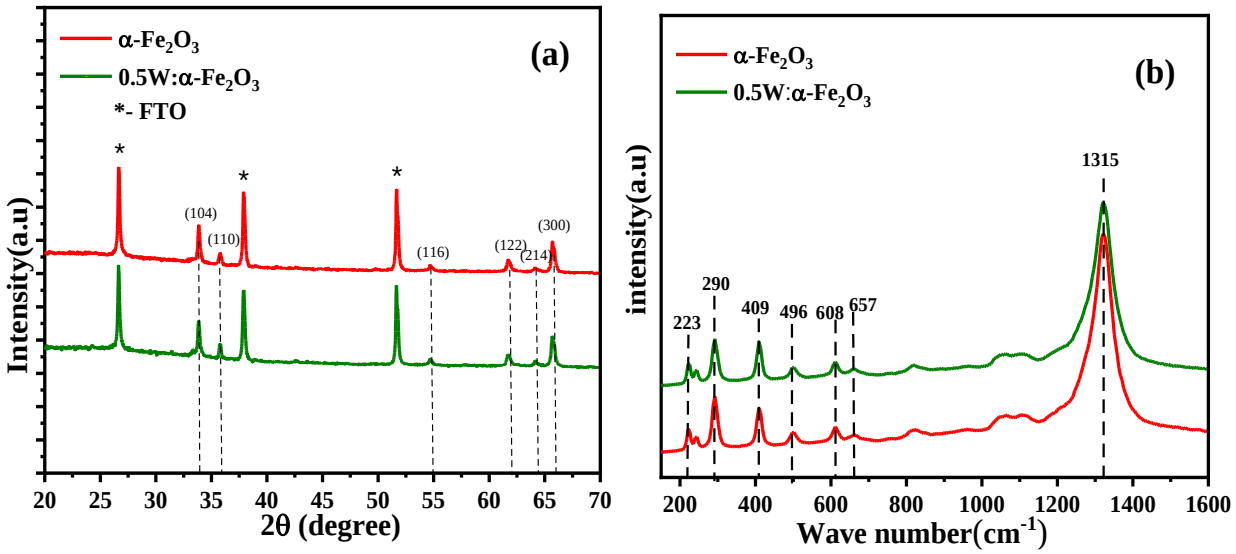

Fig. 2.2.2. (a) X-Ray diffraction patterns and (b) Raman spectra for pristine hematite and 0.5%W doped hematite.

To detect the presence of elements in the samples and investigate the electronic structure, XPS

analysis were performed, and the results are shown in Figs. 2.2.3a–c. The Fe 2p region spectra show binding energies of 724.5 eV (Fe $2p_{1/2}$) with a shake-up satellite line at 733.5 eV and other binding energies of 711.1 eV (Fe $2p_{3/2}$) with a shake-up satellite line at 718.8 eV, which is specified to be Fe^{3+} in α-Fe_2O_3 (see Fig. 2.2.5a). As shown Fig. 2.2.5b, the deconvolution O1s spectrum peaks had a high peak at around 530.8 eV that can be corresponds to the Fe-O bonds at around 529.7 eV. The O1s spectrum at around 531.5 eV revealed OH^- in both α-Fe_2O_3 and W:α-Fe_2O_3 samples [13]. In the detecting W spectra, three peaks were observed at 35.1 and 37 for W $4f_{7/2}$ and W $4f_{5/2}$, respectively, which can be attributed to the existence of W nanoparticle in the 0.5W:α-Fe_2O_3 sample (Fig. 2.2.3c).

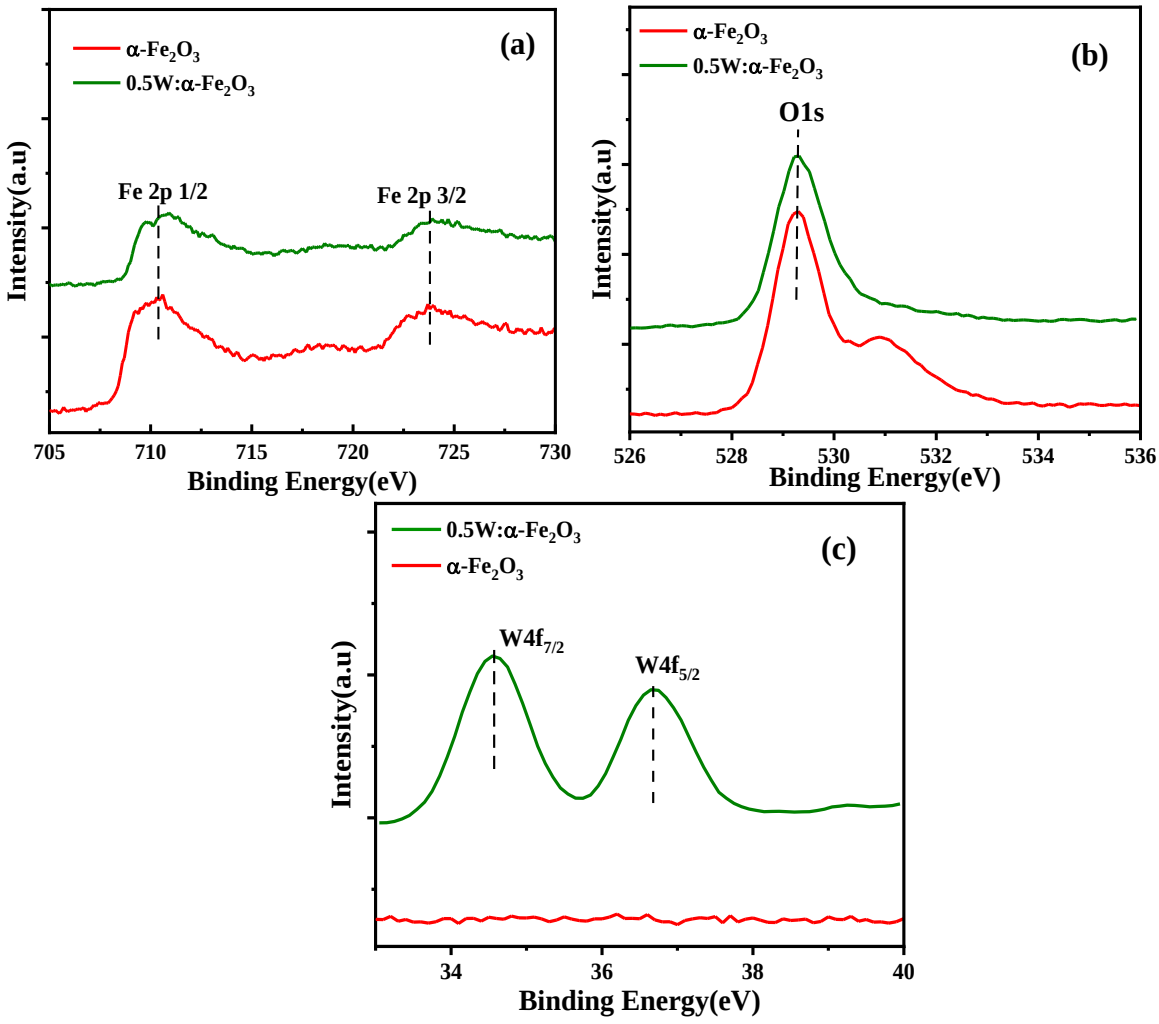

Fig. 2.2.3. (a) XPS survey spectra and high-resolution XPS spectra for (b) Fe 2p (c) O1s and (d) W4f for pristine and 0.5% W doped hematite.

The XPS depth and the electron paramagnetic resonance (EPR) spectra were measured for the 0.5W:α-Fe_2O_3 electrode to further confirm the doping role of W, with the results shown in Fig. 2.2.4a to d, respectively. The W4f intensity signals do not increase significantly with increasing etching times (Figs. 2.2.4a and b), indicating that the homogenous distribution of the W element exists in the structure, thus confirming the doping role for tungsten at the optimum photoelectrode [14, 15]. The EPR results of α-Fe_2O_3, 0.25W:α-Fe_2O_3, 0.5W:α-Fe_2O_3, and 1W:α-Fe_2O_3 photoelectrode are shown in Figs. 2.2.4c and d. It can be easily seen that the g-values of all sample spectra are the same whereas the peak intensities are enhanced for the W doped α-Fe_2O_3 electrodes. The peak intensity of the EPR spectrum is correlated with the concentration of Fe^{3+} and Fe^{2+} ions, which implies that more oxygen vacancies were produced by the doping process of the tungsten. The EPR spectrum shows weak signals centered at g=4.2759 and around g=2.0012 at room temperature. These signals are attributed to the high-spin Fe^{3+} ($S_{5/2}$) and low-spin Fe^{3+} ($S_{1/2}$), respectively [16]. They were also assigned to Fe^{3+} ions coupled via exchange interactions and Fe^{3+} ions in rhombic and axial symmetry sites, respectively. However, the high-intensity signals centered at g = 2.5687 could clearly be observed for the W doped α-Fe_2O_3 samples, particularly 0.5W:α-Fe_2O_3, samples (Fig. 2.2.4c). This change can be linked to the interaction between Fe^{3+} and Fe^{2+} ions caused by a ferromagnetic resonance. It can also be seen that the g-values of all sample spectra remained the same whiles the EPR intensity increased (Fig. 2.2.4d). The EPR data reveals that the structure of α-Fe_2O_3 was not changed after using tungsten as a dopant. Therefore, these results convincingly show that the W doped samples possess more defects than the pure α-Fe_2O_3 electrode [17, 18]. Based on the above discussions, it can be concluded that the role of W could be the metal-doped on the surface of α-Fe_2O_3 photoanode.

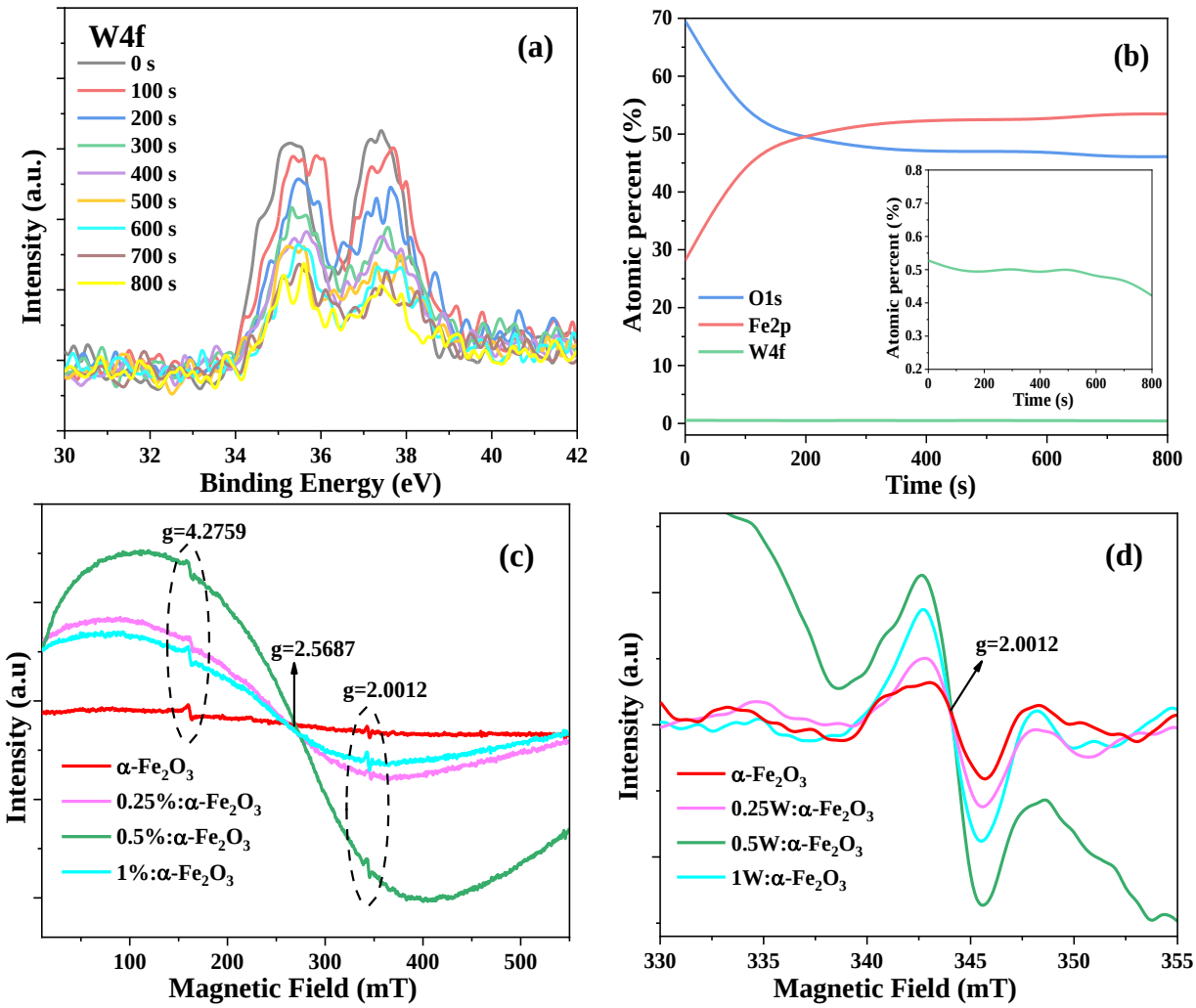

Fig. 2.2.4. (a) XPS depth profiles of W4f in different etching times and (b) XPS depth profiles of W4f, Fe2p, and O1s in the 0.5W:α-Fe_2O_3 photoanode. C and d) Electron paramagnetic resonance (EPR) spectra of the pure α-Fe_2O_3, 0.25W:α-Fe_2O_3, 0.5W:α-Fe_2O_3, and 1W:α-Fe_2O_3 photoanodes.

To evaluate the optical properties of the prepared photoelectrodes, the UV-vis reflectance spectra were measured for the pure α-Fe_2O_3 and W:α-Fe_2O_3 photoanodes (Fig. 2.2.5a). The reflectance of 0.5W:α-Fe_2O_3 are significantly decreased compared to that of the pure α-Fe_2O_3. Further, the slight redshift indicates the presence of tungsten as a dopant, which implies that the absorbance intensity was improved [19, 20]. In addition, the band gap energies of the prepared α-Fe_2O_3, 0.25W:α-Fe_2O_3, 0.5W:α-Fe_2O_3, and 1W:α-Fe_2O_3 thin films are shown in Fig. 2.2.5b. The band gap for α-Fe_2O_3 decreased after doping W from 2.16 to 2.11 eV. Compared to the pure α-Fe_2O_3 photoelectrode, the

W:α-Fe_2O_3 photoelectrodes had a strong absorption spectrum in a wide range of wavelengths. This may be related to the red shift of the light absorption band of the W doped samples that improving the light absorption ability and the photon to charge conversion efficiency [21]. As shown in Fig. 2.2.5c, the W:α-Fe_2O_3 samples could absorb more photons than the pristine α-Fe_2O_3 sample could, and therefore generated more electron-hole pairs. This confirms the improved PEC efficiency under higher wave number (low energy) of visible light irradiation compared with that of pure α-Fe_2O_3. The photogenerated electron-hole recombination rate and charge trapping effect can be detected by analyzing the photoluminescence (PL) spectrum data (Fig. 2.2.5d). The PL spectra of the undoped and doped α-Fe_2O_3-based thin films were measured under an excitation range from 450 nm to 600 nm with a 10 nm interval. The intensity of the PL for 0.5W:α-Fe_2O_3 was substantially weaker than those of the other samples of pure α-Fe_2O_3, as well as 0.25 and 1%W doped Tungsten (Fig. 2.2.5d). These results implied reductions in recombination and charge trapping of photogenerated electron-hole pairs in the samples [22, 23].

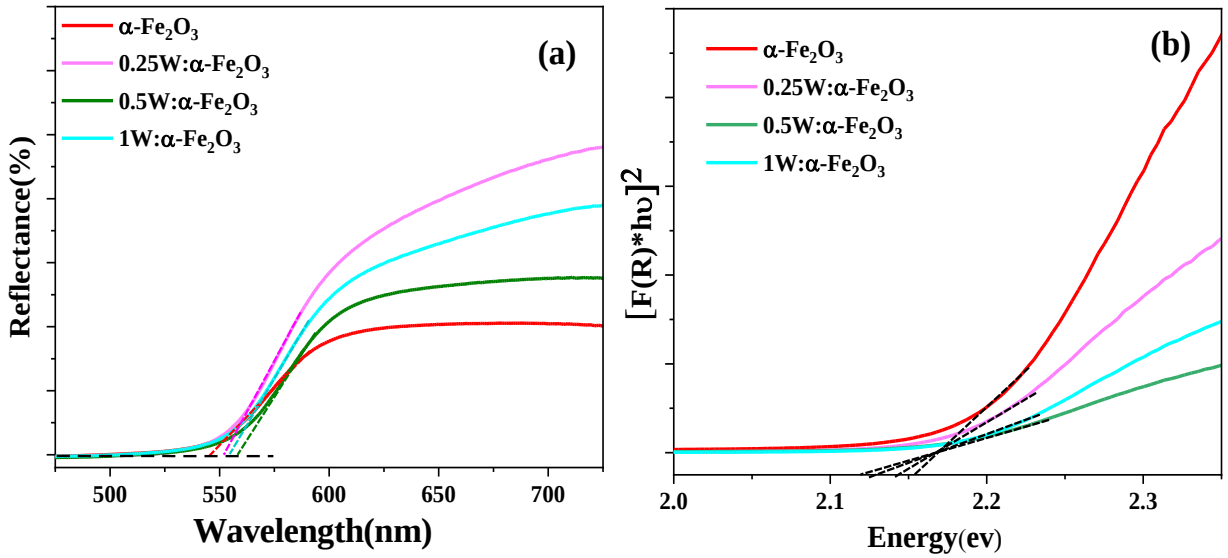

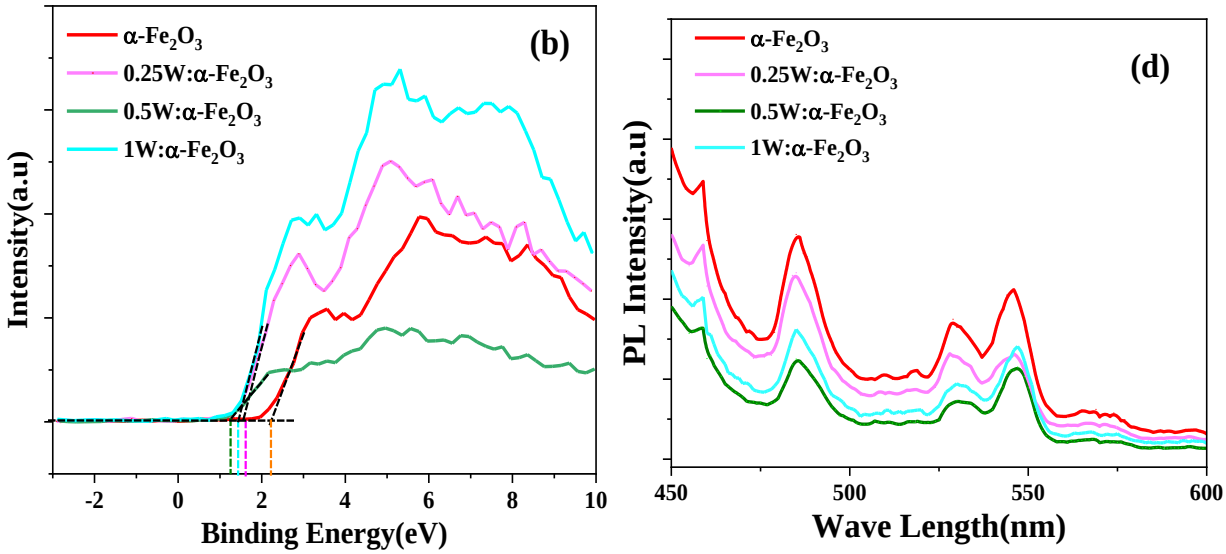

Fig. 2.2.5. (a) UV–vis reflectance spectra and (b) band gap energies, (c) XPS for VB, and (d) PL of pure α-Fe_2O_3, 0.25W:α-Fe_2O_3 , 0.5W:α-Fe_2O_3, and 1W:α-Fe_2O_3.

2.2.3.2. Photoelectrochemical (PEC) measurements

Figs.2.2.6a and b show linear scan voltammetry (LSV) and chopped LSV of the pure α-Fe_2O_3, 0.25W:α-Fe_2O_3 , 0.5W:α-Fe_2O_3, and 1W:α-Fe_2O_3 electrodes under continuous and on-off cycling between 0.3-1.7 V vs. RHE. In the dark condition, the photocurrent density is around zero for all samples. After starting illumination, photoelectron-hole pairs generated in the photoanode α-Fe_2O_3, 0.25W:α-Fe_2O_3 , 0.5W:α-Fe_2O_3, and 1W:α-Fe_2O_3 electrodes and this photocurrent is dependent to applied voltage in which the higher voltage is applied the more photoelectron can be collected [24]. As shown in Fig.2.2.6a, pure α-Fe_2O_3 shows low photo response with a photocurrent density reaching 0.07 mA cm^{-2} at 1.23 V vs. RHE. This can be attributed to high rate of recombination of electron and hole due to poor electron mobility inside bulk α-Fe_2O_3 [25]. After doping a small amount of tungsten (0.25, 0.5, and 1%W:α-Fe_2O_3), the photocurrent density is substantially increased, in particular for the 0.5 W:α-Fe_2O_3 electrode which peaks at around 0.5 mA.cm^{-2} at 1.23 V vs. RHE (more than 7-fold greater than that of pure α-Fe_2O_3). The significant enhancement of PEC performance at low W atomic percentage in α-Fe_2O_3 is attributable to the improved electrical

conductivity of α-Fe_2O_3, increased charge separation and reduced charge recombination rate [26]. Furthermore, after W doping, the onset potential shifted significantly to a lower applied voltage. However, the further addition of W (1% W:α-Fe_2O_3) beyond the optimal W loading decreased the photocurrent density due to the existing defects and traps in the photoanodes functioning as recombination centers [27].

Figs. 2.2.6c and d show the photocurrent response and photostability results of the pure α-Fe_2O_3, 0.25W:α-Fe_2O_3 , 0.5W:α-Fe_2O_3, and 1W:α-Fe_2O_3 photoelectrodes for 4 cycles at a constant potential of 1.23 V vs. RHE. Clearly, 0.5 W:α-Fe_2O_3 shows the highest photocurrent intensity among all samples. The photocurrent of 0.5 W:α-Fe_2O_3 with good stability over time is ~7-, 3-, and 2-fold higher than that of pure α-Fe_2O_3, 0.25W:α-Fe_2O_3, and 1W:α-Fe_2O_3, respectively. This indicates that the optimum W content (0.5%) in α-Fe_2O_3 could create greater strength in the separation and transfer of electron–hole pairs compared with undoped or higher W-atomic percentage α-Fe_2O_3 [28].

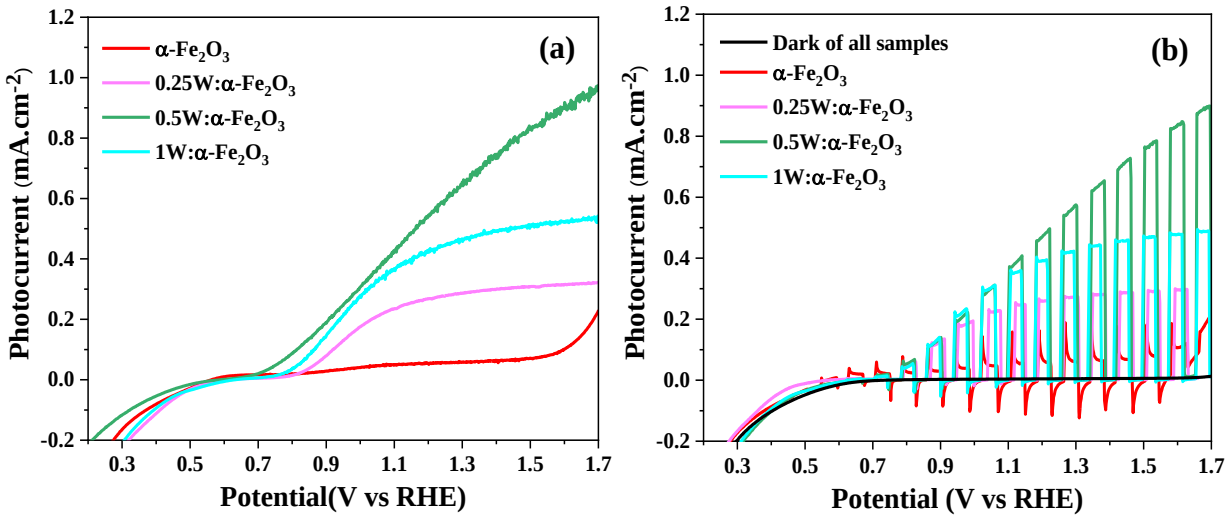

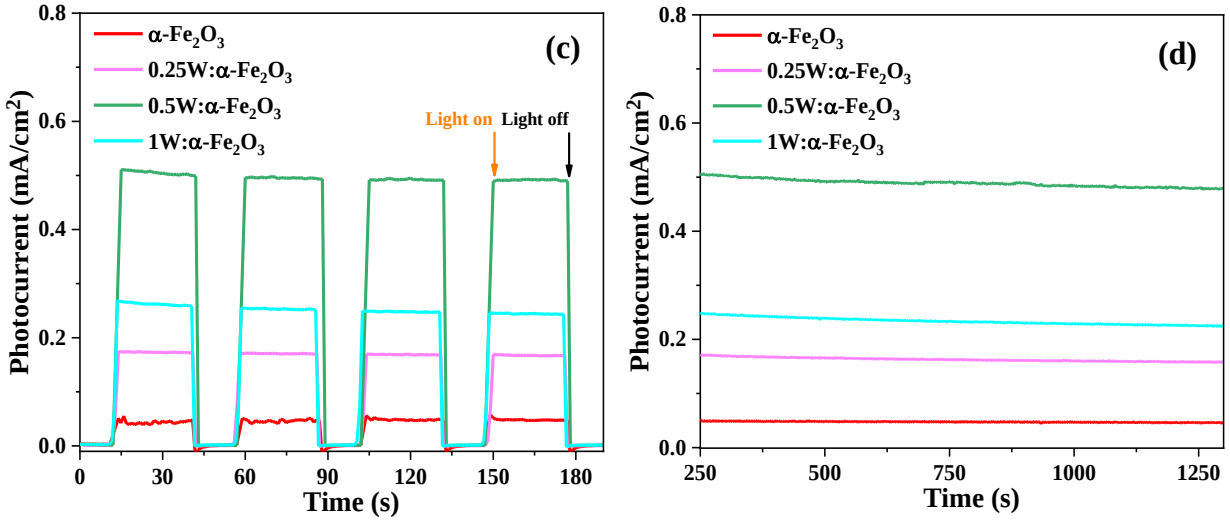

Fig. 2.2.6. (a) Linear scan voltammetry and (b) chopped LSV vs. potential linear from 0.3 to 1.5 V vs. RHE, (c) photocurrent response, and (d) photocurrent stability at 1.23 V vs. RHE for pure α-Fe_2O_3, 0.25W:α-Fe_2O_3 , 0.5W:α-Fe_2O_3, and 1W:α-Fe_2O_3 under 100 $mWcm^{-2}$ illumination. The electrolyte was a 1 M NaOH.

The IPCE result in Fig. 2.2.7a obtained at 1.23 V vs. RHE shows that the photon conversion efficiency increased for 0.5W:α-Fe_2O_3 compared to α-Fe_2O_3 which is in good agreement with photocurrent and absorption results [29].

The open circuit potential is measured to show the improvement in carrier-separation for α-Fe_2O_3 and 0.5W:α-Fe_2O_3 photoelectrodes. Figure 2.2.7b shows the change in open circuit potential (Δ OCP) versus light illumination density. As it can be observed in Fig.7b, the ΔOCP value for 0.5W:α-Fe_2O_3 increased more than pure α-Fe_2O_3 indicating a photogenerated electrons production in 0.5W:α-Fe_2O_3 due to less recombination [30].

The charge carrier mobility plays an important role in the PEC performance of α-Fe_2O_3. The electrochemical impedance spectroscopy (EIS) was conducted for α-Fe_2O_3 and W:α-Fe_2O_3 (0.25, 0.5, and 1%) (Fig. 2.2.7c), to study the charge carrier mobility of photoanodes. The imaginary data (Z_{imag}) of impedance for W:α-Fe_2O_3 reduced as compared with pure α-Fe_2O_3, leads to smaller semicircle radius. Fig. 2.2.7c shows that the 0.5W:α-Fe_2O_3 sample has the smallest semicircle

radius, which indicates the smallest electron transfer resistance (R_{ct}) and the highest conductivity for photogenerated carriers transport among the tested W:α-Fe_2O_3 photoanodes. Thus, the efficient charge transfer at the interface between the photoanode and the electrolyte prevents the charge carrier recombination and induces easy charge transport of electrons through the photoanode [31].

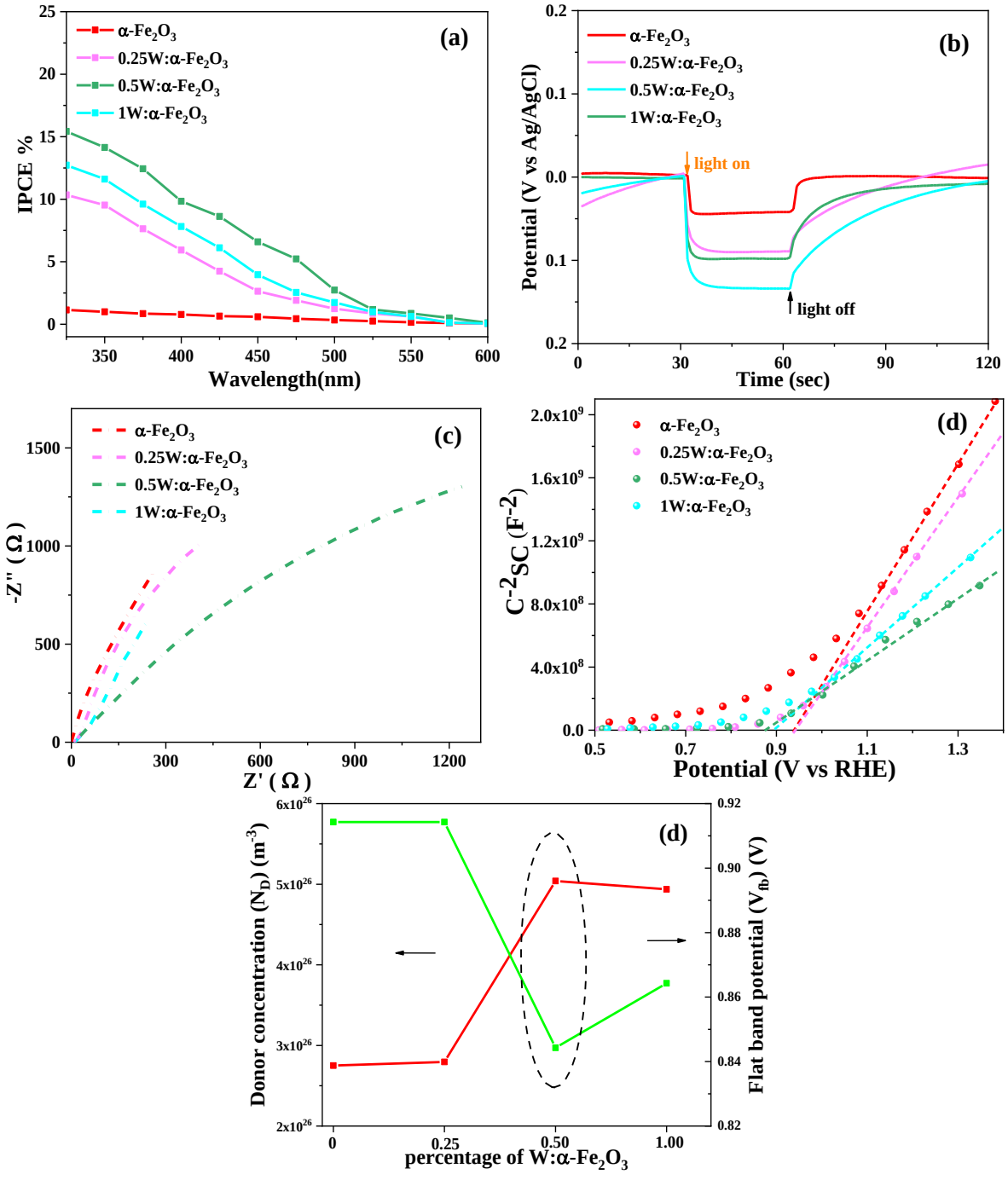

Fig. 7. (a) The incident-photon-to-current-efficiencies (IPCE), (b) change in open circuit potential (ΔOCP) value, (c) Nyquist plot, (d) Mott–Schottky analysis, and (e) the relationship between Donor concentration (N_D) and V_{fb} for pure α-Fe_2O_3, 0.25W:α-Fe_2O_3 , 0.5W:α-Fe_2O_3, and 1W:α-Fe_2O_3 under 100 $mWcm^{-2}$ illumination. The supporting electrolyte was a 1 M aqueous solution of NaOH.

Donor concentration (N_D) and flat band potential energy level are among the most important factors explaining the enhanced photocatalytic and PEC activities for semiconductors. To extract the N_D and V_{fb}, the Mott-Schottky plots were plotted by assuming ideal semiconductor characteristics using equation (4)

$$\frac{1}{C^2} = \frac{2}{\varepsilon\varepsilon_0 A^2 e N_D}\left(V - V_{fb} - \frac{K_B T}{e}\right) \quad (4)$$

where V is the CB potential (V), V_{fb} the flat band potential (V), k the Boltzmann constant, T the temperature (K), e the charge of an electron (C), ε the relative permittivity, ε_0 the dielectric constant, N_D the donor concentration per unit volume (cm^3), and C_{sc} the surface charge capacitance (F/cm^2). The Mott–Schottky plot can provide qualitative information on N_D and V_{fb} in which the positive slopes of electrodes indicate n-type semiconductors. Fig. 2.2.7d shows that the 0.5W:α-Fe_2O_3 film has the lowest slope, followed by 0.25%, 0.5% and 1% W:α-Fe_2O_3 samples, which show much increased N_D as compared with pure α-Fe_2O_3. Moreover, the V_{fb} was shifted to a negative value after doping W (V_{fb} pure α-Fe_2O_3 =0.91V_{RHE} and V_{fb} 0.5W:α-Fe_2O_3 =0.84 V_{RHE}), indicating the presence of more surface states which can lead to a significant change in the band position. The newly generated surface states in the 0.5W:α-Fe_2O_3 photoanode could contribute to the visible light response in the photocurrent action spectrum [32].

2.2.4. Conclusion

Following the facile and cost-effective preparation of photoanodes by a hydrothermal and drop casting method with different W atomic percentages in α-Fe_2O_3 photoanode, this study has estimated the key PEC parameters and investigated the PEC performance of the photoanodes

according to their W atomic percentage. The optimized 0.5W:α-Fe_2O_3 photoanode exhibited the greatest improvement in the PEC performance, at about 7-fold higher than that of pure α-Fe_2O_3 (0.5 mA/cm^2 at 1.23 V vs. RHE), which demonstrated its significant light harvesting and charge transport characteristics. The notable enhancement of the PEC properties is attributed to the synergistic effect of the incorporated W doping, which contributes to the interface formation wherein the efficient separation, transport, and utilization of the charge carriers (e−/h+) can occur. Mott-Schottky and EIS analyses supported that adding W in pure α-Fe_2O_3, particularly 0.5%W, greatly increased the N_D and decreased V_{fb}, W_{SCL} and R_{ct}. The favorable changes in these key parameters all combined to improve the PEC performance of W:α-Fe_2O_3 electrodes.

Reference

[1] P. Ciambelli, M. Sarno, D. Scarpa, 11 Photoelectrocatalytic H2 production: current and future challenges, Hydrogen Production and Energy Transition, (2021) 401.
[2] J. Liqiang, Q. Yichun, W. Baiqi, L. Shudan, J. Baojiang, Y. Libin, F. Wei, F. Honggang, S. Jiazhong, Review of photoluminescence performance of nano-sized semiconductor materials and its relationships with photocatalytic activity, Solar Energy Materials and Solar Cells, 90 (2006) 1773-1787.
[3] G. Longo, F. Fresno, S. Gross, U.L. Štangar, Synthesis of BiVO4/TiO2 composites and evaluation of their photocatalytic activity under indoor illumination, Environmental Science and Pollution Research, 21 (2014) 11189-11197.
[4] F. Kiani, N.A. Astani, R. Rahighi, A. Tayyebi, M. Tayebi, J. Khezri, E. Hashemi, U. Rothlisberger, A. Simchi, Effect of graphene oxide nanosheets on visible light-assisted antibacterial activity of vertically-aligned copper oxide nanowire arrays, Journal of colloid and interface science, 521 (2018) 119-131.
[5] L. Yu, Y. Zhang, J. He, H. Zhu, X. Zhou, M. Li, Q. Yang, F. Xu, Enhanced photoelectrochemical properties of α-Fe2O3 nanoarrays for water splitting, Journal of Alloys and Compounds, 753 (2018) 601-606.
[6] L. Long, G. Lv, Q. Han, X. Wu, Y. Qian, D. Wang, Y. Zhou, Z. Zou, Achieving Direct Z-Scheme Charge Transfer through Constructing 2D/2D α-Fe2O3/CdS Heterostructure for Efficient Photocatalytic CO2 Conversion, The Journal of Physical Chemistry C, (2021).
[7] Y.-S. Hu, A. Kleiman-Shwarsctein, A.J. Forman, D. Hazen, J.-N. Park, E.W. McFarland, Pt-doped α-Fe2O3 thin films active for photoelectrochemical water splitting, Chem. Mater., 20 (2008) 3803-3805.
[8] V. Kumar, D.S. Ahlawat, S.A. Islam, A. Singh, Ce doping induced modifications in structural, electrical and magnetic behaviour of hematite nanoparticles, Materials Science and Engineering: B, 272 (2021) 115327.
[9] W. Li, K. Wang, X. Yang, F. Zhan, Y. Wang, M. Liu, X. Qiu, J. Li, J. Zhan, Q. Li, Surfactant-assisted controlled synthesis of a metal-organic framework on Fe2O3 nanorod for boosted photoelectrochemical water oxidation, Chemical Engineering Journal, 379 (2020) 122256.
[10] A.S.M. Ismail, I. Garcia-Torregrosa, J.C. Vollenbroek, L. Folkertsma, J.G. Bomer, T. Haarman, M. Ghiasi, M. Schellhorn, M. Nachtegaal, M. Odijk, A. van den Berg, B.M. Weckhuysen, F.M.F. de Groot, Detection of Spontaneous FeOOH Formation at the Hematite/Ni(Fe)OOH Interface During Photoelectrochemical Water Splitting by Operando X-ray Absorption Spectroscopy, ACS Catalysis, 11 (2021) 12324-12335.
[11] Y. Guo, T. Liu, N. Wang, Q. Luo, H. Lin, J. Li, Q. Jiang, L. Wu, Z. Guo, Ni-doped α-Fe2O3 as electron transporting material for planar heterojunction perovskite solar cells with improved efficiency, reduced hysteresis and ultraviolet stability, Nano Energy, 38 (2017) 193-200.
[12] S. Shen, C.X. Kronawitter, J. Jiang, S.S. Mao, L. Guo, Surface tuning for promoted charge transfer in hematite nanorod arrays as water-splitting photoanodes, Nano Research, 5 (2012) 327-336.
[13] S. Bai, H. Chu, X. Xiang, R. Luo, J. He, A. Chen, Fabricating of Fe2O3/BiVO4 heterojunction based photoanode modified with NiFe-LDH nanosheets for efficient solar water splitting, Chemical Engineering Journal, 350 (2018) 148-156.
[14] M. Maximov, D. Nazarov, A. Rumyantsev, Y. Koshtyal, I. Ezhov, I. Mitrofanov, A. Kim, O. Medvedev, A. Popovich, Atomic Layer Deposition of Lithium–Nickel–Silicon Oxide Cathode Material for Thin-Film Lithium-Ion Batteries, Energies, 13 (2020) 2345.
[15] Y. Ling, G. Wang, D.A. Wheeler, J.Z. Zhang, Li, Yat, , Sn-doped hematite nanostructures forphotoelectrochemical water splitting. Nano letters11 (2011) 2119-2125.
[16] J. Tang, J. Sánchez Costa, S. Smulders, G. Molnár, A. Bousseksou, S.J. Teat, Y. Li, G.A. van Albada, P. Gamez, J. Reedijk, Two-Step Spin-Transition Iron(III) Compound with a Wide [High Spin-Low Spin] Plateau, Inorganic Chemistry, 48 (2009) 2128-2135.
[17] Z. Zhang, I. Karimata, H. Nagashima, S. Muto, K. Ohara, K. Sugimoto, T. Tachikawa, Interfacial oxygen vacancies yielding long-lived holes in hematite mesocrystal-based photoanodes, Nature Communications, 10 (2019) 4832.
[18] M. Allieta, K. Beranová, M. Marelli, M. Coduri, M. Stefan, D. Ghica, G. Morello, F. Malara, A. Naldoni, Electron Small Polaron and Magnetic Interactions Direct Anisotropic Growth of Silicon-Doped Hematite Nanocrystals, Crystal Growth & Design, 20 (2020) 4719-4730.
[19] M. Orlandi, N. Dalle Carbonare, S. Caramori, C.A. Bignozzi, S. Berardi, A. Mazzi, Z. El Koura, N. Bazzanella, N. Patel, A. Miotello, Porous versus Compact Nanosized Fe(III)-Based Water Oxidation Catalyst for Photoanodes Functionalization, ACS Applied Materials & Interfaces, 8 (2016) 20003-20011.

[20] Z. Zhang, L. Zhang, B. Chen, M. Baek, K. Yong, Efficient Photoconversion and Charge Separation of a (Mn2+-Fe2O3)/Reduced Graphene Oxide/(Fe3+-WO3) Photoelectrochemical Anode via Band-Structure Modulation, ACS Sustainable Chemistry & Engineering, 6 (2018) 13462-13472.
[21] C. Tian, W. Li, Y. Lin, Z. Yang, L. Wang, Y. Du, H. Xiao, L. Qiao, J.-Y. Zhang, L. Chen, Electronic Structure, Optical Properties and Photoelectrochemical Activity of Sn Doped Fe2O3 Thin Films, The Journal of Physical Chemistry C, (2020).
[22] M. Tayebi, Z. Masoumi, B.-K. Lee, Ultrasonically prepared photocatalyst of W/WO3 nanoplates with WS2 nanosheets as 2D material for improving photoelectrochemical water splitting, Ultrasonics Sonochemistry, 70 (2021) 105339.
[23] T. Wang, X. Long, S. Wei, P. Wang, C. Wang, J. Jin, G. Hu, Boosting Hole Transfer in the Fluorine-Doped Hematite Photoanode by Depositing Ultrathin Amorphous FeOOH/CoOOH Cocatalysts, ACS Applied Materials & Interfaces, 12 (2020) 49705-49712.
[24] M. Tayebi, B.-K. Lee, The effects of W/Mo-co-doped BiVO4 photoanodes for improving photoelectrochemical water splitting performance, Catalysis Today, 361 (2021) 183-190.
[25] S.-M. Tao, L.-Y. Lin, Design of efficient Mn-doped α-Fe2O3/Ti-doped α-Fe2O3 homojunction for catalyzing photoelectrochemical water splitting, International Journal of Hydrogen Energy, 45 (2020) 6487-6499.
[26] S. Shen, J. Zhou, C.-L. Dong, Y. Hu, E.N. Tseng, P. Guo, L. Guo, S.S. Mao, Surface engineered doping of hematite nanorod arrays for improved photoelectrochemical water splitting, Scientific reports, 4 (2014) 6627.
[27] M. Tayebi, A. Tayyebi, B.-K. Lee, C.-H. Lee, D.-H. Lim, The effect of silver doping on photoelectrochemical (PEC) properties of bismuth vanadate for hydrogen production, Sol. Energy Mater. Sol. Cells, 200 (2019) 109943.
[28] Q. Rui, L. Wang, Y. Zhang, C. Feng, B. Zhang, S. Fu, H. Guo, H. Hu, Y. Bi, Synergistic effects of P-doping and a MnO2 cocatalyst on Fe2O3 nanorod photoanodes for efficient solar water splitting, Journal of Materials Chemistry A, 6 (2018) 7021-7026.
[29] H.-J. Ahn, K.-Y. Yoon, M.-J. Kwak, J.-S. Lee, P. Thiyagarajan, J.-H. Jang, MoSx supported hematite with enhanced photoelectrochemical performance, Journal of Materials Chemistry A, 3 (2015) 21444-21450.
[30] P.S. Bassi, R.P. Antony, P.P. Boix, Y. Fang, J. Barber, L.H. Wong, Crystalline Fe2O3/Fe2TiO5 heterojunction nanorods with efficient charge separation and hole injection as photoanode for solar water oxidation, Nano Energy, 22 (2016) 310-318.
[31] B.-Y. Chang, S.-M. Park, Electrochemical impedance spectroscopy, Annual Review of Analytical Chemistry, 3 (2010) 207-229.
[32] H. Zhang, G. Wang, D. Chen, X. Lv, J. Li, Tuning photoelectrochemical performances of Ag− TiO2 nanocomposites via reduction/oxidation of Ag, Chemistry of Materials, 20 (2008) 6543-6549.

Chapter 3-Heterojunction

A heterojunction is an interface between two layers or regions of dissimilar semiconductors. These semiconducting materials have unequal band gaps as opposed to a homojunction. It is often advantageous to engineer the electronic energy bands in many solid-state device applications, including semiconductor lasers, solar cells, transistors, and photo-electrochemical water splitting. The first step in thinking about how a semiconductor device operates usually consists of drawing its energy band diagram. Bandgap tuning is an interesting topic in the field of photocatalysis. However, the conduction band (CB) elevation effect induced by quantum size is limited. On the other hand, the formation of heterojunction can obviously promote the CB positions of photocatalysts via the Fermi levels alignment. The hematite (α-Fe_2O_3) has a positive conduction band edge, which can be addressed by the construction of heterojunction with other semiconductors. In this chapter, the α-Fe_2O_3 nanorods heterojunction with TMDs nanosheets were fabricated to enhance photoelectrochemical performance by suppressing the charge recombination, enhances the photogeneration of electron–hole pairs, and facile hole/electron transfer pathways.

This chapter contains one section as follow:

3.1. Hematite (α-Fe_2O_3) heterojunction with molybdenum disulfide (MoS_2)

Chapter 3- Section 1- Heterojunction with Molybdenum disulfide (MoS_2)

Enhanced photoelectrochemical performance of α-Fe_2O_3 photoanode by the construction of heterojunction with molybdenum disulfide (MoS_2)

Abstract:

This study successfully manufactured a p-n heterojunction hematite (α-Fe_2O_3) structure with molybdenum disulfide (MoS_2) to address the electron–hole transfer problems of conventional hematite to enhance photoelectrochemical (PEC) performance. The two-dimensional MoS_2 nanosheets were prepared through ultrasonication-assisted liquid-phase exfoliation, after which the concentration, number of layers, and thickness parameters of the MoS_2 nanosheets were respectively estimated by UV-vis, HRTEM and AFM analysis to be 0.37 mg/ml, 10-12 layers and around 6nm. The effect of heterojunction α-Fe_2O_3/MoS_2 and the role of the ultrasonication process were investigated by the optimized concentration of MoS_2 in the forms of bulk and nanosheet on the surface of the α-Fe_2O_3 electrode while measuring the PEC performance. The best photocurrent density of the α-Fe_2O_3/MoS_2 photoanode was obtained at 1.52 and 0.86 $mA.cm^{-2}$ with good stability at 0.6 V vs. Ag/AgCl under 100mW/cm^2 (AM 1.5) illumination from the back- and front-sides of α-Fe_2O_3/MoS_2; these values are 13.82 and 7.85-times higher than those of pure α-Fe_2O_3, respectively. The results of electrochemical impedance spectroscopy (EIS) and Mott-Schottky analysis showed increased donor concentration (2.6-fold) and decreased flat band potential (by 20%). Moreover, the results of IPCE, ABPE, and OCP analyses also supported the enhanced PEC

performance of α-Fe_2O_3/MoS_2 through the formation of a p–n heterojunction, leading to a facile electron–hole transfer.

3.1.1. Introduction:

The immense global consumption of fossil fuels has led to serious environmental impacts around the world. Many studies have aimed to address these issues by investigating the production of renewable energy resources such as hydrogen gas by using photoelectrochemical (PEC) water splitting technology [1]. This emerging technology can produce more renewable energy by directly harvesting solar energy, leading to reduced air emissions from greenhouse gases. PEC water splitting requires enough energy to cause a reaction in semiconductor materials with valence and conduction band positions that are appropriate for generating hydrogen and oxygen [2]. Semiconductors for PEC should be efficient, environmentally friendly, and nontoxic end products, and they should enable cost-effective energy conversion [3]. Hematite (α-Fe_2O_3) satisfies all these requirements and also has a proper band gap (E_g=2.1 eV) making it a promising candidate for water oxidation [4, 5]. However, bare α-Fe_2O_3 has some limitations in terms of PEC performance, including fast electron-hole recombination, short hole diffusion length (typically 2–4 nm), and low conductivity [6, 7]. Various methods can be used to overcome these drawbacks, such as the application of doping elements to improve electron transport , the inclusion of a heterojunction with other semiconductors to enhance charge separation [8-11], the use of nanostructures to generate more electron–hole pairs, the addition of co-catalysts on the surface to promote charge migration, and other methods to control morphology [12].

Two-dimensional (2D) materials tend to be more reactive to their bulk counterparts, and as they contain unique properties, they have the potential to reveal intriguing new phenomena [13]; transition-metal dichalcogenides (TMDs) are one of the most noteworthy examples of the type of

material. In the type MX_2, M is a transition metal atom and X is a chalcogen atom. The unique combination of a direct bandgap, favorable mechanical and electronic properties, and strong spin–orbit coupling makes them more attractive for applications in optoelectronics, electronics, and energy harvesting materials [14]. Molybdenum Disulfide (MoS_2) is one of the most attractive and widely used TMDs; it has desirable properties, such as a low coefficient of friction, high chemical stability, and thermal stability, and can thus enhance visible light absorption with a proper band edge [15]. When changing from a bulk material to a 2D material, the bandgap length is modified from an indirect bandgap of 1.4eV to a direct bandgap of 2eV. This change in the bandgap makes it an extremely interesting material for a wide range of applications [16]. The use of MoS_2 could also improve the separation of photogenerated electron-hole pairs in the α-Fe_2O_3 photoanode [17, 18].

In this section, we synthesized MoS_2 nanosheets using a liquid exfoliation method. A p–n junction of α-Fe_2O_3/MoS_2 was fabricated on FTO substrate with two simple hydrothermal and drop casting processes. Further, the effect of the ultrasonication process on PEC performance was investigated for α-Fe_2O_3/MoS_2 electrodes prepared with and without the ultrasonication process. The best PEC performance of α-Fe_2O_3/MoS_2 was achieved by optimizing the amount and the thickness of the MoS_2 in the p–n heterojunction. We confirmed that the p–n junction effect of MoS_2 in α-Fe_2O_3 improved the PEC performance.

3.1.2. Experimental section:

3.1.2.1. Preparation of α-Fe_2O_3 photoanode:

The PEC cells were manufactured using FTO (Fluorine Doped Tin Oxide Coated Glass, 25mm×25mm×2.2mm, ~7ohm/sq) as the substrate and washed with deionized water, ethanol, and acetone in equal volumes for 15 min, then dried for subsequent use. α-Fe_2O_3 thin films were

manufactured through a hydrothermal method, typically using an aqueous solution of 1 M $NaNO_3$ and 0.15 M $FeCl_3.6H_2O$ as precursor. After mixing these solutions, hydrochloric acid (HCl) was added dropwise to regulate the pH of the mixture to 1.5. The cleaned FTO was placed at the bottom of a Teflon container, and 80ml of the solution was added into this container. Then, the autoclave was placed in an oven at 100°C for 6 h. After the autoclave had cooled down, the coated FTO were taken out, and the residues on the surfaces of the samples were washed off with deionized water. The yellowish layer that was coated on the FTO was β-FeOOH. To transform the β-FeOOH into α-Fe_2O_3 and to prepare the α-Fe_2O_3 photoanode, the FTO coated with β-FeOOH was placed in a furnace in air at 550°C for 4 h.

3.1.2.2. Preparation of 2D-MoS_2 nanosheet by ultrasonication:

The MoS_2 nanosheets were synthesized via a liquid exfoliation method, as shown in a schematic in Fig. 1. First, 300 mg of MoS_2 powder was added into the solution prepared by combining 45 ml Ethanol with 55 mL water as a solvent. The exfoliated MoS_2 nanosheets precursor was sonicated continuously for five days. The dispersions were centrifuged at 3500 rpm for 60 min to separate MoS_2 nanosheets. Then, the supernatant containing thin MoS_2 nanosheets were collected from the top of the solution.

3.1.2.3. Preparation of α-Fe_2O_3/MoS_2 thin film:

The p-n heterojunction between these two semiconductors of α-Fe_2O_3 and MoS_2 was manufactured through a simple and low-cost drop casting method. We dropped 100 µl of liquid exfoliation MoS_2 nanosheets solution on to the surfaces of the α-Fe_2O_3 photoanodes, then placed them in a furnace for 5 min at 450˚C. We repeated the drop casting process under the same conditions four, eight, and 12 times, and the resulting samples were labeled α-Fe_2O_3/4-MoS_2, α-Fe_2O_3/8-MoS_2, and α-Fe_2O_3/12-MoS_2, respectively. Finally, all the heterojunction samples of the α-Fe_2O_3/MoS_2

photoanodes were calcined in a furnace for 2 h at 450°C.

3.1.2.4. Characterization Measurement:

The morphologies and structures of the samples were characterized by a scanning electron microscope (SEM, Model Quanta 250 FEG) and a transmission electron microscope (TEM, JEOL, JEM-2100F). Structure and crystallinities of the different catalytic films were characterized by X-ray diffraction (XRD). The X-ray source was Bruker D8Advance with monochromatic Cu Kα radiation (λ=1.5406 Å) in the 2θ range of 10–55°. Raman spectra was used with the laser line at 785 nm as the excitation source at room temperature (Bruker, model: Senteraa 2009, Germany). The chemical states of the component elements in the film samples were investigated using a Thermo Scientific Sigma Probe spectrometer with a monochromatic AlKα source (photon energy 1486.6 eV), a spot size of 400 μm, an energy step size of 1.0 eV, and a pass energy of 200 eV. The optical properties of the photoanodes were measured by Perkin Elmer UV-Vis-NIR model Lambda 950 and photoluminescence (PL) spectra (Edinburgh F-4600 NF900 (FLS920) fluorescence spectrophotometer) at 400 nm excitation.

3.1.2.5. Photoelectrochemical (PEC) Measurement:

A standard three-electrode structure was used for PEC measurements. The pure α-Fe_2O_3 and modified α-Fe_2O_3/MoS_2 heterojunction photoelectrodes were used as working electrodes, a platinum wire was used as a counter electrode, and Ag/AgCl was used as a reference electrode in 1 M NaOH electrolyte. The PEC performance was measured under 100mW/cm^2 (AM 1.5) an illumination from a 300W Xe lamp from the front- and back-sides of the photoanodes in the voltage range of -0.7 to 0.7 V (vs. Ag/AgCl). EIS was measured with the usage of potentiate by the identical electrode formation. IPCE measurements were also taken using different filters in this

system at 0.6V(vs. Ag/AgCl) under 100mW.cm^{-2} (AM 1.5) illumination to investigate the conversion ratio of the incident photon to electron.

3.1.3. Results and discussion

3.1.3.1. Structural characterization

One method used to investigate the van der Waals interactions in 2D materials is atomic force microscopy (AFM). The optical absorption of MoS_2 can be seen from the near-infrared (NIR) to the ultraviolet (UV) region because of its electronic band structure. Points A, B, and C shown in Fig. 3.1.2a imply the existence of MoS_2 nanosheets. The accumulation of layers slightly influences d-orbitals in the metal atom and causes shifts in the A and B exciton peaks. By increasing the number of layers, the energy difference between excitons B and A increases ($\Delta E = E_B - E_A$) [19]. The C peak occurs in various energies for monolayered versus multilayered materials. The C transitions are attributed to the van der Waals interactions, which require the p-orbitals of the S atoms. In our work, the C peak in MoS_2 is centered at ~397 nm, while the B and A transitions are at ~610 nm and ~670 nm, respectively, with a difference of ~59 nm between their excitons. These results indicate a significant contribution of the few-layered nanosheets [18, 20]. The thicknesses of the MoS_2 nanosheets are estimated using equation (1).

$$\text{Thickness (N (nm))} = 2.3 \times 10^{36} \times exp\left(-{}^{58444}/_{\lambda_A}\right) \quad (1)$$

In this equation, λ_A is the wavelength of the absorbance light at point A in Fig. 3.1.2a. The thickness of the MoS_2 nanosheets exfoliated by an ultrasonication process was found to be around 6 nm, which represents the few layers of nanosheets used.

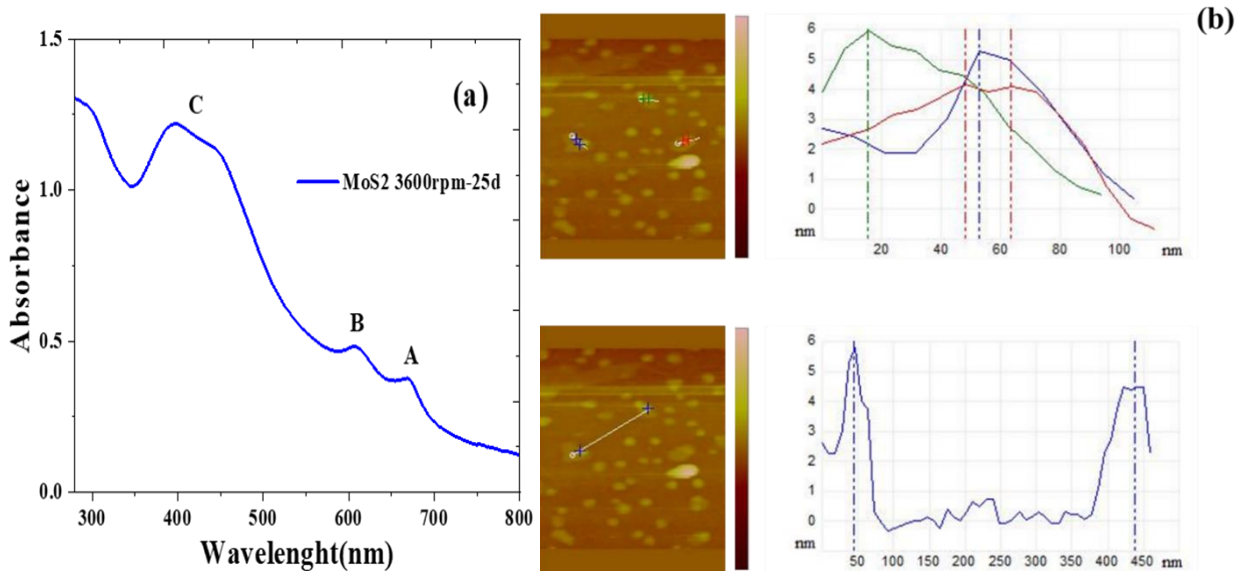

Fig. 3.1.2. (a) UV-Vis and (b) AFM images and height profiles for MoS_2 nanosheets.

The AFM results, specifically the deposited height measurement, can provide a further estimate of the number of MoS_2 nanosheets layers. The average thickness measured from the height profile diagram was estimated to be approximately 4.5-6 nm (Fig. 3.1.2b).

The concentration and length of the exfoliated MoS_2 (C_M) was estimated by Eq. 2 and 3.

$$L(nm) = \frac{(3500\times\frac{EXT_B}{EXT_{345}}-140)}{(11.5-\frac{EXT_B}{EXT_{345}})} \quad (2)$$

$$C\ (mg.\ mL^{-1}) = EXT_{345}/(\alpha\times l) \quad (3)$$

In this equation, L is average size of nanosheets were estimated by EXT_B and EXT_{345} values in UV-vis data. Concentration of the nanosheets depends on EXT_{345} value, the absorption coefficient (α) and the path length (l). Furthermore, the amount of MoS_2 precursor per area of photoelectrode was calculated as shown in Eq. 4:

Amount of MoS_2 nanosheets per area= (Times of drop×100 µl×C_M)/photoelectrode's area (4)

It should be noted that concentrations reported in the cited references may not be the optimal values because the experimental parameters (such as ultrasonic time, centrifuge speed and time) would

greatly affect the obtained product concentration. Further, the length and concentration of the MoS_2 nanosheets on each photoanode were estimated to be 104.74 nm and 0.37 mg/ml, respectively.

Table 1: Amount of MoS_2 nanosheets on the photoelectrodes.

Samples name	Time of drops	Volume of MoS_2 precursor (0.1 ml per each drop cycle)	Concentration of MoS_2 nanosheets in precursor (mg/ml)	Concentration of MoS_2 nanosheets in each photoelectrode (mg/ml)	Amount of MoS_2 nanosheets in photoelectrode's area (mg/cm^2) (FTO area =25mm×25mm)
α-Fe_2O_3-4-MoS_2	**4**	**4×0.1=0.4**	**0.37**	**0.148**	**0.023**
α-Fe_2O_3-8-MoS_2	**8**	**8×0.1=0.8**	**0.37**	**0.296**	**0.47**
α-Fe_2O_3-12-MoS_2	**12**	**12×0.1=1.2**	**0.37**	**0.44**	**0.71**

Fig. 3.1.3a shows TEM images of typical MoS_2 nanosheets prepared using a sonication process in the liquid exfoliation method with a lateral size of 100-150 nm. Figs. 3.1.3b and c show HRTEM images of the MoS_2 layers, which are well accumulated with an interlayer interval of 0.26 nm, corresponding to the (100) lattice planes of the hexagonal MoS_2 phase.

HRTEM analysis in the boundary areas is a common method used to directly distinguish the numbers of layers of the MoS_2 nanosheet [21]. As shown in Fig. 3.1.3c, 10 -12 dark and bright patterns can be seen for the exfoliated MoS_2 nanosheet, indicating that the MoS_2 was accumulated with 10-12 single layers, which is consistent with the AFM results.

The high-resolution TEM image in Fig. 3.1.3d shows that the lattice structure of the MoS_2 nanosheet was not damaged during the sonication process. The electron diffraction pattern shown in the inset in Fig. 3.1.3d indicates that the MoS_2 nanosheet has an acceptable crystallinity for the synthesis process.

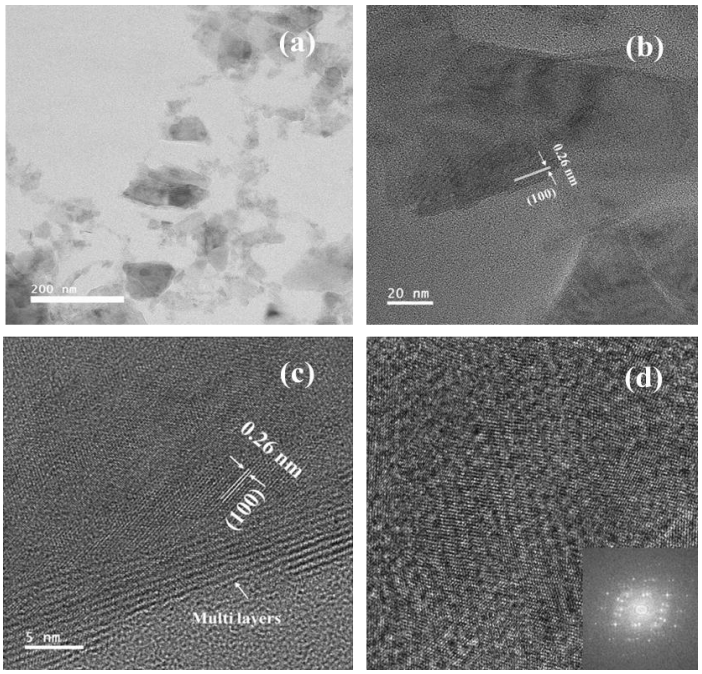

Fig. 3.1.3. a and b) HRTEM images of MoS_2 nanosheets exfoliated by ultrasonication process. c and d) High-resolution TEM images of 10–12-layer MoS_2 nanosheet. The inset in (d) is the corresponding SAED pattern.

The morphologies of the pure α-Fe_2O_3 and α-Fe_2O_3/MoS_2 electrodes were analyzed by SEM, and the results are shown in Fig. 3.1.4(a-d). The optimized sample of the α-Fe_2O_3/MoS_2 confirms that it has the same morphology as the pure α-Fe_2O_3 sample. The α-Fe_2O_3/8-MoS_2 nanorods in Fig. 3.1.4b are denser, and they appear as rice-shaped rods that are both longer and wider [22]. As shown in Fig. 3.1.4c and 3.1.4d, the thicknesses of the pristine α-Fe_2O_3 and α-Fe_2O_3/8-MoS_2 thin films are around 430 and 500 nm, respectively. The concentration of MoS_2 on the surface of the thin films affects the light harvesting of the electrodes when loading more MoS_2 on the surface of the photoelectrode in question. In the HRTEM image of the α-Fe_2O_3 electrode shown in Fig. 3.1.4e, the identified lattice space is 0.23 nm, which is attributed to the lattice plate (110); this was also detected in the XRD analysis results (Fig. 3.1.5a). The thickness of the MoS_2 increased with the dropping of more MoS_2 nanosheets on the surface of α-Fe_2O_3 photoanodes with increased repetitions of drop casting from four to eight to 12 times, respectively denoted as 4-MoS_2, 8-MoS_2, and 12-MoS_2 (Table 1). The evolutions of 0.7 nm, 3.33 nm, and 7.6 nm of the MoS_2 nanosheets

on the α-Fe_2O_3 surface were detected in α-Fe_2O_3/4-MoS_2 (Fig. 3.1.4f), α-Fe_2O_3/8-MoS_2 (Fig. 3.1.4g), and α-Fe_2O_3/12-MoS_2 (Fig. 3.1.4h), respectively. We found that the α-Fe_2O_3/8-MoS_2 photoanode produced a thickness of around 3.33 nm and exhibited the best photocurrent density and PEC performance of all the samples (Fig. 3.1.7a).

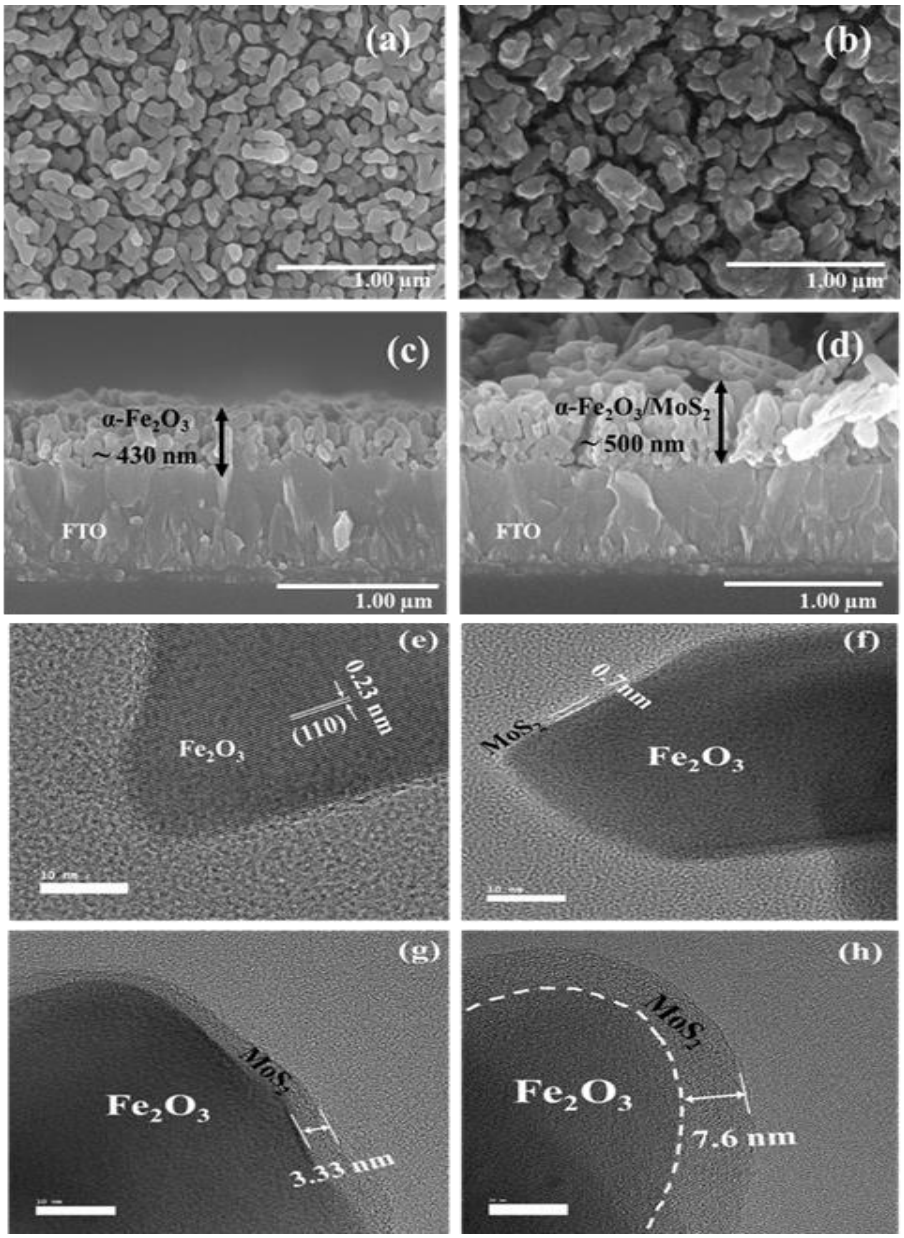

Fig. 3.1.4. Top-view (a and b) and cross-sectional (c and d) FE-SEM images of pure α-Fe_2O_3 (a and c) and α-Fe_2O_3 /MoS_2 (b and d). HRTEM images of (e) α-Fe_2O_3, (f) α-Fe_2O_3/4-MoS_2, (g) α-Fe_2O_3/8-MoS_2, and (h) α-Fe_2O_3/12-MoS_2. The thickness of the MoS_2 layer was controlled by changing the time spent on the drop casting of MoS_2 nanosheets with the same concentration on the FTO/α-Fe_2O_3 electrode.

X-ray diffraction (XRD) analysis was used to investigate the crystallographic structures of the α-Fe_2O_3 and α-Fe_2O_3/8-MoS_2 electrode, and the results are shown in Fig. 3.1.5. Since FTO was used as the substrate, its XRD peaks were detected in all samples (PDF 99-0024). The peaks around 34, 37, 62, and 64° respectively corresponded to the 104, 110, 214, and 300 planes of the α-Fe_2O_3 structure (PDF 02-0915) in both samples. These results confirm that there was no restructuring in the α-Fe_2O_3 photoanode after the addition of the p-n junction with MoS_2 nanosheets. The diffraction peaks at 14.4° and 33.5°,which respectively corresponded to the (002) and (101) planes of MoS_2 (PDF 73-1508), prove the presence of MoS_2 coated on the α-Fe_2O_3 film as heterojunction layers [17, 23]. The Raman spectra of the photoanodes display a dominant band at about 1318 cm^{-1}, which corresponds to the existence of hematite in both structures (Fig. 3.1.5b). The band at (148383, 403 cm^{-1}) further supports the formation of dual α-Fe_2O_3/MoS_2 nanocomposites. In addition, the Raman plot around 1318 cm^{-1} shifts to a higher wavelength after the loading of MoS_2. The red shift for α-Fe_2O_3/8-MoS_2 can be observed, which is attributed to the improved crystallinity of the material, therefore indicating that the material lattice was not compressed [24].

X-ray photoelectron spectroscopy (XPS) spectra were taken to better investigate the elemental compositions of the α-Fe_2O_3/MoS_2 thin films (Fig. 3.1.5c to 5f). The high resolution XPS spectrum with all deconvoluted peaks of Fe 2p shows two peaks at 709.43 and 723.72 eV, which are respectively attributed to Fe $2p_{3/2}$ and $2p_{1/2}$, and these are characteristic of Fe^{2+} in α-Fe_2O_3. Moreover, the distance of 13.8 eV between Fe $2p_{1/2}$ and Fe $2p_{3/2}$ represented the Fe^{3+} ions in α-Fe_2O_3 [25]. Fig. 3.1.5d shows the binding energies of the two distinguishable diffraction O 1s peaks at 529.97 eV (Fe-O) and 532.04 eV (-OH). The oxygen peaks in the α-Fe_2O_3/MoS_2 sample are higher than those in pure α-Fe_2O_3, which may indicate the presence of MoO_3 as a side product of the formation of MoS_2 on the α-Fe_2O_3. Two peaks are shown in the modified sample at 232.46

and 235.54 eV, which respectively correspond to Mo $3d_{3/2}$ and Mo $3d_{5/2}$ and confirm the existence of Mo^{6+} cations in MoS_2. The energy separation between Mo $3d_{5/2}$ and Mo $3d_{3/2}$ is estimated to be 3.08 eV (<3.3 eV), which is indicative of the presence of MoS_2 [26]. S $2p_{1/2}$ and $2p_{3/2}$ peaks appear at around 164 and 163 eV, respectively. In a higher binding energy, the SO_4^{2-} peak shows MoO_3, which formed as a side product during the calcination process of MoS_2 on the hematite substrate [27]. Thus, the XPS data further confirm the existence of MoS_2 in α-Fe_2O_3/MoS_2 film, which is consistent with the XRD results (Fig. 3.1.5a).

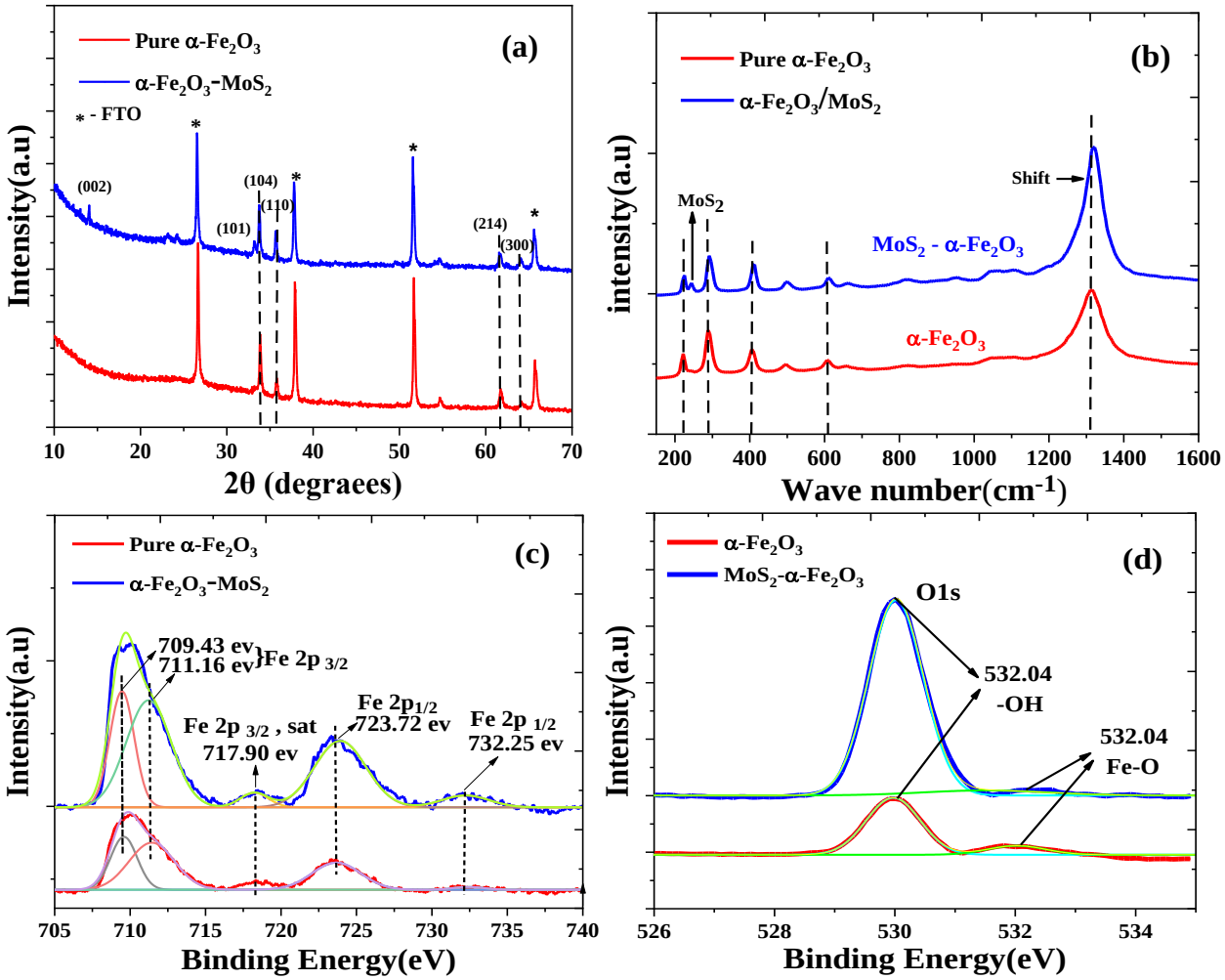

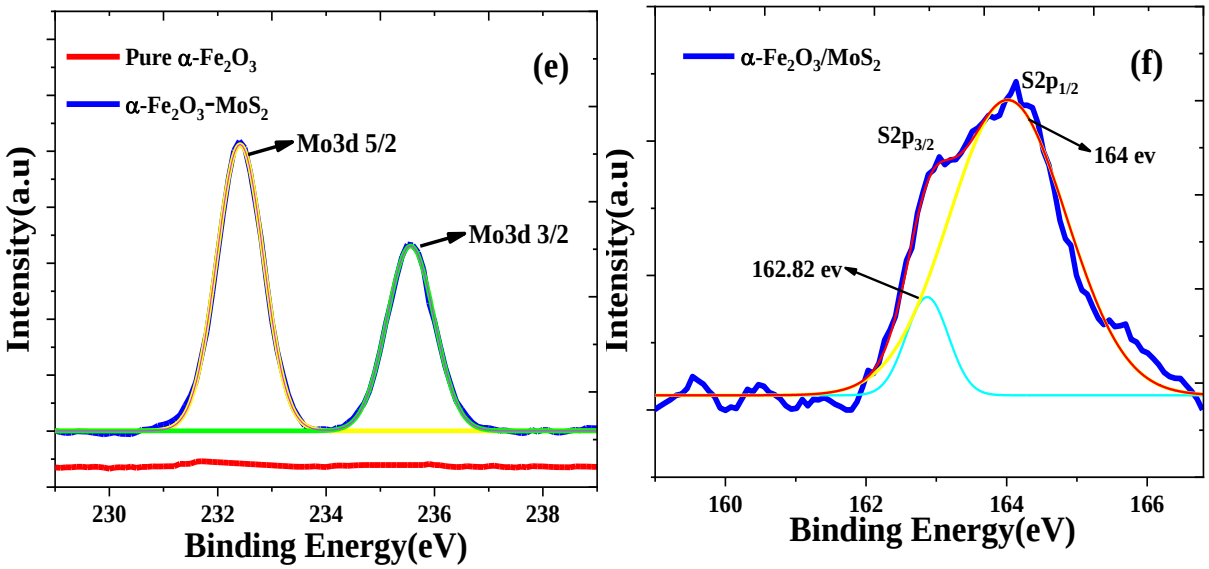

Fig. 3.1.5. (a) X-Ray diffraction peaks and (b) Raman spectra and XPS spectra for (c) Fe 2p (d) O1s (e) Mo3d, and (f) S2p for pure α-Fe_2O_3 and α-Fe_2O_3/MoS_2.

Fig. 3.1.6a shows the optical properties and band-gap energies of α-Fe_2O_3 and α-Fe_2O_3/8-MoS_2. To evaluate the effect of MoS_2, the light absorption ability and photon-to-charge conversion efficiency of the α-Fe_2O_3-based samples are considered. The band gaps estimated for α-Fe_2O_3 and α-Fe_2O_3/MoS_2 films were 2.09 eV and 2.05 eV, respectively. These results confirm that the α-Fe_2O_3/8-MoS_2 electrode is a suitable photocatalytic material due to its high visible light response [25]. Photoluminescence (PL) spectrum analysis can be used to investigate the charge trapping and recombination rate for photogenerated electron-hole pairs in the photocatalyst. The PL intensity of α-Fe_2O_3/MoS_2 thin film is less than that of pure α-Fe_2O_3 between 420 nm to 600 nm (Fig. 3.1.6b). These data indicate the fast electron–hole transfer between α-Fe_2O_3 and MoS_2, which is attributed to the p–n junction present in the α-Fe_2O_3/MoS_2 photoelectrode [28].

Fig. 3.1.6c shows the electron–hole transfer mechanism of the p–n heterojunction in the α-Fe_2O_3/MoS_2 photoelectrode. The band bending achieved equilibrium of the Fermi level when MoS_2 was in contact with α-Fe_2O_3 in the p-n junction. Following visible light illumination, the electrons obtained from electron-hole separation were transferred from the valence band (VB) to

the conduction band (CB) of α-Fe_2O_3 and MoS_2. Due to the difference in energy levels, an electron was transferred from the CB of MoS_2 to the CB of α-Fe_2O_3. The holes were simultaneously driven by the electrostatic field from the VB of α-Fe_2O_3 to the VB of MoS_2, and they reacted with OH to generate O_2 gas. The electrons were led to the Pt electrode via the FTO substrate, and this process produced hydrogen gas. Hence, this inner electrostatic field formed in the p-n heterojunction can increase the extraction of the photo-induced carriers at the space charge region of the p-n junction and can also gain more O_2 and H_2 generation by facilitating the electron-hole separation pathway.

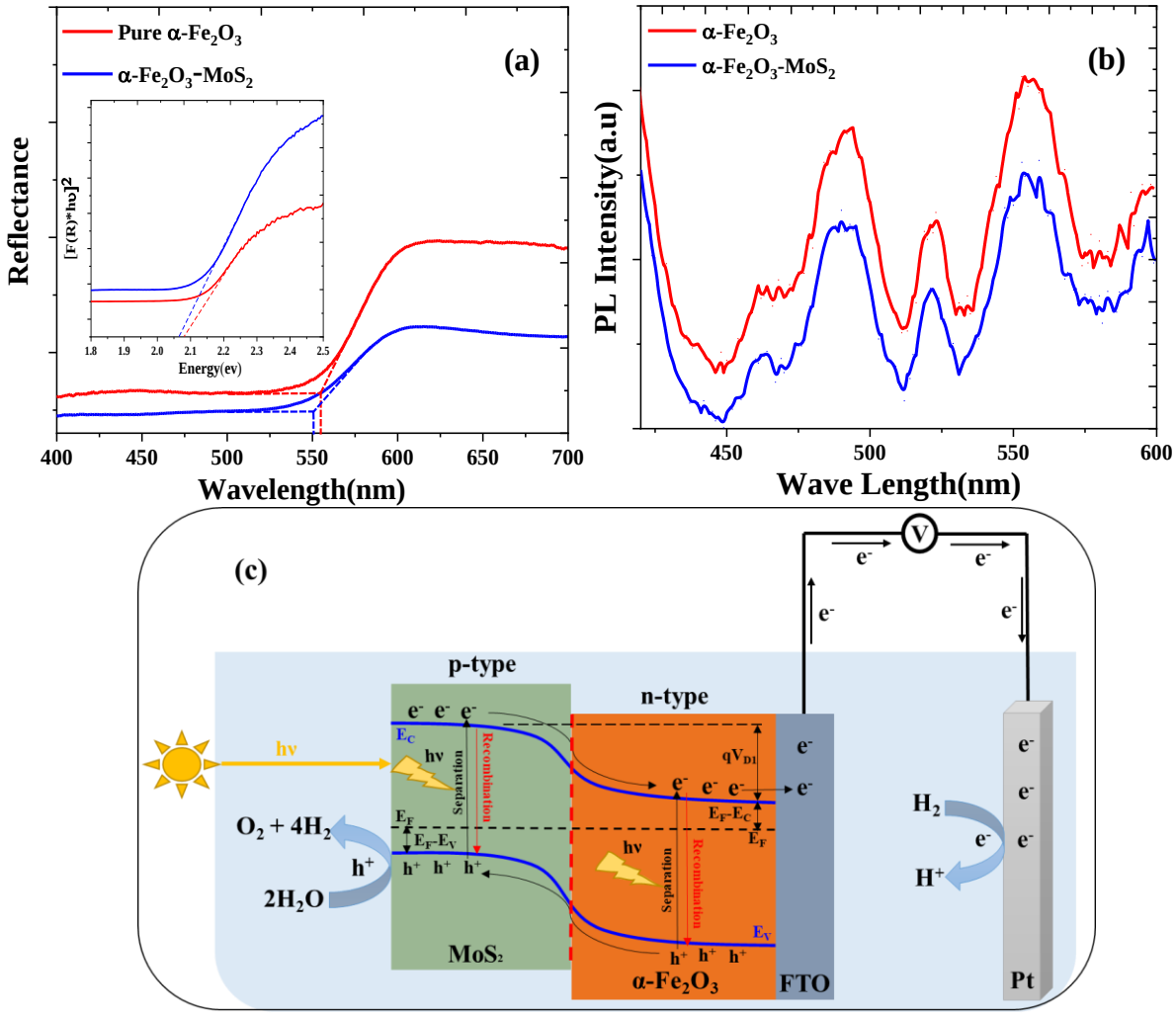

Fig. 3.1.6. (a) UV–Vis reflectance spectra and band gap energies, (b) photoluminescence (PL) spectrum analysis for α-Fe_2O_3 and α-Fe_2O_3α-Fe_2O_3/MoS_2, and (c) mechanism for the p–n heterojunction of α-Fe_2O_3/MoS_2.

3.1.3.2. Effect of MoS_2 nanosheets on the PEC activity of α-Fe_2O_3 photoanode

Linear scan voltammetry (LSV) of the pure α-Fe_2O_3 and α-Fe_2O_3/MoS_2 electrodes were taken under continuous and on-off cycling between -0.6 and 0.6 V vs. Ag/AgCl in 1 M NaOH solution (pH~12), as shown in Fig. 3.1.7a. After starting light illumination, the photoanode photocurrent density reached ~0.11 mA cm^{-2} at 0.6 V vs. Ag/AgCl for the pure α-Fe_2O_3 electrode. The photocurrent density significantly increased after the deposition of MoS_2 nanosheets with the highest value of 0.63 mA cm^{-2} obtained at 0.6 V vs. Ag/AgCl for α-Fe_2O_3/8-MoS_2. This behavior could be attributable to the heterojunction between MoS_2 and α-Fe_2O_3, which improved the charge separation and reduced the recombination of the photogenerated electrons and holes. However, further increases the amount of MoS_2 loaded on the surface of α-Fe_2O_3 gradually decreased the photocurrent density, because excessive MoS_2 may block the light absorption of α-Fe_2O_3 [25, 26]. Moreover, after the deposition of MoS_2 nanosheets, the onset potential significantly shifts from 0.25 V for α-Fe_2O_3 to a lower applied voltage of 0.1 V. This indicates that the α-Fe_2O_3 photoanode underwent a quick reaction to the light and promptly generated photocurrent from zero to its equilibrium value. Chronoamperometry scans were measured for 10 cycles (Fig. 3.1.7b) under intermittent irradiation (30 min light on and 15 min light off) in 1 M NaOH solution, and these confirm the photocurrent responses. The fast and uniform reactions to each light on/off interval of the two electrodes reflect the good producibility of the samples. The pristine α-Fe_2O_3 has a low photocurrent, which implies a low quantum efficiency of α-Fe_2O_3. By contrast, the α-Fe_2O_3/MoS_2 heterostructure shows a higher photocurrent response, which in turn has a positive effect on the decreased recombination for photogenerated charges. As shown in Fig. 3.1.7c, the photocurrent stabilities of different α-Fe_2O_3/MoS_2 films were obtained by continuous illumination after 10 on-off cycles. The photoelectrodes with the p-n heterojunction showed stable photocurrent, even in

30-min light illumination, without any significant downturn.

The photocurrent density depends on many conditions, including the direction of light illumination; back-side illumination significantly increases photocurrent density compared to front-side illumination (Fig. 3.1.7d). The identified photocurrent for α-Fe_2O_3/8-MoS_2 thin film reached ~1.52 mA.cm^{-2}, which was 13.8 and 1.77 times more than that for pure α-Fe_2O_3 and α-Fe_2O_3/8-MoS_2 in front-side illumination, respectively [29, 30].

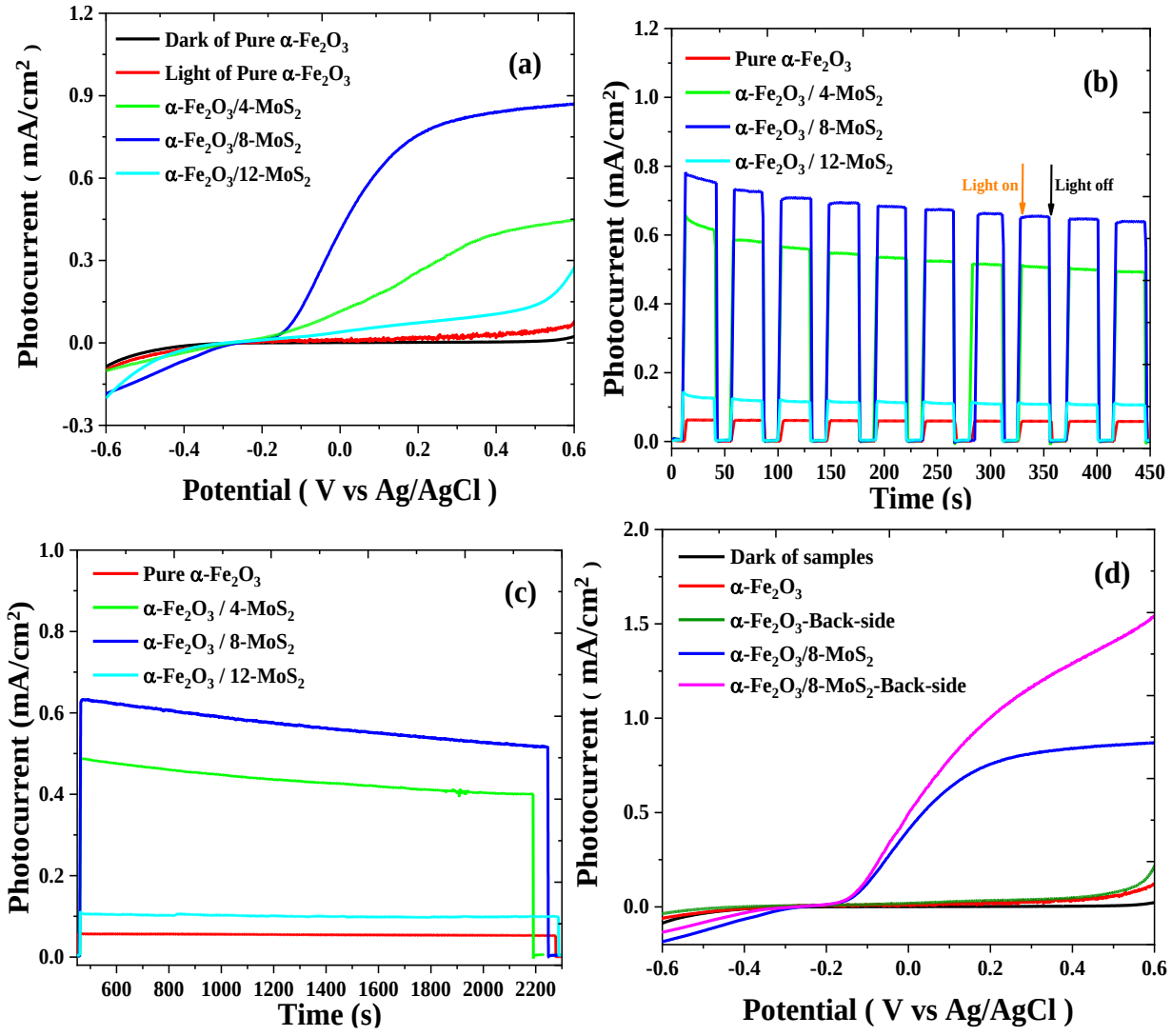

Fig. 3.1.7. (a) Linear scan voltammetry, (b) photocurrent response, (c) photocurrent stability at 0.6 V (vs. Ag/AgCl) , (d) photocurrent density vs. potential linear of α-Fe_2O_3 and α-Fe_2O_3/MoS_2 at potentials from -0.6 to 0.6 V (vs. Ag/AgCl) under 100 mWcm^{-2} back- and front-side illumination. The electrolyte was a 1 M NaOH.

The effect of MoS_2 thickness on the charge transfer process at the α-Fe_2O_3/MoS_2/electrolyte was elucidated using electrochemical impedance spectroscopy (EIS). Fig. 3.1.8a shows that the addition amount of MoS_2 nanosheets reduced the semicircle radius as compared with the pure α-Fe_2O_3 having a relatively very large semicircle. This indicates that the addition of MoS_2 nanosheets on the surface of α-Fe_2O_3 effectively reduced its R_{ct}. Consequently, the α-Fe_2O_3/4-MoS_2 electrodes exhibited higher conductivity for photogenerated carriers transport [31].

The Mott-Schottky plot shown in Fig. 3.1.8c. These represent the charge transport time factor and the electron mobility corresponding to the electron recombination. The donor concentration N_D and the flat band potential V_{Fb} can be respectively obtained from the slope and the intercept on the potential axis of the Mott-Schottky plot. The slopes of the Mott-Schottky curves were significantly reduced after the p-n junction of the α-Fe_2O_3/MoS_2. The N_D in α-Fe_2O_3/8-MoS_2 photoelectrodes (2.07E+27), which has a 2.5-fold higher donor concentration than that of the pure α-Fe_2O_3 (8.11E+26), leading to increased charge carrier transfer and improved PEC performance. Moreover, the qualitative p-type nature of MoS_2 for approving the formation of p–n junctions can be evaluated by the negative slope of Mott–Schottky measurements (Fig. 3.1.8b).

The incident-photon-to-current-efficiencies (IPCE) quantitatively reflect the activity of the photoelectrode at different wavelengths. The IPCE of α-Fe_2O_3 and α-Fe_2O_3/8-MoS_2 were measured under 100 $mWcm^{-2}$ at a bias voltage of 0.6 V (vs. Ag/AgCl) in 1 M NaOH, and they were calculated by placing the appropriate values in equation (5):

$$IPCE, \% = \left(\frac{1240}{\lambda} \times \frac{J_{light}}{P_{light}}\right) \times 100 \quad (5)$$

The steady-state photocurrent density at the wavelength (λ) of incident light (J_{light}) and the light power at the specific wavelengths (P_{light}) were replaced with our measured data. The IPCE values

were obtained in the range from 350 to 600 nm (Fig. 3.1.8d), and they are consistent with the light absorption spectrum results of α-Fe_2O_3 and α-Fe_2O_3/8-MoS_2 (Fig. 3.1.6a). The highest IPCE value (7.6%) was detected at around 325 nm for α-Fe_2O_3/8-MoS_2, which is 7.5 times higher than that of the pure α-Fe_2O_3 electrode (1%). This improvement reflects the successful conversion of the absorbed photons to photocurrent, which is confirmed by the LSV result (Fig. 3.1.7a).

To further elucidate the production behavior of the photogenerated electrons, open current potential (ΔOCP) analysis was conducted (Fig. 3.1.8e). In the figure, higher ΔOCP values represent the higher production of photogenerated electrons and the improved conductivity [32]. As shown in Fig. 3.1.6c, the α-Fe_2O_3/MoS_2 conductivity increased after loading MoS_2 on the surface of α-Fe_2O_3 eight times, and this was attributed to the higher production of photogenerated electrons as well as the substantially reduced electron-hole recombination on the surface of the electrodes.

The applied bias photon-to-current conversion efficiency (ABPE) under different applied potentials was calculated from LSV using equation 6.

$$\text{ABPE (\%)} = \left(\frac{J\left(\frac{mA}{cm2}\right)\times(1.23-Vbias)(V)}{P\left(\frac{mW}{cm2}\right)}\right) \quad (6)$$

In this equation, V is the applied potential; P is the power density of the incident light, 100mW/cm^2 (AM 1.5); and J is the net photocurrent density at different potentials [33, 34]. The ABPE values of all the α-Fe_2O_3 heterojunctions with MoS_2 are higher than those of the pure α-Fe_2O_3 over the measured potential range in a 1 M (pH=14) aqueous solution of NaOH. The highest percentage for ABPE was around 0.132 % at 0.97 V_{RHE} for the α-Fe_2O_3 8layer MoS_2, which is 30.69 times higher than that of pure α-Fe_2O_3 (0.0043%). Therefore, the α-Fe_2O_3/8-MoS_2 photoanode shows the highest photoelectrochemical properties.

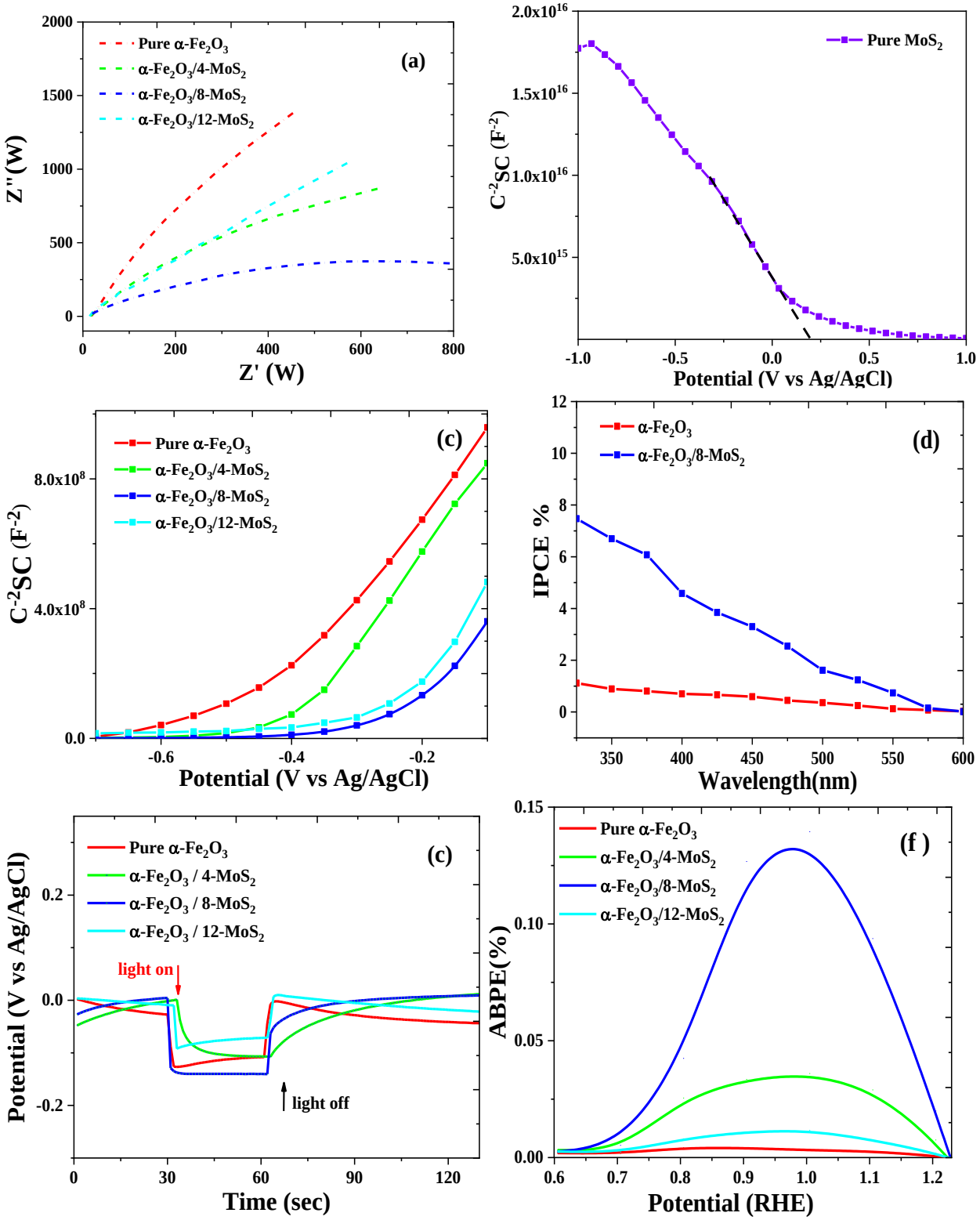

Fig. 3.1.8. (a) Nyquist plot, (b) Mott–Schottky of pure MoS_2, (c) Mott–Schottky plot, (d) IPCE, (e) open circuit potential (ΔOCP), and (f) ABPE plots for pure α-Fe_2O_3 and α-Fe_2O_3/MoS_2 electrodes. The supporting electrolyte was a 1 M aqueous solution of NaOH.

3.1.4. Conclusion

The heterojunction of α-Fe_2O_3 with exfoliated two-dimensional MoS_2 nanosheets, prepared through the ultrasonication process showed an improved PEC performance caused by the facile electron–hole transfer due to the formation of an electrostatic field. The optimized α-Fe_2O_3/MoS_2 with a thin 8-MoS_2 layer (3.3 nm thickness), labeled α-Fe_2O_3/8-MoS_2, showed photocurrent densities of 0.86 and 1.52 $mA.cm^{-2}$ at 0.6 V (vs. Ag/AgCl) in front- and back-side illumination, respectively, which were 7.85 and 13.81 times higher than those of pure α-Fe_2O_3, respectively. The enhanced PEC performance of the α-Fe_2O_3/MoS_2 heterojunction was due to the improved production efficiency of photo-generated electron-hole pairs as well as the decreased resistance caused by the reduced recombination rate of charge carriers and facile hole extraction through the p–n junction. Moreover, the ultrasonication process influenced the photoelectrochemical performance of α-Fe_2O_3/MoS_2 photoanode and increased both light harvesting efficiency and electrical conductivity due to the improved efficient charge transport through the p-n junction.

Reference

[1] M. Tayebi, A. Tayyebi, T. Soltani, B.-K. Lee, pH-Dependent photocatalytic performance of modified bismuth vanadate by bismuth ferrite, New Journal of Chemistry, 43 (2019) 9106-9115.
[2] J. Wang, J. Yang, Z. Zheng, T. Lu, W.J.A.C.B.E. Gao, The role of thin NiPi film for enhancing solar water splitting performance of Ti doped hematite, 218 (2017) 277-286.
[3] O. Monfort, D. Raptis, L. Satrapinskyy, T. Roch, G. Plesch, P. Lianos, Production of hydrogen by water splitting in a photoelectrochemical cell using a BiVO4/TiO2 layered photoanode, Electrochimica Acta, 251 (2017) 244-249.
[4] R. Chong, Y. Du, Z. Chang, Y. Jia, S. Liu, Y. Liu, Y. Zhou, D.J.A.C.B.E. Li, 2D Co-incorporated hydroxyapatite nanoarchitecture as a potential efficient oxygen evolution cocatalyst for boosting photoelectrochemical water splitting on Fe2O3 photoanode, 250 (2019) 224-233.
[5] W. Li, K. Wang, X. Yang, F. Zhan, Y. Wang, M. Liu, X. Qiu, J. Li, J. Zhan, Q.J.C.E.J. Li, Surfactant-assisted controlled synthesis of a metal-organic framework on Fe2O3 nanorod for boosted photoelectrochemical water oxidation, 379 (2020) 122256.
[6] M. Allieta, M. Marelli, F. Malara, C.L. Bianchi, S. Santangelo, C. Triolo, S. Patane, A.M. Ferretti, Š. Kment, A.J.C.T. Ponti, Shaped-controlled silicon-doped hematite nanostructures for enhanced PEC water splitting, 328 (2019) 43-49.
[7] S.R. Pendlebury, X. Wang, F. Le Formal, M. Cornuz, A. Kafizas, S.D. Tilley, M. Grätzel, J.R.J.J.o.t.A.C.S. Durrant, Ultrafast charge carrier recombination and trapping in hematite photoanodes under applied bias, 136 (2014) 9854-9857.
[8] M.B. Lejbini, P.J.O. Sangpour, Hydrothermal synthesis of α-Fe2O3-decorated MoS2 nanosheets with enhanced photocatalytic activity, 177 (2019) 112-117.
[9] J. Deng, X. Lv, K. Nie, X. Lv, X. Sun, J. Zhong, Lowering the onset potential of Fe2TiO5/Fe2O3 photoanodes by interface structures: F-and Rh-based treatments, ACS Catalysis, 7 (2017) 4062-4069.
[10] Y. Wu, J. Ward-Bond, D. Li, S. Zhang, J. Shi, Z. Jiang, g-C3N4@ α-Fe2O3/C photocatalysts: synergistically intensified charge generation and charge transfer for NADH regeneration, ACS Catalysis, 8 (2018) 5664-5674.
[11] N. Thangavel, S. Bellamkonda, A.D. Arulraj, G.R. Rao, B. Neppolian, Visible light induced efficient hydrogen production through semiconductor–conductor–semiconductor (S–C–S) interfaces formed between gC 3 N 4 and rGO/Fe 2 O 3 core–shell composites, Catalysis Science & Technology, 8 (2018) 5081-5090.
[12] X. Zhang, Y. Yang, L. Song, Y. Wang, C. He, Z. Wang, L.J.M.C. Cui, High and stable catalytic activity of Ag/Fe2O3 catalysts derived from MOFs for CO oxidation, 447 (2018) 80-89.
[13] Y. Hou, B. Zhang, Z. Wen, S. Cui, X. Guo, Z. He, J.J.J.o.M.C.A. Chen, A 3D hybrid of layered MoS 2/nitrogen-doped graphene nanosheet aerogels: an effective catalyst for hydrogen evolution in microbial electrolysis cells, 2 (2014) 13795-13800.
[14] D. Geng, H.Y.J.A.M. Yang, Recent advances in growth of novel 2D materials: beyond graphene and transition metal dichalcogenides, 30 (2018) 1800865.
[15] W. Fei, H. Li, N. Li, D. Chen, Q. Xu, H. Li, J. He, J.J.S.E. Lu, Facile fabrication of ZnO/MoS2 pn junctions on Ni foam for efficient degradation of organic pollutants through photoelectrocatalytic process, 199 (2020) 164-172.
[16] L. Zhou, J. Lei, L. Wang, Y. Liu, J. Zhang, Highly efficient photo-Fenton degradation of methyl orange facilitated by slow light effect and hierarchical porous structure of Fe2O3-SiO2 photonic crystals, Applied Catalysis B: Environmental, 237 (2018) 1160-1167.
[17] T. Zhang, H. Zhang, Y. Ji, N. Chi, Y.J.E.A. Cong, Preparation of a novel Fe2O3-MoS2-CdS ternary composite film and its photoelectrocatalytic performance, 285 (2018) 230-240.
[18] Y. Qu, X. Song, X. Chen, X. Fan, G.J.C.E.J. Zhang, Tuning charge transfer process of MoS2 photoanode for enhanced photoelectrochemical conversion of ammonia in water into gaseous nitrogen, 382 (2020) 123048.
[19] K. Novoselov, A. Mishchenko, A. Carvalho, A.C.J.S. Neto, 2D materials and van der Waals heterostructures, 353 (2016) aac9439.
[20] F.M. Pesci, M.S. Sokolikova, C. Grotta, P.C. Sherrell, F. Reale, K. Sharda, N. Ni, P. Palczynski, C.J.A.C. Mattevi, MoS2/WS2 heterojunction for photoelectrochemical water oxidation, 7 (2017) 4990-4998.
[21] D. Gao, M. Si, J. Li, J. Zhang, Z. Zhang, Z. Yang, D. Xue, Ferromagnetism in freestanding MoS 2 nanosheets, Nanoscale research letters, 8 (2013) 129.
[22] Y. Cong, Y. Ge, T. Zhang, Q. Wang, M. Shao, Y.J.I. Zhang, E.C. Research, Fabrication of Z-Scheme Fe2O3–MoS2–Cu2O Ternary Nanofilm with Significantly Enhanced Photoelectrocatalytic Performance, 57 (2018) 881-890.
[23] A. Kagkoura, J. Hernandez-Ferrer, A.M. Benito, W.K. Maser, N.J.C.A.A.J. Tagmatarchis, In-Situ Growth and

Immobilization of CdS Nanoparticles onto Functionalized MoS2: Preparation, Characterization and Fabrication of Photoelectrochemical Cells, (2019).
[24] A. Piazza, F. Giannazzo, G. Buscarino, G. Fisichella, A. La Magna, F. Roccaforte, M. Cannas, F.M. Gelardi, S.J.B.j.o.n. Agnello, In-situ monitoring by Raman spectroscopy of the thermal doping of graphene and MoS2 in O2-controlled atmosphere, 8 (2017) 418-424.
[25] S. Wang, B. Tang, W. Yang, F. Wu, G. Zhang, B. Zhao, X. He, Y. Yang, J.J.J.o.A. Jiang, Compounds, The flower-like heterostructured Fe2O3/MoS2 coated by amorphous Si-Oxyhydroxides: An effective surface modification method for sulfide photocatalysts in photo-Fenton reaction, 784 (2019) 1099-1105.
[26] S.S. Bhat, S.A. Pawar, D. Potphode, C.-K. Moon, J.M. Suh, C. Kim, S. Choi, D.S. Patil, J.-J. Kim, J.C.J.A.C.B.E. Shin, Substantially enhanced photoelectrochemical performance of TiO2 nanorods/CdS nanocrystals heterojunction photoanode decorated with MoS2 nanosheets, 259 (2019) 118102.
[27] Y. Liu, Y.-X. Yu, W.-D.J.T.J.o.P.C.C. Zhang, MoS2/CdS heterojunction with high photoelectrochemical activity for H2 evolution under visible light: the role of MoS2, 117 (2013) 12949-12957.
[28] H.-J. Ahn, K.-Y. Yoon, M.-J. Kwak, J.-S. Lee, P. Thiyagarajan, J.-H.J.J.o.M.C.A. Jang, MoS x supported hematite with enhanced photoelectrochemical performance, 3 (2015) 21444-21450.
[29] P.S. Bassi, L. Xianglin, Y. Fang, J.S.C. Loo, J. Barber, L.H.J.P.C.C.P. Wong, Understanding charge transport in non-doped pristine and surface passivated hematite (Fe 2 O 3) nanorods under front and backside illumination in the context of light induced water splitting, 18 (2016) 30370-30378.
[30] F. Le Formal, S.R. Pendlebury, M. Cornuz, S.D. Tilley, M. Grätzel, J.R.J.J.o.t.A.C.S. Durrant, Back electron–hole recombination in hematite photoanodes for water splitting, 136 (2014) 2564-2574.
[31] H.-J. Ahn, K.-Y. Yoon, M.-J. Kwak, J.-S. Lee, P. Thiyagarajan, J.-H. Jang, MoS x supported hematite with enhanced photoelectrochemical performance, Journal of Materials Chemistry A, 3 (2015) 21444-21450.
[32] M. Tayebi, B.-K. Lee, The effects of W/Mo-co-doped BiVO4 photoanodes for improving photoelectrochemical water splitting performance, Catalysis Today, (2020).
[33] D. Feng, J. Qu, R. Zhang, X. Sun, L. Zheng, H. Liu, X. Zhang, Z. Lu, F. Lu, W.J.J.o.C. Wang, ITO regulated high-performance n-Si/ITO/α-Fe2O3 Z-scheme heterostructure towards photoelectrochemical water splitting, 381 (2020) 501-507.
[34] J.H. Kim, J.-W. Jang, Y.H. Jo, F.F. Abdi, Y.H. Lee, R. Van De Krol, J.S.J.N.c. Lee, Hetero-type dual photoanodes for unbiased solar water splitting with extended light harvesting, 7 (2016) 1-9.

Chapter 4 - Complex Modification

To decrease these drawbacks affecting the PEC performance of α-Fe_2O_3, various techniques have been examined. For instance, doping techniques particularly using metals, have been widely applied to obtain improved PEC performance by increasing the conductivity, lifetime of charge carriers, hole diffuse length and crystallinity. In this chapter, the complex of heterojunction with doping (W:α-Fe_2O_3/MoS_2) and multi-heterojunction (α-Fe_2O_3/$BiVO_4$/MoS_2) were studied, which shows more effective PEC performance. Further, characterization analyses, energy band diagram, and photoelectrochemical measurements are systematically investigated for both studies. This chapter contains two sections as follow:

4.1. Complex of heterojunction with doping (W:α-Fe_2O_3/MoS_2)

4.2. Multi-heterojunction (α-Fe_2O_3/$BiVO_4$/MoS_2)

Chapter 4 - Section 1 - Doping & Heterojunction

Simultaneous Enhancement of Charge Separation and Hole Transfer in a W:α-Fe_2O_3/MoS_2 Photoanode: The Collaborative Approach of MoS_2 as a Heterojunction and W as Metal Doping

Abstract

In this study, a facile approach has been successfully applied to synthesize the W doped-Fe_2O_3/MoS_2 core-shell with unique nanostructure modifications for photoelectrochemical performance. A two-dimensional structure of molybdenum disulfide (MoS_2) and tungsten (W) doped hematite (W:α-Fe_2O_3) overcome the drawbacks of the α-Fe_2O_3 and MoS_2 semiconductor though simple and facile processes to improve photoelectrochemical (PEC) performance. The highest photocurrent density of the 0.5W:α-Fe_2O_3/MoS_2 photoanode is 1.83 mA.cm^{-2}, at 1.23 V vs. RHE under 100mW/cm^2 illumination which is higher than those of 0.5W:α-Fe_2O_3 and pure α-Fe_2O_3 electrodes. The overall water splitting was evaluated by measuring the H_2 and O_2 evolution that after 2h of irradiation for 0.5W:α-Fe_2O_3/MoS_2 was determined 49 and 23.8 μmol.cm^{-2}, respectively. The optimized combination of the heterojunction and metal doping on the pure α-Fe_2O_3 (0.5W:α-Fe_2O_3/MoS_2 photoanode) showed IPCE of 37% and ABPE 26%, which are around 5.2 and 13 times higher than those of 0.5W:α-Fe_2O_3, respectively. Moreover, the facile fabrication strategy can be easily extended to design other oxide/carbon–sulfide/oxide core–shell materials for extensive applications.

4.1.1. Introduction:

The photoelectrochemical (PEC) systems as an approaching way to address the global energy crisis can successfully convert the abundant solar energy harvesting into the storable chemical fuel. The photocatalytic conversion of solar energy into renewable hydrogen fuel via the dissociation of water molecules using a PEC system containing a photoanode and a counter-electrode can enable energy production to zero emissions of pollutants [1]. The major limiting factors affecting the efficiency of solar fuel production include: (i) low light absorption, (ii) poor charge separation and transport and (iii) low surface chemical reaction; substantial efforts have thus gone toward solving these problems[2].

Hematite is one of the most promising metal oxides which have been used as a photoanode in PEC cells. It is not only highly naturally abundant, environmentally friendly, and low cost, but it also has a narrow bandgap (1.9-2.2 eV) and photo-chemical stability [3]. Theoretically, the maximum solar-to-hydrogen [4] efficiency over α-Fe_2O_3 could reach 15.3%, corresponding to a photocurrent density of ca. 12.6 $mA.cm^{-2}$ at 1.23 V vs. RHE under AM 1.5 G. However, the drawbacks of α-Fe_2O_3 result in inconformity in the conduction band edge compared to the redox level of the H_2/H^+ couple [5]. To decrease these drawbacks affecting the PEC performance of α-Fe_2O_3, various techniques have been examined. For instance, doping techniques particularly using metals, have been widely applied to obtain improved PEC performance by increasing the conductivity, lifetime of charge carriers, hole diffuse length and crystallinity. These property improvements are mostly the result of increasing free electrons generation and minimize electron-hole recombination [6]. Another technique for enhancing the PEC performance by reducing the onset potential involves utilizing structural design control , such as nanoparticle, nanowires, nanotubes, nano sheets and three-dimensional inverse opal structures of α-Fe_2O_3 [7]. Further, designing a heterojunction

structure with other catalysts in good coordinated band gap position or using cocatalysts on the surface of α-Fe_2O_3 can also be considered an effective technique for making facile electron-hole transfer route [8]. Specially, having a heterojunction with two-dimensional materials can be effective on the surface passivation of the photoanode by facilitating the extraction of holes from a photoexcited absorber such as semiconductors through the easier charge transfer pathway [9].

This study reports a new and facile construction method for improving the PEC performance of the α-Fe_2O_3 photoanode. Here, α-Fe_2O_3 is newly developed with W doped and heterojunction MoS_2 by using a simple and low-cost drop casting method, then systematically investigated to get elucidate the metal doping and heterojunction effects. The present study demonstrates that W is such a good dopant for improving the activity of the α-Fe_2O_3 photoanodes by enhancing the charge carrier mobility. Subsequently, the development of a facile charge transfer by constructing a heterojunction with MoS_2 nanosheets while optimizing the tungsten content was shown to lead a significant enhancement in PEC performance.

4.1.2. Experimental

4.1.2.1. Preparation of W:αFe_2O_3 photoanode

Akageneite (β-FeOOH) thin layer was coated on fluorine tin oxide (FTO) using a hydrothermal method. An aqueous solution was prepared by mixing 1 M sodium nitrate ($NaNO_3$) and 0.15M ferric chloride ($FeCl_3.6H_2O$) as a precursor and then adding hydrochloric acid (HCl) to adjust the pH to 1.5. Next, the FTO was washed with a mixture of deionized water, acetone and anhydrous ethanol in equal volumes, and then placed in a Teflon container, and had 80ml precursor poured over it. The hydrothermal process was left in an oven at 100°C for 6h. After this, the surface of FTO/β-FeOOH were washed using DI water, and a yellowish layer appeared on the FTO. The samples were placed in a furnace at 550°C for 3 h to produce α-Fe_2O_3 thin film. The α-Fe_2O_3

photoanode was doped with Tungsten (W) through a simple and low-cost drop casting method with W containing species with different amounts of $N_{10}H_{42}W_{12}O_{42}$ in 30ml deionized water. Finally, the W doped α-Fe_2O_3 photoanodes with W content (atomic percentage) were optimized by loading 500µl of the 0.25, 0.5, or 1 % atomic ratio of W precursor on the surface of the α-Fe_2O_3 photoanode, and the resulting photoanodes were labeled 0.25W:αFe_2O_3, 0.5W:αFe_2O_3 and 1W:αFe_2O_3, respectively.

4.1.2.2. Preparation of W:α-Fe_2O_3/MoS_2 photoanodes

The W:α-Fe_2O_3/MoS_2 heterojunction was constructed by dropping the precursor of liquid exfoliation MoS_2 nanosheets onto the surfaces of W:α-Fe_2O_3 photoanodes. The MoS_2 nanosheets were made using 300 mg bulk powder of the MoS_2 which dissolved in 55 mL DI water and 45 ml Ethanol as a solvent and sonicated for continues five days. Further, prepared solution was centrifuged at 3500 rpm for 60 min to make the few layers of MoS_2 nanosheets. Then, the top of the solution containing thin MoS_2 nanosheets was collected for use. For making heterojunction, 800 µl of the few layers exfoliated MoS_2 nanosheets precursor was dropped on W:α-Fe_2O_3 photoanodes, and the W:α-Fe_2O_3/MoS_2 sample was put in the furnace for 3 h at 550°C.

4.1.2.3. Characterization Equipment

The morphologies and structures of the samples were characterized by using scanning electron microscopy (SEM, Model Quanta 250 FEG) and transmission electron microscopy (TEM, JEOL, JEM-2100F). The structures and crystallinities of the different catalytic films were characterized by X-ray diffraction (XRD). The X-ray source was Bruker D8Advance with monochromatic Cu Kα radiation (λ=1.5406 Å) in the 2θ range of 10–55°. A Raman spectrum was used with the laser line at 785 nm as the excitation source at room temperature (Bruker, model: Senteraa 2009, Germany). The chemical states of the component elements in the samples were investigated using

Thermo Scientific Sigma Probe spectrometer with a monochromatic AlKα source (photon energy 1486.6 eV), spot size of 400 μm, energy step size of 1.0 eV and pass energy of 200 eV. The optical properties of the photoanodes were measured by Perkin Elmer UV-Vis-NIR model Lambda 950. Finally, photoluminescence (PL) spectra were detected at room temperature using an Edinburgh F-4600 NF900 (FLS920) fluorescence spectrophotometer at an excitation of 400 nm. Electron paramagnetic resonance (EPR) measurements in the X-band (9.64 GHz) were performed using a CW/Pulse EPR System(QM09). The power 1 mW absorbed by the samples was recorded at room temperature. To measure the time-resolved photoluminescence (TRPL), we used the second harmonic generated beam of a Ti:sapphire laser (800 nm wavelength, 100 fs pulse-width, and 82 MHz repetition rate), which detected by a photomultiplier tube (PMT-100, Becker & Hickl). The luminescence signal from the photomultiplier tube was processed by time-correlated single-photon counting (TCSPC) system (SPC-730, Becker & Hickl) to yield the temporal behavior of FTOs and hematite-based samples. The monitoring window for the TRPL measurements was 590 nm and 469 nm for FTOs and α-Fe_2O_3 s, respectively and the excitation intensity was about 4.7 MW/cm^2.

4.1.2.4. Photoelectrochemical (PEC) Measurement:

The PEC measurements were obtained using a standard three-electrode structure. The pure α-Fe_2O_3, W:α-Fe_2O_3, and W:α-Fe_2O_3/MoS_2 photoelectrodes were utilized as a working electrode and a counter electrode was a platinum wire with an Ag/AgCl reference electrode in 1 M NaOH electrolyte. The applied bias was converted into RHE scale by Eq.1:

$$V_{RHE} = V_{Ag/AgCl} + 0.197 + 0.059 \times pH \quad (1)$$

The PEC performance was measured under an illumination of 100mW/cm^2 from a 300W Xe lamp from the front side of the photoanodes in the voltage range from -0.3 to 1.5 V (vs. RHE). Electrochemical impedance spectroscopy (EIS) was conducted using the various potentials (0.9,

1, and 1.1 V vs. RHE) with the identical electrode formation. Finally, Incident Photon-to-electron Conversion Efficiency (IPCE) were investigated using different filters in this system to find out the conversion ratio of the incident photon to electron at 1.23V(vs. RHE).

4.1.2.4. Hydrogen and Oxygen Evolution Measurement:

The overall water splitting of α-Fe_2O_3, o.5W-α Fe_2O_3 and o.5W-α Fe_2O_3/MoS_2 photoanodes were evaluated by measuring the H_2 and O_2 evolution at 1.23 V versus RHE in 1 M NaOH electrolyte under 100 mW.cm^{-2} irradiations. The amounts of generated oxygen and hydrogen gas were measured by gas chromatography (GC) system (YL Instrument, 6500GC System). Prior to the measurments the water splitting reaction nitrogen gas was purged into cell for 2 h to remove the air remaining in the reaction vessel. The light source was turned on and the amounts of evolved oxygen and hydrogen were measured by a tight syringe every 20 min using a gas chromatograph for 2h. The the resulting peak areas (AreaH_2, AreaO_2) were recorded by injecting gas samples in the GC. The progressed oxygen-hydrogen gases were estimated using the Eq.2 :

$$H_2(or\ O_2)\mu mol.\,cm^{-2} = \left(\frac{Area\ of\ H_2(or\ O_2)peak}{Slope\ of\ calibration\ curve\ for\ H_2(or\ O_2)}\right) \times (Head\ space\ volume) \times \left(\frac{1mol}{24.2\ L}\right) \qquad (2)$$

4.1.3. Results and Discussion

4.1.3.1. Structural characterization

The UV-vis, AFM and TEM graphs for prepared exfoliated MoS_2 nanosheets display in Fig. 4.1.1a-d. The near-infrared (NIR) to the ultraviolet (UV) region can be seen for optical absorption of MoS_2 nanosheets due to the electronic band structure. Positions named C, B, and A in Fig. 4.1.1a indicate the presence of exfoliated MoS_2 nanosheets in the solution. The A and B transitions are at 671.12 nm and 612.65 nm, respectively. The point C in Fig. 4.1.1a were place at 398.34 nm that is also corresponds to the well prepared MoS_2 nanosheets precursor [10]. The length, concentration, and thickness of the exfoliated MoS_2 nanosheets was calculated by equations 1, 2, and 3 are given

in chapter 3-1 [11]. The number of MoS_2 nanosheets were estimated based on the deposited height measurement (Fig. 4.1.1b). Both measured average thicknesses using height profile diagram (Fig. 4.1.1b) and estimated using equation 3 in chapter 2-1 are approximately 6-7 nm. Moreover, the average concentration and length of the MoS_2 nanosheets on each prepared photoelectrodes were estimated to be 0.03 mg/ml and 168.26 nm, respectively.

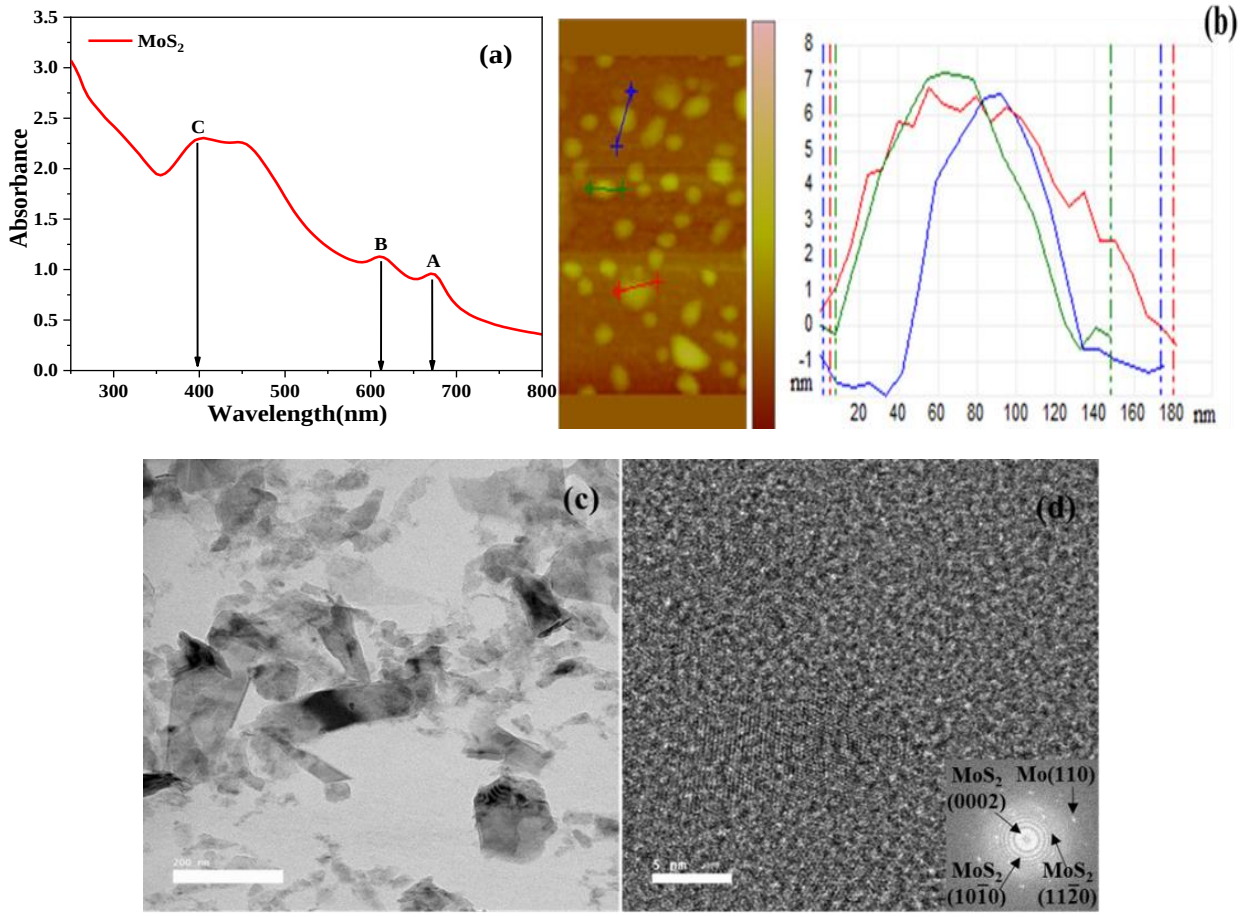

Fig. 4.1.1. (a) UV-Vis, (b) AFM and height profiles, and (c, d) TEM images for MoS_2 nanosheets.

As shown in Fig. 4.1.1c, a lateral size of prepared MoS_2 nanosheets by the liquid phase exfoliation process is approximately 100-150 nm. The lattice structure in high-resolution TEM image (Fig. 4.1.1d) implies the unscathed MoS_2 nanosheets in synthesis process. A polycrystalline film of MoS_2 includes $\{10\bar{1}0\}$, $\{11\bar{2}0\}$, and (0002) indicates in the electron diffraction pattern (inset in

Fig. 4.1.1d) , which confirms few layers of MoS_2 nanosheets with an acceptable crystallinity of the synthesis process [12].

Field emission scanning electron microscope (FESEM) images illustrate the oval shaped α-Fe_2O_3 nanostructure on the FTO, which has a diameter around 50 nm, and a length around 70–150 nm (Fig. 4.1.2). The heterojunction of MoS_2 nanosheets also led to longer thickness (~470nm) and changes the size and condensation of nanorods as compared to pure α-Fe_2O_3 (Fig. 4.1.2b and d). Following the drop-deposition of two-dimensional exfoliated MoS_2 nanosheets on the surface of W:α-Fe_2O_3 films, the surface becomes denser, which can lead to more effective light harvesting, electron-hole separation and facile transfer to the photoelectrode-electrolyte interface due to the existing heterojunction structure in the 0.5W:α-Fe_2O_3/MoS_2 photoanode.

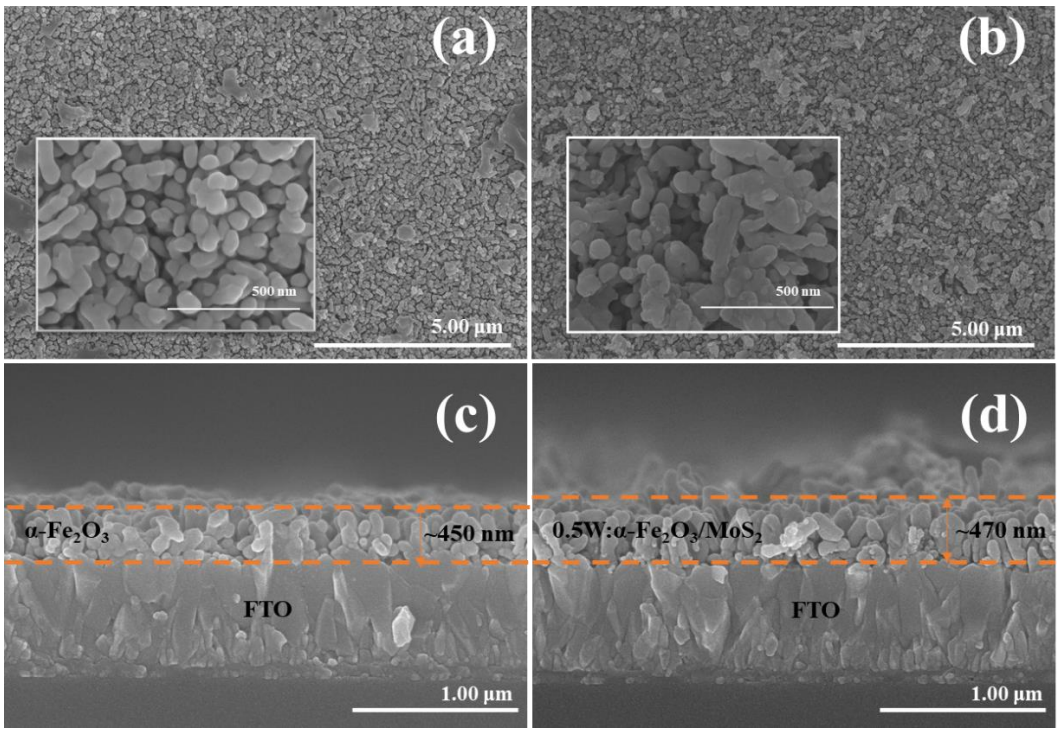

Fig. 4.1.2. Top-view (a and b) and cross-sectional (c and d) FE-SEM images of pure α-Fe_2O_3 (a and c) and 0.5W:α-Fe_2O_3/MoS_2 (b and d) photoanodes.

After the W doping and junction with MoS_2, the changes in morphology between 0.5W:α-Fe_2O_3 and the 0.5W:α-Fe_2O_3/MoS_2 thin films could not be clearly distinguished in SEM images (Fig.

4.1.2). To further investigate the morphology of the 0.5W:α-Fe_2O_3/MoS_2 sample, high-resolution TEM (HRTEM), high-angle annular dark-field scanning TEM (HAADF-STEM) and energy-dispersive X-ray spectroscopy (EDX) elemental mapping images are shown in Fig. 4.1.3(a–i). The morphology of the 0.5W:α-Fe_2O_3/MoS_2 has nanorods (Fig. 4.1.3a), however shortened nanorods which may have originated during the processing of preparation and TEM scanning. According to the Figs. 4.1.3c, the nanorod morphology remained almost unchanged upon W doping, [13]. A uniform α-Fe_2O_3 film was just detected with a lattice spacing of 0.249 nm corresponding to (110), which was also confirmed through XRD analysis (Fig. 4.1.4a). The α-Fe_2O_3/MoS_2 structure was shown to have a core-shell morphology with a thickness of around 6 nm (Fig. 4.1.3c). When the MoS_2 nanosheets coated on the surface of W:α-Fe_2O_3, the crystal structure decreased as compared to that of pure MoS_2 nanosheets. This change in the crystal structure of the MoS_2 layer can be attributed to increasing the concentration of the MoS_2 nanosheets on the surface of the α-Fe_2O_3 photoanode by dropping several times. In Figs. 4.1.3b and c, the MoS_2 surrounding the 0.5W:α-Fe_2O_3 indicated that the MoS_2 layer was composed of stacked nano sheets [14]. Further, the STEM and EDX elemental mapping results of the 0.5W:α-Fe_2O_3/MoS_2 nanorods show the presence of all elements which confirms the XPS analysis results.

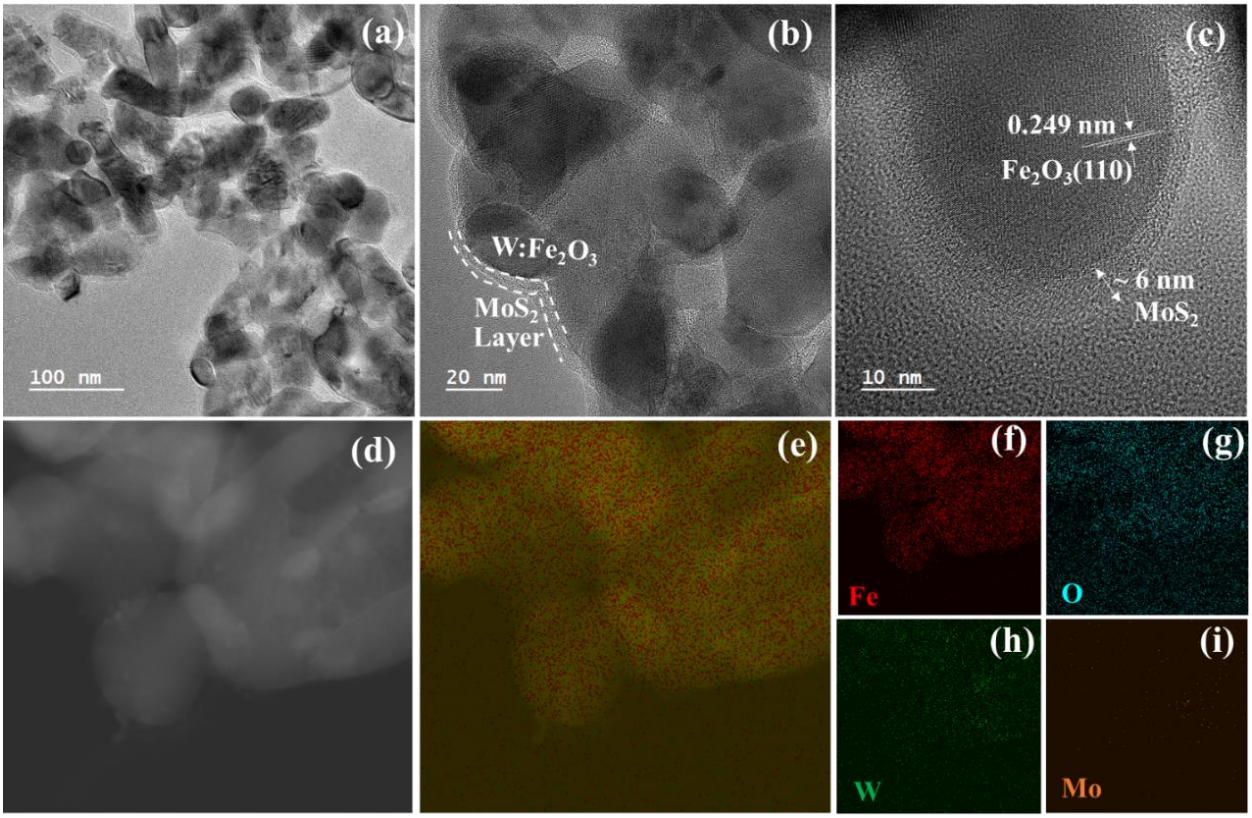

Fig. 4.1.3. (a-c) HRTEM images of 0.5W:α-Fe_2O_3/MoS_2 (d-i) HAADF-STEM image and energy-dispersive EDX elemental mapping images of 0.5W:α-Fe_2O_3/MoS_2 sample.

The phase purities and crystallographic structures of the prepared pure α-Fe_2O_3, 0.5W:α-Fe_2O_3 and 0.5W:α-Fe_2O_3/MoS_2 thin films were confirmed by using X-ray diffraction (XRD) patterns (see Fig. 4.1.4a). The diffractions at 64, 62, 37, and 34° respectively matched with the (300), (214), (110), and (104) planes of the α-Fe_2O_3 structure (PDF 02-0915) in all the samples and no additional XRD peak could be observed. Thus, the XRD data reveals that the pure crystal structure of α-Fe_2O_3 reserved without appearance of any extra peaks or impurity such as WO_3 or MoO_3. This possibly indicated that after addition of $N_{10}H_{42}W_{12}O_{42}$ and calcination at 550 ^oC, W elements diffused into a shallow distance in the crystalline structure of α-Fe_2O_3 and replaced on defect sites resulted in W-doping α-Fe_2O_3 [2] .

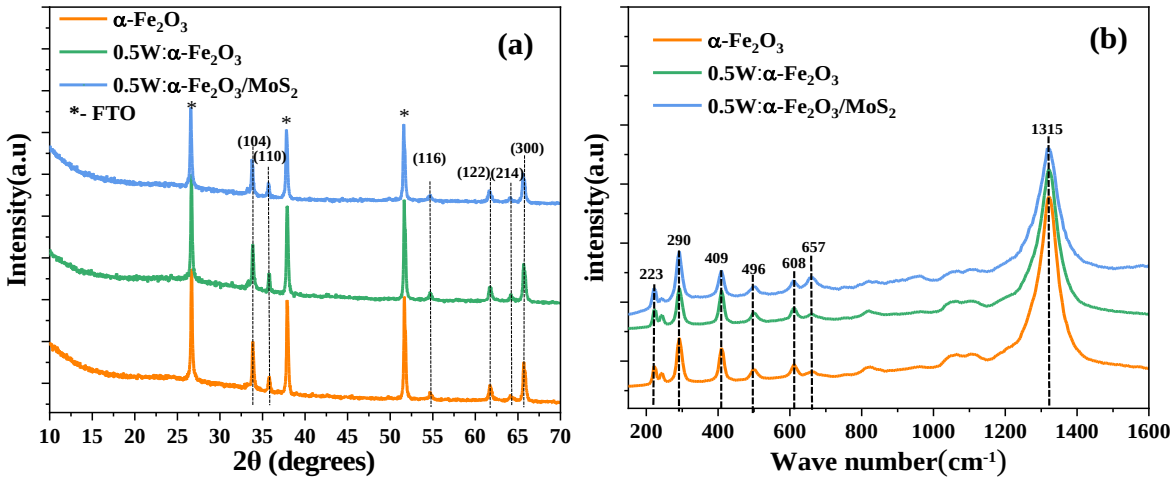

Fig. 4.1.4. (a) X-Ray Diffraction patterns and (b) Raman spectra of the pure α-Fe_2O_3, 0.5W:α-Fe_2O_3, and 0.5W:α-Fe_2O_3/MoS_2.

Fig. 4.1.4b shows the Raman spectra of pure α-Fe_2O_3, 0.5W:α-Fe_2O_3 and, 0.5W:α-Fe_2O_3/MoS_2 nanorods to further clarify the structural features. All the characteristic peaks of the α-Fe_2O_3-based samples show well crystallized features of the hematite. The spectral range between 200 and 650 cm^{-1} contains the most intensive peaks of α-Fe_2O_3, while the peak recorded at 1315cm^{-1} with a higher intensity is determined to be a second harmonic vibration. The vibration peak intensity becomes wider and smaller after structural defects due to W doping in 0.5W:α-Fe_2O_3 and heterojunction 0.5W:α-Fe_2O_3/MoS_2.The increasing intensity of the peak around 657 cm^{-1} can be attributed to the induction of an impurity phase and a defective structure [15].

To detect the presence of elements in the samples and investigate the electronic structure, XPS analysis were performed, and the results are shown in Fig. 4.1.5a–d. The Fe 2p region spectra show binding energies of 724.5 eV (Fe $2p_{1/2}$) with a shake-up satellite line at 733.5 eV and other binding energies of 711.1 eV (Fe $2p_{3/2}$) with a shake-up satellite line at 718.8 eV, which is specified to be Fe^{3+} in α-Fe_2O_3 (see Fig. 5a). As shown Fig. 4.1.5b, the deconvolution O1s spectrum peaks had a high peak at around 530.8 eV that can be corresponds to the Fe-O and Mo-O bonds at around 529.7 eV and 530.2 eV, respectively. The peak at 530.2 eV could be related to the oxygen atoms of the

MoO_3 on the surface [16]. The O1s spectrum at around 531.5 eV revealed OH^- in both α-Fe_2O_3 and 0.5W:α-Fe_2O_3 as well as Mo-peroxo for 0.5W:α-Fe_2O_3/MoS_2. The hydroxyl groups (-OH) were unified on the surface by water molecular adsorption, while the peroxo groups (O_2^{2-}) joined to the Mo atoms attributing to the surface defect [17]. In the detecting W spectra, three peaks were observed at 35.1, 37, and 41.2 eV for W $4f_{7/2}$, W $4f_{5/2}$, and W $5p_{5/2}$, respectively, which can be attributed to the existence of W nanoparticle in the 0.5W:α-Fe_2O_3 sample (Fig. 4.1.5c). Interestingly, the W peaks in the 0.5W:α-Fe_2O_3/MoS_2 thin film are shifted to the lower binding energies of 34.1, 36.2, and 40.3 eV for W $4f_{7/2}$, W $4f_{5/2}$, and W $5p_{5/2}$, respectively. This negative shift in binding energy can be detected by the electron donation of W, leading to a change in the electronic properties of the W 4f peaks [18].

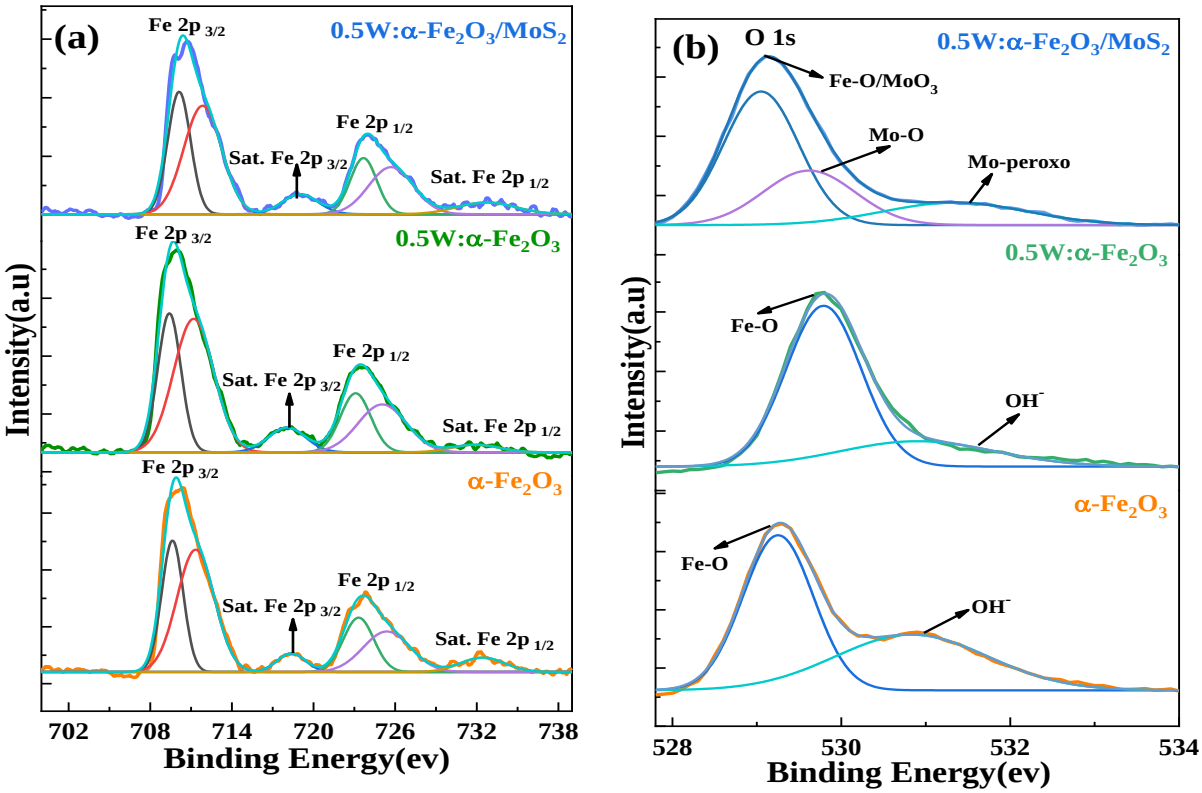

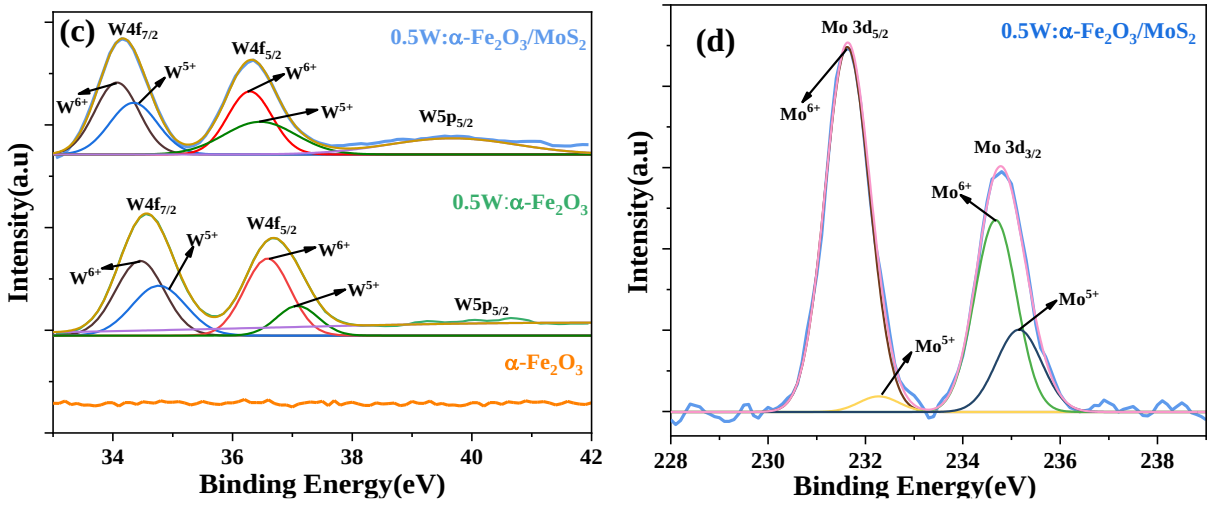

Fig. 4.1.5. XPS spectra for (a) Fe 2p (b) O1s, (c) W4f and (d) Mo3d for pure α-Fe_2O_3, 0.5W:α-Fe_2O_3, and 0.5W:α-Fe_2O_3/MoS_2.

Furthermore, Mo^{6+} and Mo^{5+} peaks appear in 0.5W:α-Fe_2O_3/MoS_2 and are confirmed by deconvoluted two major peaks at 231.5 eV ($Mo3d_{5/2}$) and 234.9 eV ($Mo3d_{3/2}$), respectively, which are attributed to the natural metal ion and oxygen vacancy on surface defects (Fig. 4.1.5d) . The XPS analysis for the sulfur element did not show any peaks, which might be related to the high annealing temperature. This analysis can support the conversion of MoS_2 into MoO_3 in the calcination process [16].

To evaluate the optical properties of the prepared photoelectrodes, the UV-vis absorption spectra were measured for the pure α-Fe_2O_3, 0.5W:α-Fe_2O_3, and 0.5W:α-Fe_2O_3/MoS_2 photoanodes (Fig. 4.1.6a). The absorbances of 0.5W:α-Fe_2O_3 and 0.5W:α-Fe_2O_3/MoS_2 are significantly enhanced compared to that of the pure α-Fe_2O_3. Further, the slight redshift indicates the presence of W as a dopant and MoS_2 nanosheets as a heterojunction, which implies that the absorbance intensity was improved [19]. The heterojunction with MoS_2 also leads to higher absorption which in turn enhances its photoelectric performance by improving the light absorption ability and the photon to charge conversion efficiency [20].

As shown in Fig. 4.1.6b, the light-harvesting efficiency (LHE) values of the α-Fe_2O_3, 0.5W:α-Fe_2O_3, and 0.5W:α-Fe_2O_3/MoS_2 thin films show enhanced light absorption, which is effective for catching more photons and generating more charge carrier; the LHE is obtained using the Eq. (3):

$$LEH=1-\mathbf{10}^{-A(\lambda)} \quad (3)$$

Where A(λ) is the absorbance in different wavelengths. The higher absorbance of photoelectrode led to the higher LHE values. The LHE enhancement can be attributed to the fact that the combination of the W doped and MoS_2 nanosheets heterojunction with α-Fe_2O_3 has a notable supplementary effect on the optical properties and this structure plays an important role in light capture efficiency [21].

The photogenerated electron-hole recombination rate and charge trapping effect can be detected by analyzing the photoluminescence (PL) spectrum data (Fig. 4.1.6a). The PL spectra of the undoped, W doped, and heterojunction structured 0.5W:α-Fe_2O_3/MoS_2 thin films were measured under an excitation range from 450 nm to 600 nm with a 10nm interval. Furthermore, the PL intensity of 0.5W:α-Fe_2O_3/MoS_2 thin film is shown in Fig. 4.1.6c, which implied reductions in recombination and charge trapping of photogenerated electron-hole pairs. The heterojunction the 0.5W:α-Fe_2O_3 with MoS_2 had decreased PL intensity compared to pure and 0.5W:α-Fe_2O_3. In addition, the broadening and widening of the PL could be due to partially absorption and trapping of emitted excited electrons induced by MoS_2 layer [22]. Thus, the W doping and the construction of the Z-scheme structure in the heterojunction greatly contributed to the improved optical property by increasing more light harvesting and the photocurrent density leading to improved PEC performance (see section 4.1.3.2) [23].

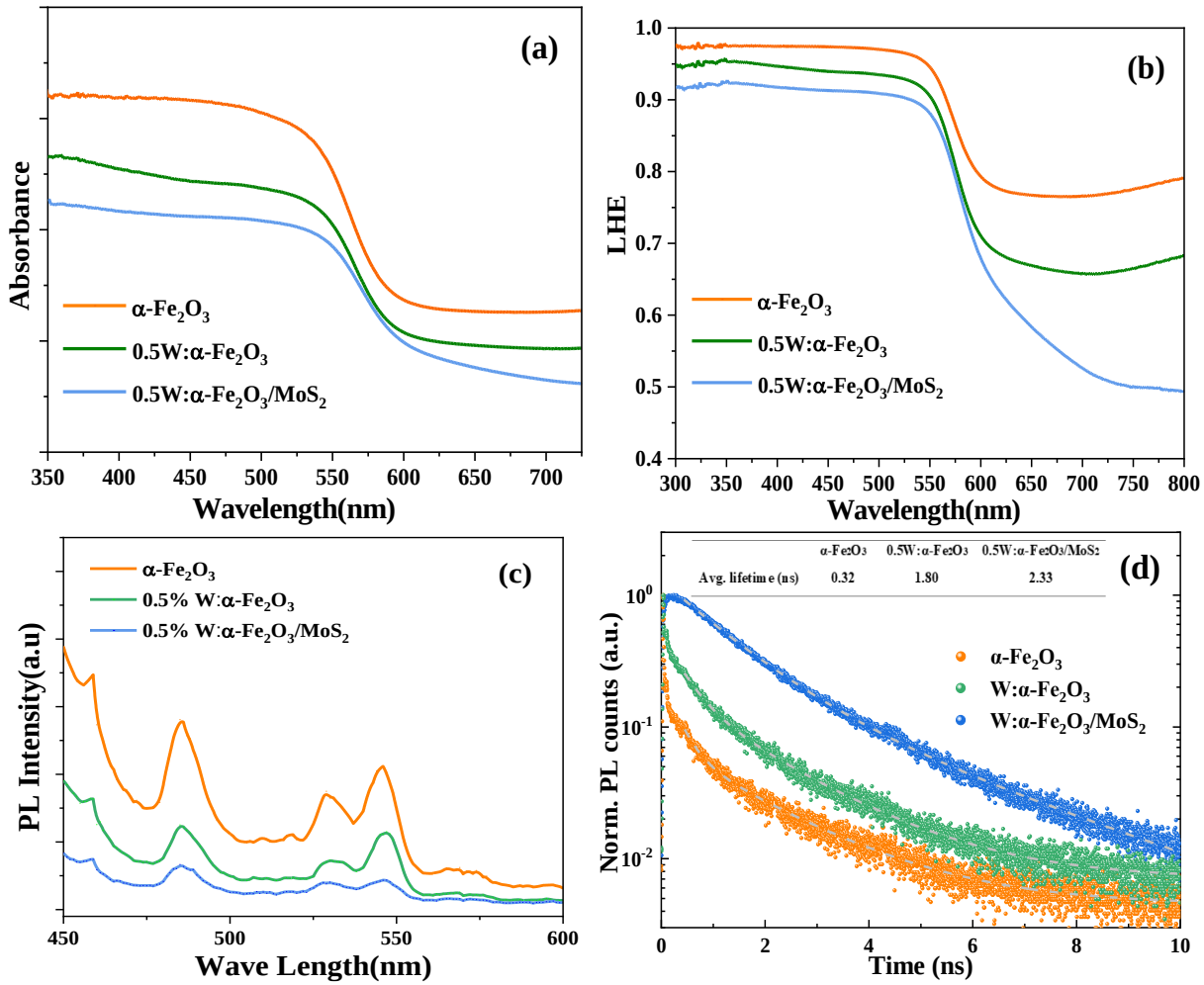

Fig. 4.1.6. (a) UV-vis absorbance, (b) LHE, (c) PL, and (d) TRPL of pure α-Fe_2O_3, 0.5W:α-Fe_2O_3 , and 0.5W:α-Fe_2O_3/MoS_2.

The time-resolved photoluminescence (TRPL) curves shown in Fig. 4.1.6d are used to assess the recombination kinetics of photoinduced electron-hole pairs. The TRPL decay spectrum was fitted with a biexponential decay function. The TRPL spectra in Fig. 4.1.6d reveal that the average decay time of the charge carriers of W:α-Fe_2O_3 (τ_{ave} =1.80 ns) is longer than that of pure α-Fe_2O_3 (τ_{ave} =0.32 ns), this significant increase in estimated τ_{ave} suggested that using W dopant could more efficiently accelerate light-induced charge separation and transfer. Further, the τ_{ave} of the 0.5W:α-Fe_2O_3/MoS_2 photoanode reaches 2.33 ns by making a heterojunction, which implies that efficient charge transfer occurs between α-Fe_2O_3 and MoS_2 semiconductors. The better separation of

electron-hole pairs leads enhanced migration of charger carriers in the 0.5W:α-Fe_2O_3/MoS_2 electrode, leading to a higher PEC water oxidation efficiency [24].

4.1.3.2. Photoelectrochemical (PEC) Performance

Linear scan voltammetry (LSV) was conducted for pure α-Fe_2O_3, W: α-Fe_2O_3, and heterojunction with MoS_2 (Figs. 4.1.7a and b) under continuing and periodic on-off 100 $mWcm^{-2}$ illuminations between 0.3 and 1.5 V vs. RHE in 1 M NaOH as an electrolyte. The photocurrent density is zero in the dark condition for all samples, and all electrodes showed a prompt and reproducible photocurrent response with respect to the irradiation signal ON-OFF cycles. The optimized W doped α-Fe_2O_3 electrode (0.5W:α-Fe_2O_3) showed increased photocurrent density to ~0.5 $mA.cm^{-2}$ at 1.23 V vs. RHE. The photocurrent onset potential was slightly shifted to negative areas after applying various atomic percentages of W doped on the surface of α-Fe_2O_3 photoelectrodes. The cathodic shift was attributed to the decreased the back reaction, but not the accelerating water oxidation kinetics, ions adsorption or passivating surface states [25, 26]. After constructing the heterojunction of the optimized W doping into α-Fe_2O_3 with MoS_2, the identified photocurrent density was 1.83 $mA.cm^{-2}$ at 1.23 V vs. RHE, which is 26 and 3.66 times higher than those of the α-Fe_2O_3 and α-Fe_2O_3/MoS_2 electrodes, respectively. The cathodic shift in the onset potential is more pronounced in the 0.5W:α-Fe_2O_3/MoS_2 electrode which implies a shift of the conduction band in the negative region and facile charge transfer path ways [27].

The photocurrent response and stability vs. time (i-t) curves of pure α-Fe_2O_3, 0.5W:α-Fe_2O_3, , and 0.5W:α-Fe_2O_3/MoS_2 were evaluated by chronoamperometry at a constant applied potential of 1.23V vs RHE for 4 on-off cycles under 1-sun illumination (Fig. 4.1.7c). The photocurrents in these four cycles were measured under periodic illumination (30 s light on and 15 s light off) in

NaOH 1M solution as an electrolyte. The immediate response to the light on-off terms for all electrodes implies appropriate sample fabrication for the charge mobility improvement [28]. After the construction of the heterojunction 0.5W:α-Fe_2O_3 electrode with MoS_2, the 0.5W:α-Fe_2O_3/MoS_2 photoelectrode could also be fitted well on its photocurrent response under the four light on/off, and it also had good stable behavior in continuous 30 min illumination. These desirable results are attributed to the suitable junction between these two semiconductors with good band alignment which lead to facile the charge transfer (Fig. 4.1.7c-d).

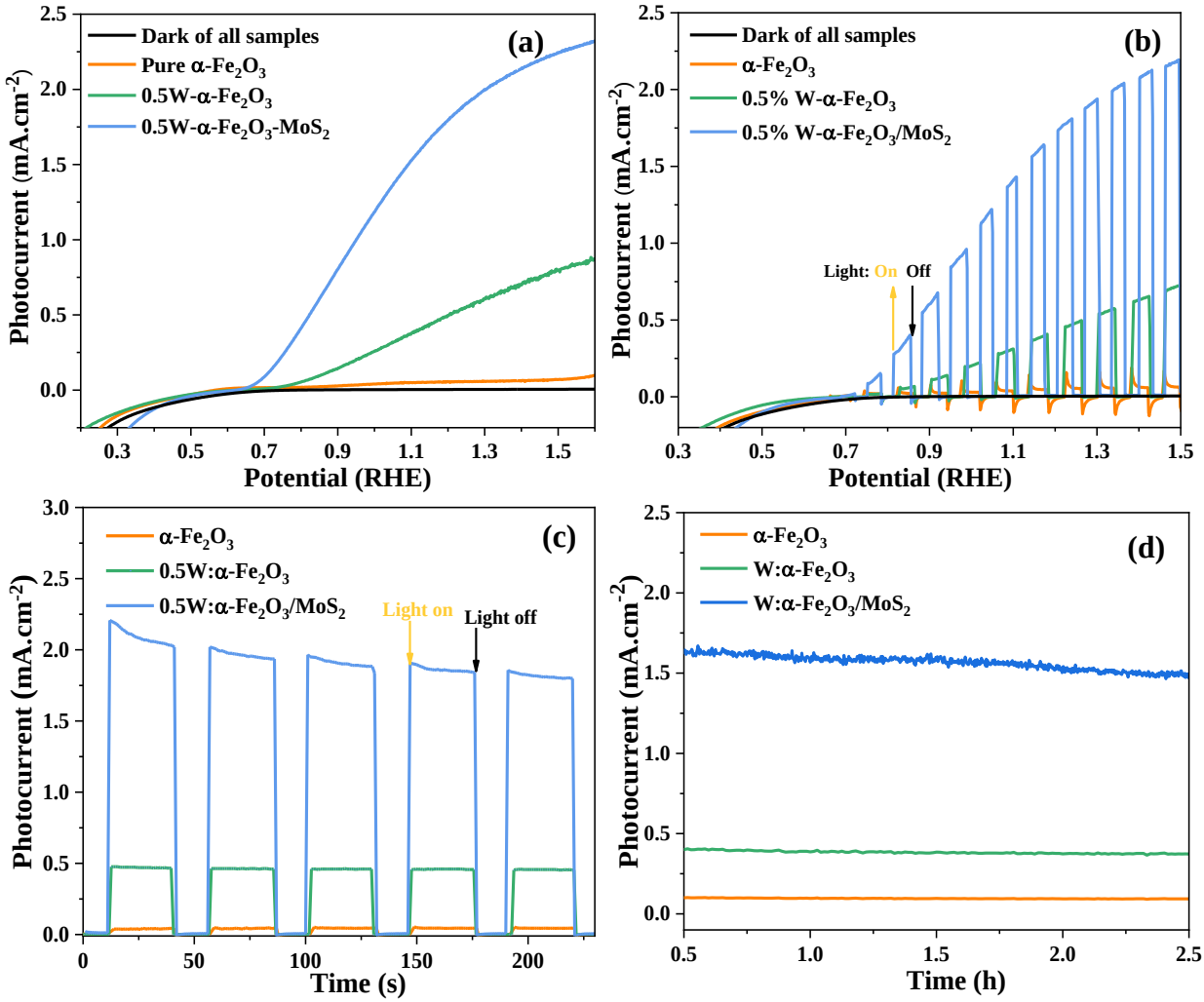

Fig. 4.1.7. (a) Linear scan voltammetry and (b) chopped LSV vs. potential linear from 0.3 to 1.5 V (vs. RHE), (c) photocurrent response, and (d) photocurrent stability at 1.23 V (vs. RHE) for pure α-Fe_2O_3, 0.5W:α-Fe_2O_3, and 0.5W:α-Fe_2O_3/MoS_2 under 100 $mWcm^{-2}$ illumination. The electrolyte was a 1 M NaOH.

Fig. 4.1.8 shows the Nyquist plots of the α-Fe_2O_3, 0.5W:α-Fe_2O_3, and 0.5W:α-Fe_2O_3/MoS_2 photoanodes at different potentials (0.9, 1, and 1.2 V vs. RHE) which were obtained through potentiostatic electrochemical impedance spectroscopy (EIS). The efficiency of photogenerated electron-hole separation and the resistance of electron transfer for photoelectrodes are reflected in the size of the arc radius in the Nyquist plot. The parameter values in the inside tables represent the data fitted with the demonstrated equivalent circuit model [29] (inside Fig. 4.1.8d). The Randles circuit model was well fitted to all the samples with the sheet resistance (R_s), interfacial charge transfer resistance (R), and the space charge capacitance of the electrode/electrolyte interface (C). The tables inside of the graphs demonstrate the resistances and space charge capacitance values, which show that the lowest resistance and highest capacitance values were obtained by 0.5W:α-Fe_2O_3/MoS_2 photoelectrode at a potential of 1.2 V vs. RHE. As indicated in the tables inside of Figs. 8a-c, the charge transfer resistance decreased with the increase in overpotential due to the increased electron transfer rate [30]. This behavior could be attributable to the collaborative approach using MoS_2 as a heterojunction and W as metal doping that facilitates the extraction of holes. Therefore, the 0.5W:α-Fe_2O_3/MoS_2 photoanode reduced recombination rate of charge carriers at the hematite nanorods which is entirely consistent with the TRPL data .

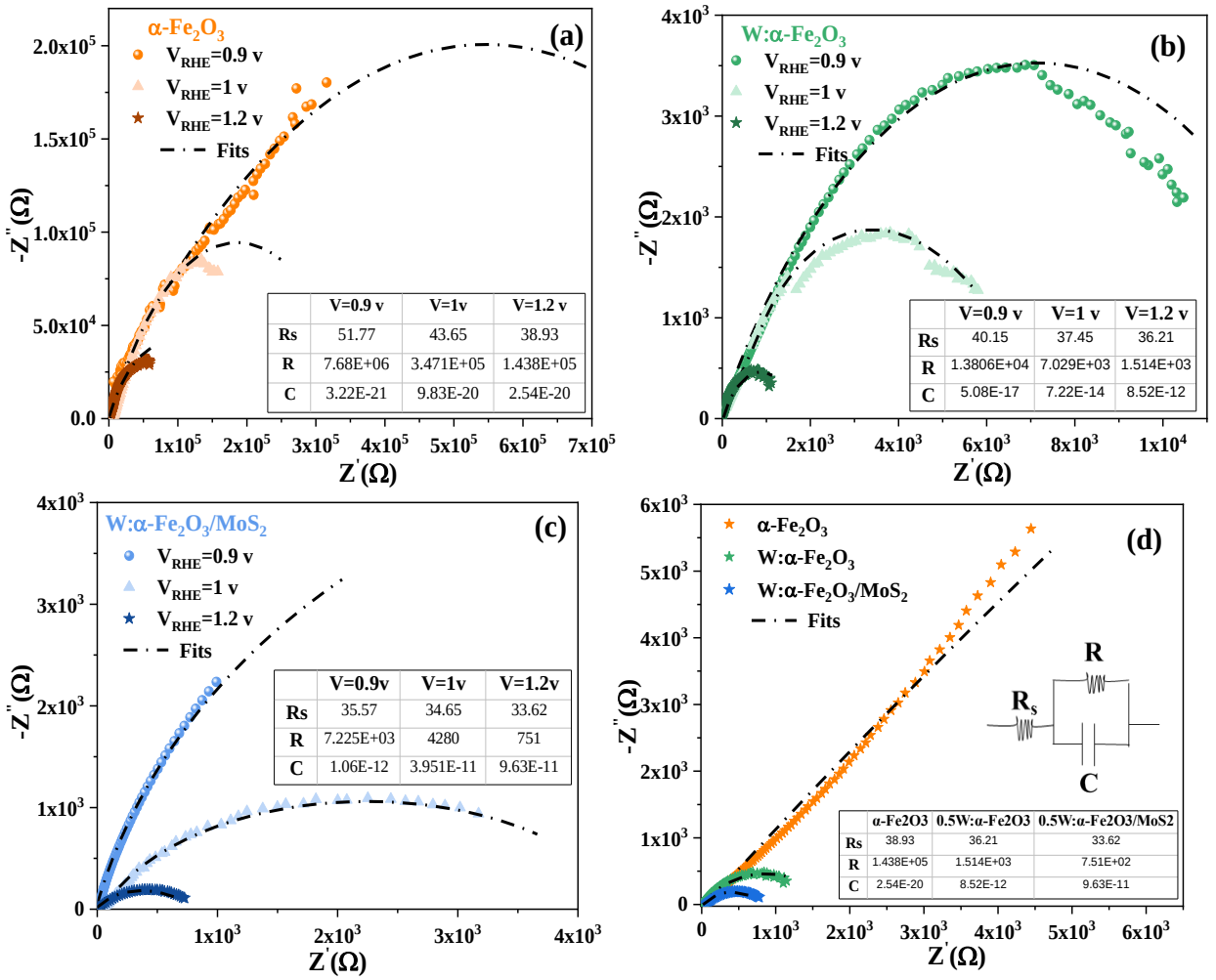

Fig. 4.1.8. Nyquist plot in potential 0.9, 1, 1.2 V vs. RHE for (a) pure α-Fe_2O_3, (b) 0.5W:α-Fe_2O_3, and (c) 0.5W:α-Fe_2O_3/MoS_2 electrodes. (d) Nyquist plot in potential 1.2 V vs. RHE for α-Fe_2O_3, 0.5W:α-Fe_2O_3, and 0.5W:α-Fe_2O_3/MoS_2 electrodes. The supporting electrolyte was a 1 M aqueous solution of NaOH. The unit of the series resistance (R_s) and charge transfer resistance (R) are ohm (Ω) and unit of capacitance (C) is farad (F).

As shown in Fig. 4.1.9a, the Mott-Schottky plots were measured to estimate the flat band potential (V_{fb}), donor concentration (N_D), and width of the space charge layer (W_{SCL}), which can be obtained using equations 4 and 5:

$$\frac{1}{C^2} = \frac{2}{\varepsilon\varepsilon_0 A^2 e N_D}\left(V - V_{fb} - \frac{K_B T}{e}\right) \quad (4)$$

$$W_{SCL} = \sqrt{\frac{2\varepsilon\varepsilon_0 (V - V_{fb})}{e N_D}} \quad (5)$$

where V is the conduction band potential (V), V_{fb} the flat band potential (V), k the Boltzmann

constant, T the temperature (K), e the charge of an electron (C), ε the relative permittivity, ε_0 the dielectric constant, N_D the donor concentration per unit volume (cm^3), and C_{sc} the surface charge capacitance (F/cm^2). The linear slopes in the Mott–Schottky plot for the pure α-Fe_2O_3 electrode decreased after doping W on the surfaces of the α-Fe_2O_3 thin films. The 0.5W:α-Fe_2O_3 sample showed an optimized linear slope with a W_{SCL} value around 38% lower than that of pure α-Fe_2O_3. The N_D and V_{fb} values estimated from the slopes and intercepts of the Mott-Schottky plots for the pure α-Fe_2O_3, 0.5W:α-Fe_2O_3, and 0.5W:α-Fe_2O_3/MoS_2 samples. In addition, the donor density was increased (N_D=5.97E+20 cm^{-3}) and the flat band potential (V_{fb}=0.81 v) was decreased by fabrication of heterojunction with the MoS_2 nanosheets as the second modification process. The space charge layer value (W_{SCL}=3.08 nm) is around 51 and 9% lower than those of pure α-Fe_2O_3 and 0.5W:α-Fe_2O_3, respectively. The W doping and heterojunction with MoS_2 nanosheets led to lower overpotential for the oxygen evolution reaction to improve the PEC performance by generating more electron-hole pairs and enhancing the charge transfer efficiency [31].

The photoelectrochemical performance for all the samples under visible light region irradiation were confirmed by the incident-photon-to-current-efficiencies (IPCE) measurement using Eq.6:

$$IPCE, \% = \left(\frac{1240}{\lambda} \times \frac{J_{light}}{P_{light}}\right) \times 100 \quad (6)$$

The highest IPCE values better support the heterojunction effect with the MoS_2 nanosheets. The identified IPCE for 0.5W:α-Fe_2O_3/MoS_2 photoanode was 38.7% at 325 nm, which is 2.5 times higher as compared that of 0.5W:α-Fe_2O_3 (Fig. 4.1.9b). Further, the IPCE curves correspond to the results of the optical absorption analysis spectrum for all samples under the visible light [32].

The applied bias photon to current efficiencies (ABPE) of α-Fe_2O_3, 0.5W:α-Fe_2O_3, and 0.5W:α-Fe_2O_3/MoS_2 are plotted in Fig. 4.1.9c by Eq. 7:

$$\text{ABPE (\%)} = \left(\frac{J\left(\frac{mA}{cm2}\right)\times(1.23-Vbias)(V)}{P\left(\frac{mW}{cm2}\right)}\right) \quad (7)$$

Here, J is the photocurrent density at the measured potential V vs. RHE under 100 mW.cm^{-2} light illumination in the NaOH 1M (pH=12) electrolyte. The maximum ABPE of 0.5W:α-Fe_2O_3 and 0.5W:α-Fe_2O_3/MoS_2 electrodes were obtained at 1.02 and 0.96 V vs RHE, respectively. The percentages of ABPE for α-Fe_2O_3, 0.5W:α-Fe_2O_3 and 0.5W:α-Fe_2O_3/MoS_2 were 0.9, 5, and 26%, respectively. Moreover, the potential at the highest ABPE value of 0.5W:α-Fe_2O_3/MoS_2 electrode shifted to the cathodic direction compared to that of pure α-Fe_2O_3. This study found that the charge transport of α-Fe_2O_3 in the low potential range is not achieved by W doping, but is easily obtained by fabricating a heterojunction with MoS_2 nanosheets [33].

The enhancement in electron-hole generation and charge transport by applying W doped and MoS_2 heterojunction were more investigated further with the open circuit potential (ΔOCP) decay curve. As shown in Fig. 4.1.9d, when the light was turned on, the potential was decreased to obtain a stable value. The 0.5W:α-Fe_2O_3 photoanode showed more photogenerated electron-hole production and a lower recombination rate as compared with that of pure α-Fe_2O_3, which are consistent with the lower stable potential between the 30, and 60 s period (Fig. 4.1.9d) [34]. The ΔOCP value of the 0.5W:α-Fe_2O_3/MoS_2 photoanode was significantly decreased to a lower potential value (~ -0.25), and this was attributed to facilitation of the charge transfer path way and the decreased the recombination rate [35].

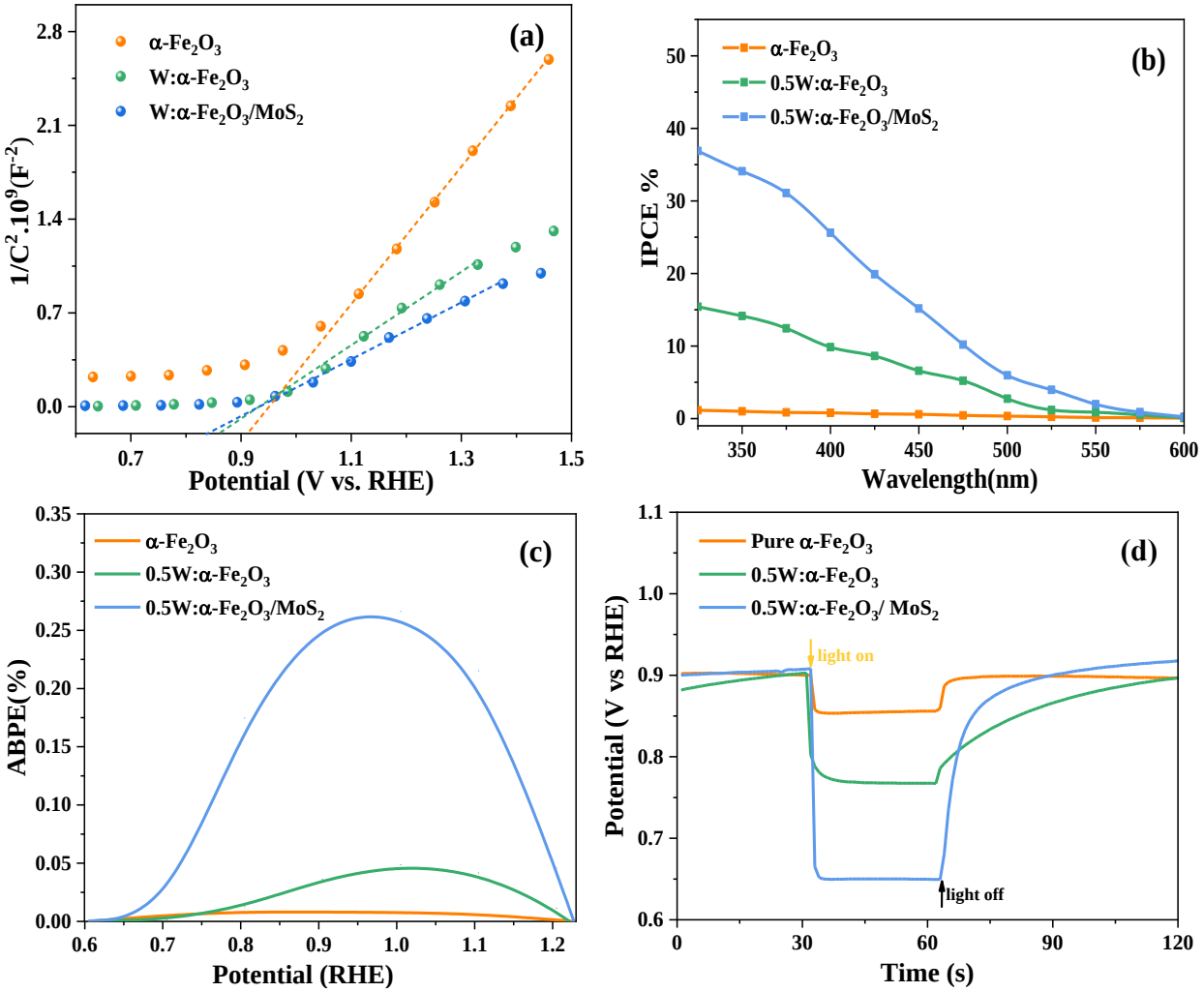

Fig. 4.1.9. (a) Mott–Schottky plot, (b) IPCE, (c) ABPE plots, and (d) open circuit potential (ΔOCP) for α-Fe_2O_3, 0.5W:α-Fe_2O_3, and 0.5W:α-Fe_2O_3/MoS_2 electrodes.

The photocurrent commonly occurs through the light absorption of the semiconductor, separation of the photogenerated charge carriers, and surface charge injection for PEC performance. The charge separation efficiency (η_{sep}) and the surface charge injection efficiency (η_{inj}) of the pure α-Fe_2O_3, 0.5W:α-Fe_2O_3, and 0.5W:α-Fe_2O_3/MoS_2 electrodes are shown in Figs. 4.1.10a and b, respectively. The values of η_{sep}, η_{inj}, and η_{LHE} are calculated in 1M NaOH and H_2O_2 as a electrolyte [36]. The charge separation efficiency (η_{sep}) was enhanced from ca. 0.07 to 0.29, and to 0.42 at 1.23 V vs. RHE for the α-Fe_2O_3, 0.5W:α-Fe_2O_3, and 0.5W:α-Fe_2O_3/MoS_2 electrodes, respectively. The surface charge injection efficiency (η_{inj}) of the α-Fe_2O_3 increased from ca. 0.08 to ca. 0.37,

and to 0.86 at 1.23 V vs. RHE for 0.5W:α-Fe_2O_3 and 0.5W:α-Fe_2O_3/MoS_2 electrodes, respectively. Obviously, the charge separation and surface charge injection efficiency were enhanced after a collaborative approach using MoS_2 as a heterojunction and W as metal doping on the α-Fe_2O_3 nanorods which in turn overcame the reaction barrier to impressively improve the hole transport through the electrode/electrolyte interface [37].

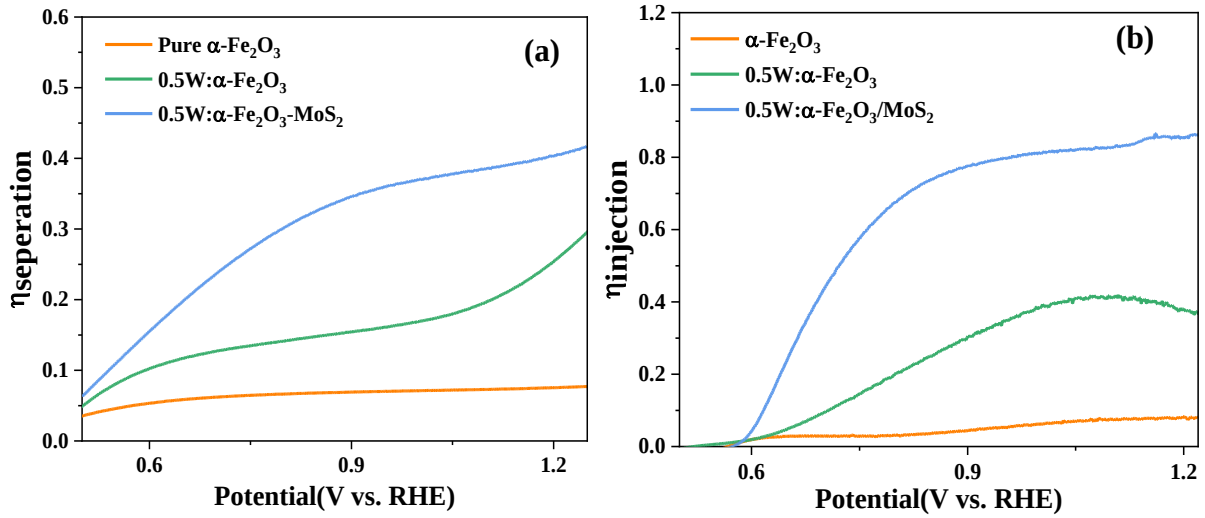

Fig. 4.1.10. (a) Charge separation efficiency (η_{sep}) and (b) charge injection efficiency (η_{inj}) of the pure α-Fe_2O_3, 0.5W:α-Fe_2O_3, and 0.5W:α-Fe_2O_3/MoS_2 electrodes.

For comparison, the overall water splitting of α-Fe_2O_3, 0.5W-α Fe_2O_3 and 0.5W-α Fe_2O_3/MoS_2 photoanodes were evaluated by measuring the H_2 and O_2 evolution at 1.23 V versus RHE under 100 mW.cm^{-2} irradiation in 1 M NaOH electrolyte. As demonstrated in Figs. 4.1.11a and b, the total H_2 values generated after 2h of irradiation for α-Fe_2O_3, 0.5W-α Fe_2O_3 and 0.5W-α Fe_2O_3/MoS_2 are 2, 11.9 and 49 μmol.cm^{-2}, respectively, and the total O_2 generated are 0.93, 5.9 and 23.8 μmol.cm^{-2}, respectively, indicating at 2:1 ratio of the water splitting reaction. The H_2/O_2 gas evolution process was accompanied by a stable photocurrent density as shown by chronoamperometry in Fig. 4.1.7d. Further, the Faradaic efficiency of O_2 and H_2 evolution for 0.5W-α Fe_2O_3/MoS_2 photoanode is determined to be 85−88%, indicating most of the

photogenerated holes were used for the water oxidation reaction[34].

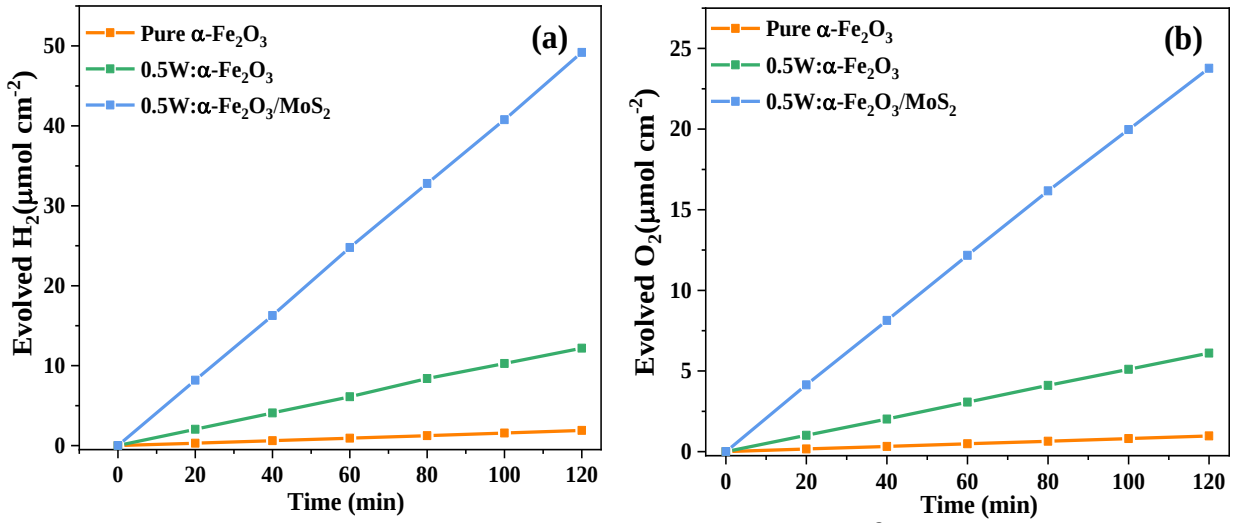

Fig. 4.1.11. (a) H_2 and (b) O_2 evolution vs. reaction time per illuminated area ($1cm^2$) for α-Fe_2O_3, 0.5W:α Fe_2O_3 and 0.5W:α Fe_2O_3/MoS_2 photoanodes at a potential of 1.23 V versus RHE. Under 100 $mW.cm^{-2}$ irradiations, electrolyte was a 1M (PH=12) aqueous solution of NaOH.

The electron-hole transfer mechanisms of the α-Fe_2O_3, W:α-Fe_2O_3 and W:α-Fe_2O_3/MoS_2 electrodes are exhibited in Fig 4.1.12. When, W:α-Fe_2O_3 and MoS_2 were in contact, band bending occurred to obtain equilibrium of the Fermi level, which created the heterojunction. After irradiation light electrons were excited from the valence band (VB) to the conduction bands (CB) of W:α-Fe_2O_3 and MoS_2 (Fig. 4.1.12c). Further, the electron from the CB of MoS_2 was then transferred to the CB of W:α-Fe_2O_3 due to the energy level difference as shown in Fig. 4.1.12c. The holes from the VB of W:α-Fe_2O_3 were transferred to the VB of MoS_2 driven by the electrostatic forces and reacted with OH to create O_2 gas, whereas electrons that had arrived at the Pt counter electrode through FTO glass generated H_2 gas. In addition, the space charge region became smaller in W:α-Fe_2O_3/MoS_2 compared to W:α-Fe_2O_3 and α-Fe_2O_3. Due to smaller space charge layer in W:α-Fe_2O_3/MoS_2, holes could move faster to the surface of the photoanode and participate in the oxygen evolution reaction. For further detail, the ultraviolet photoelectron spectroscopy (UPS) results of the α-Fe_2O_3, 0.5W:α-Fe_2O_3, and MoS_2 samples are shown in Fig.

4.1.12. The maximum valence bands were determined to be 6.54, 6.49, and 5.27 eV versus vacuum level for α-Fe_2O_3, 0.5W:α-Fe_2O_3, and MoS_2, respectively. These were calculated using Eq. 12, that involves subtracting the width of the UPS spectrum from the excitation energy (21.22 eV) [38].

Energies of the Fermi levels (E_F) and the valence band maxima (E_{VBM}) retrieved from ultraviolet photoelectron spectroscopy (UPS) spectra show in Fig. 4.1.12a andb. The work function (Φ) gives the energy of the Fermi level with respect to the vacuum level and is calculated with Eq. (8):

$$\Phi = h\nu - E_{highcutoff} \quad ,(h\nu \approx 21.22 \text{ ev}) \tag{8}$$

$|E_{VBM}|$ is calculated with Eq. (9):

$$|E_{VBM}| = h\nu - (E_{highcutoff} - E_{lowcutoff}) \tag{9}$$

The work function (Φ) was estimated based on the energy of the Fermi level with respect to the vacuum level for the α-Fe_2O_3, 0.5%W:α-Fe_2O_3 and MoS_2 samples insides of Fig. 4.1.12a and b, respectively. In addition, the band alignment diagram of the MoS_2 shows in Fig. 4.1.12c, which indicates Φ=4.34 eV corresponding to the few layer of the MoS_2 nanosheets [39].

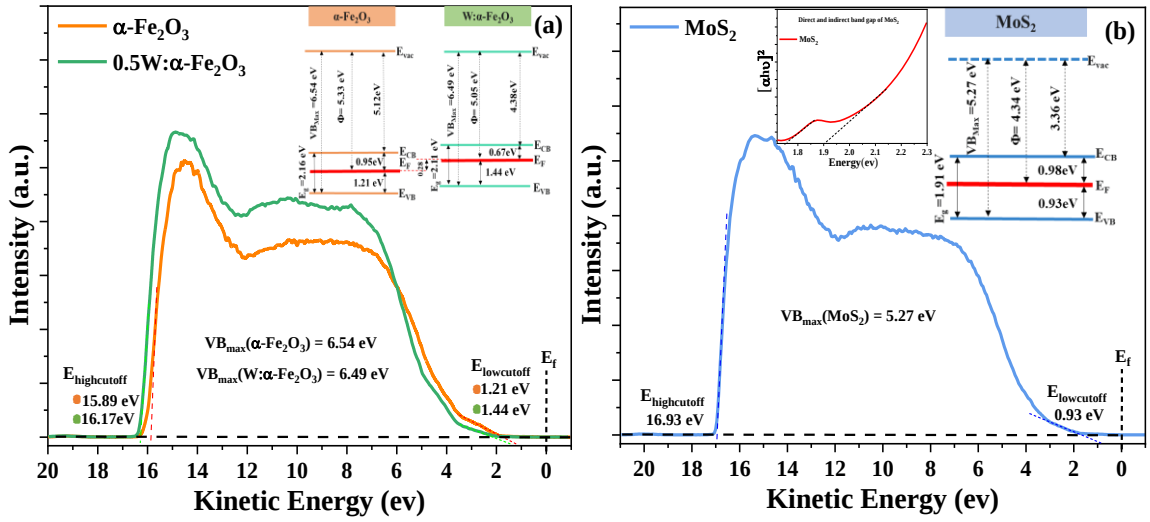

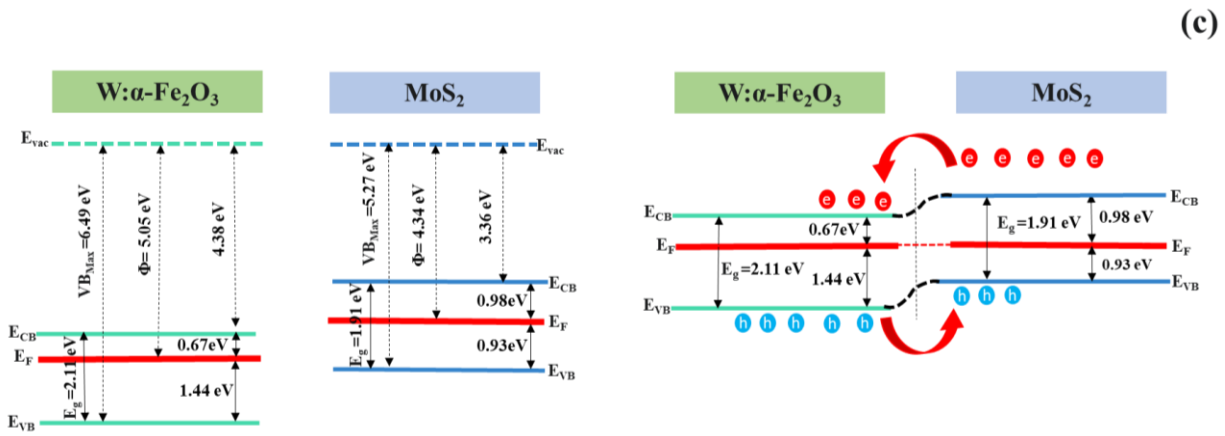

Fig. 4.1.12. UPS and work function of (a) pure hematite and 0.5W doped , (b) MoS2, and (c) energy band diagram of the heterojunction.

The energy band diagram of the heterojunction under the photoexcitation is also shown in Fig. 4.1.13c. This indicates that by depositing α-Fe_2O_3 between MoS_2 and FTO substrate, the charge separation and with depositing W doping α-Fe_2O_3 between MoS_2 and FTO, transfer of electron-hole pairs at semiconductor heterojunction film could be enhanced compared to pure α-Fe_2O_3 electrodes . This led to the more efficient collection of photogenerated electrons on the FTO surface before recombination. Therefore a collaborative approach of MoS_2 as heterojunction and W as doping (0.5W:α-Fe_2O_3/MoS_2 photoanode) create greater strength in the separation and transfer of electron-hole pairs to improve noticeably its PEC performance compared with 0.5W:α-Fe_2O_3 and pure α-Fe_2O_3 electrodes [31].

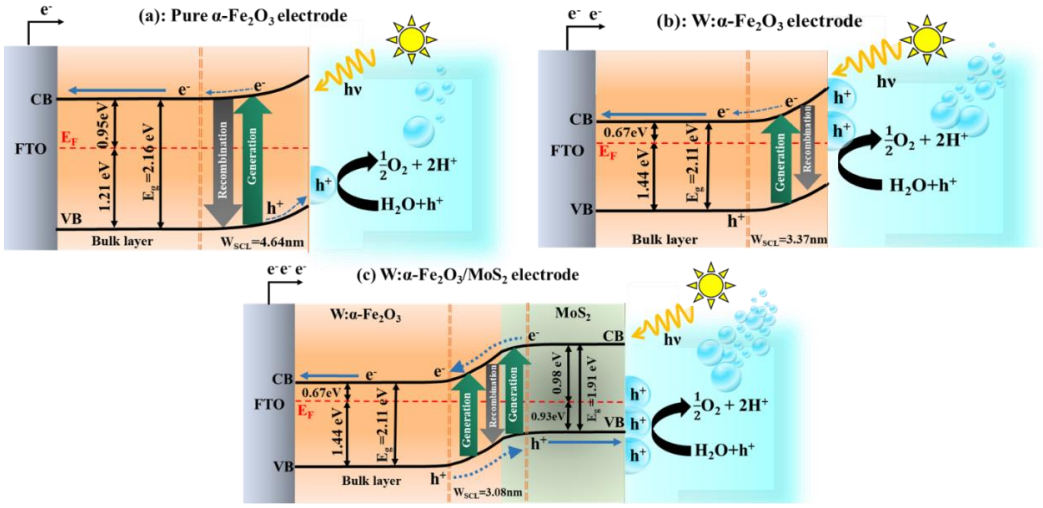

G: Generation electron, W_{SCL}: Space charge layer, and R: Recombination rate

$$G_a < G_b < G_c \qquad W_{SCL\,(a)} > W_{SCL\,(b)} > W_{SCL\,(c)} \qquad R_a > R_b > R_c$$

Fig. 4.1.13. Schematic illustration of electron-hole separation for (a) pure α-Fe_2O_3 electrode (b) W-α-Fe_2O_3 electrode, and (c) 0.5W:α-Fe_2O_3/MoS_2 electrode under 100 mWcm^{-2} in contact with 1 M NaOH electrolyte.

4.1.4. Conclusion

This study successfully fabricated of the heterojunction between two-dimensional materials (MoS_2) and tungsten (W) doped α-Fe_2O_3 by optimizing the atomic percentage of tungsten and amount of the MoS_2 nanosheets by using simple and low-cost synthesis processes to improve the efficiency of photoelectrochemical performance. The identified photocurrent density of the 0.5W:α-Fe_2O_3/MoS_2 photoanode was ~1.83 mA.cm^{-2} at 1.23 V_{RHE}, which was around 4 and 26 times higher than that of α-Fe_2O_3/MoS_2 and pure α-Fe_2O_3 electrodes, respectively. The combination of the heterojunction and metal doping on the pure α-Fe_2O_3 increased its donor concentration, reduced the space charge layer, and decreased the flat band potential, which could all have contributed to the improved photoelectrochemical efficiency. The optimized incorporation of 0.5%W doping and 2D nanosheets of MoS_2 (0.5W:α-Fe_2O_3/MoS_2) showed IPCE of 37% and ABPE 26% at 0.96 V_{RHE}, which are around 5.2 and 13 times higher than those of 0.5W:α-$Fe_2O_3$and pure α-Fe_2O_3, respectively.

Reference:

[1] V. Vinesh, M. Ashokkumar, B. Neppolian, rGO supported self-assembly of 2D nano sheet of (g-C3N4) into rod-like nano structure and its application in sonophotocatalytic degradation of an antibiotic, Ultrasonics Sonochemistry, (2020) 105218.

[2] W. Li, K. Wang, X. Yang, F. Zhan, Y. Wang, M. Liu, X. Qiu, J. Li, J. Zhan, Q. Li, Surfactant-assisted controlled synthesis of a metal-organic framework on Fe2O3 nanorod for boosted photoelectrochemical water oxidation, Chemical Engineering Journal, 379 (2020) 122256.

[3] S. Bai, X. Yang, C. Liu, X. Xiang, R. Luo, J. He, A. Chen, An Integrating Photoanode of WO3/Fe2O3 Heterojunction Decorated with NiFe-LDH to Improve PEC Water Splitting Efficiency, ACS Sustainable Chemistry & Engineering, 6 (2018) 12906-12913.

[4] A. Verma, A. Srivastav, S.A. Khan, V.R. Satsangi, R. Shrivastav, D.K. Avasthi, S. Dass, Enhanced photoelectrochemical response of plasmonic Au embedded BiVO 4/Fe 2 O 3 heterojunction, Physical Chemistry Chemical Physics, 19 (2017) 15039-15049.

[5] C. Shao, A.S. Malik, J. Han, D. Li, M. Dupuis, X. Zong, C.J.N.E. Li, Oxygen vacancy engineering with flame heating approach towards enhanced photoelectrochemical water oxidation on WO3 photoanode, 77 (2020) 105190.

[6] M. Tayebi, A. Tayyebi, Z. Masoumi, B.-K. Lee, Photocorrosion suppression and photoelectrochemical (PEC) enhancement of ZnO via hybridization with graphene nanosheets, Applied Surface Science, 502 (2020) 144189.

[7] M. Guo, Z. Xing, T. Zhao, Y. Qiu, B. Tao, Z. Li, W. Zhou, Hollow flower-like polyhedral α-Fe2O3/Defective MoS2/Ag Z-scheme heterojunctions with enhanced photocatalytic-Fenton performance via surface plasmon resonance and photothermal effects, Applied Catalysis B: Environmental, (2020) 118978.

[8] Y. Tang, Z. Zheng, X. Sun, X. Li, L. Li, Ternary CdS-MoS2 coated ZnO nanobrush photoelectrode for one-dimensional acceleration of charge separation upon visible light illumination, Chemical Engineering Journal, 368 (2019) 448-458.

[9] M. Faraji, M. Yousefi, S. Yousefzadeh, M. Zirak, N. Naseri, T.H. Jeon, W. Choi, A.Z. Moshfegh, Two-dimensional materials in semiconductor photoelectrocatalytic systems for water splitting, Energy & Environmental Science, 12 (2019) 59-95.

[10] Y. Qu, X. Song, X. Chen, X. Fan, G. Zhang, Tuning charge transfer process of MoS2 photoanode for enhanced photoelectrochemical conversion of ammonia in water into gaseous nitrogen, Chemical Engineering Journal, 382 (2020) 123048.

[11] C. Backes, R.J. Smith, N. McEvoy, N.C. Berner, D. McCloskey, H.C. Nerl, A. O'Neill, P.J. King, T. Higgins, D.J.N.c. Hanlon, Edge and confinement effects allow in situ measurement of size and thickness of liquid-exfoliated nanosheets, 5 (2014) 1-10.

[12] Z. Masoumi, M. Tayebi, B.-K. Lee, Ultrasonication-assisted liquid-phase exfoliation enhances photoelectrochemical performance in α-Fe2O3/MoS2 photoanode, Ultrasonics Sonochemistry, 72 (2021) 105403.

[13] P. Peerakiatkhajohn, J.H. Yun, H. Chen, M. Lyu, T. Butburee, L. Wang, Stable hematite nanosheet photoanodes for enhanced photoelectrochemical water splitting, Advanced Materials, 28 (2016) 6405-6410.

[14] J. Jian, H. Chang, T. Xu, Structure and Properties of Single-Layer MoS2 for Nano-Photoelectric Devices, Materials, 12 (2019) 198.

[15] S. Shen, C.X. Kronawitter, J. Jiang, S.S. Mao, L. Guo, Surface tuning for promoted charge transfer in hematite nanorod arrays as water-splitting photoanodes, Nano Research, 5 (2012) 327-336.

[16] A.A. Bortoti, A. de Freitas Gavanski, Y.R. Velazquez, A. Galli, E.G. de Castro, Facile and low cost oxidative conversion of MoS2 in α-MoO3: Synthesis, characterization and application, Journal of Solid State Chemistry, 252 (2017) 111-118.

[17] L. Wang, N.T. Nguyen, X. Huang, P. Schmuki, Y. Bi, Hematite photoanodes: synergetic enhancement of light harvesting and charge management by sandwiched with Fe2TiO5/Fe2O3/Pt structures, Advanced Functional Materials, 27 (2017) 1703527.

[18] F. Ruggieri, D. Di Camillo, L. Maccarone, S. Santucci, L. Lozzi, Electrospun Cu-, W-and Fe-doped TiO 2 nanofibres for photocatalytic degradation of rhodamine 6G, Journal of nanoparticle research, 15 (2013) 1982.
[19] Z. Zhang, L. Zhang, B. Chen, M. Baek, K. Yong, Efficient Photoconversion and Charge Separation of a (Mn2+-Fe2O3)/Reduced Graphene Oxide/(Fe3+-WO3) Photoelectrochemical Anode via Band-Structure Modulation, ACS Sustainable Chemistry & Engineering, 6 (2018) 13462-13472.
[20] C.M. Tian, W.W. Li, Y.M. Lin, Z.Z. Yang, L. Wang, Y.G. Du, H.Y. Xiao, L. Qiao, J.Y. Zhang, L. Chen, D.-C. Qi, J.L. MacManus-Driscoll, K.H.L. Zhang, Electronic Structure, Optical Properties, and Photoelectrochemical Activity of Sn-Doped Fe2O3 Thin Films, The Journal of Physical Chemistry C, 124 (2020) 12548-12558.
[21] J. Shi, Y. Luo, H. Wei, J. Luo, J. Dong, S. Lv, J. Xiao, Y. Xu, L. Zhu, X. Xu, H. Wu, D. Li, Q. Meng, Modified Two-Step Deposition Method for High-Efficiency TiO2/CH3NH3PbI3 Heterojunction Solar Cells, ACS Applied Materials & Interfaces, 6 (2014) 9711-9718.
[22] S. Arab, M. Yao, C. Zhou, P. Daniel Dapkus, S.B. Cronin, Doping concentration dependence of the photoluminescence spectra of n-type GaAs nanowires, Applied Physics Letters, 108 (2016) 182106.
[23] H.-J. Ahn, K.-Y. Yoon, M.-J. Kwak, J.-S. Lee, P. Thiyagarajan, J.-H. Jang, MoS x supported hematite with enhanced photoelectrochemical performance, Journal of Materials Chemistry A, 3 (2015) 21444-21450.
[24] J. Sun, L. Li, S. Ge, P. Zhao, P. Zhu, M. Wang, J. Yu, Dual-Mode Aptasensor Assembled by a WO3/Fe2O3 Heterojunction for Paper-Based Colorimetric Prediction/Photoelectrochemical Multicomponent Analysis, ACS Applied Materials & Interfaces, 13 (2021) 3645-3652.
[25] M. Tayebi, A. Tayyebi, B.-K. Lee, Photocharged molybdenum-doped BiVO4 photoanodes for simultaneous enhancements in charge transport and surface passivation, Solar Energy, 191 (2019) 427-434.
[26] D. Cao, W. Luo, J. Feng, X. Zhao, Z. Li, Z. Zou, Cathodic shift of onset potential for water oxidation on a Ti 4+ doped Fe 2 O 3 photoanode by suppressing the back reaction, Energy & Environmental Science, 7 (2014) 752-759.
[27] X. Fan, T. Wang, H. Xue, B. Gao, S. Zhang, H. Gong, H. Guo, L. Song, W. Xia, J. He, Synthesis of Tungsten Trioxide/Hematite Core-Shell Nanoarrays for Efficient Photoelectrochemical Water Splitting, ChemElectroChem, 6 (2019) 543-551.
[28] I.S. Cho, C.H. Lee, Y. Feng, M. Logar, P.M. Rao, L. Cai, D.R. Kim, R. Sinclair, X. Zheng, Codoping titanium dioxide nanowires with tungsten and carbon for enhanced photoelectrochemical performance, Nature communications, 4 (2013) 1-10.
[29] B. Klahr, S. Gimenez, F. Fabregat-Santiago, J. Bisquert, T.W. Hamann, Photoelectrochemical and Impedance Spectroscopic Investigation of Water Oxidation with “Co–Pi”-Coated Hematite Electrodes, Journal of the American Chemical Society, 134 (2012) 16693-16700.
[30] Q. Che, X. Zhou, Q. Liu, Y. Tan, Q. Li, Synthesis of an in situ core–shell interlink ultrathin-nanosheet Fe@FexNiO/Ni@NiyCoP nanohybrid by scalable layer-to-layer assembly strategy as an ultra-highly efficient bifunctional electrocatalyst for alkaline/neutral water reduction/oxidation, Journal of Materials Chemistry A, 9 (2021) 5833-5847.
[31] M. Tayebi, Z. Masoumi, B.-K. Lee, Ultrasonically prepared photocatalyst of W/WO3 nanoplates with WS2 nanosheets as 2D material for improving photoelectrochemical water splitting, Ultrasonics Sonochemistry, (2020) 105339.
[32] P. Tang, H. Xie, C. Ros, L. Han, M. Biset-Peiró, Y. He, W. Kramer, A.P. Rodríguez, E. Saucedo, J.R. Galán-Mascarós, Enhanced photoelectrochemical water splitting of hematite multilayer nanowire photoanodes by tuning the surface state via bottom-up interfacial engineering, Energy & Environmental Science, 10 (2017) 2124-2136.
[33] G. Liu, Y. Zhao, R. Yao, N. Li, M. Wang, H. Ren, J. Li, C. Zhao, Realizing high performance solar water oxidation for Ti-doped hematite nanoarrays by synergistic decoration with ultrathin cobalt-iron phosphate nanolayers, Chemical Engineering Journal, 355 (2019) 49-57.
[34] M. Tayebi, B.-K. Lee, The effects of W/Mo-co-doped BiVO4 photoanodes for improving photoelectrochemical water splitting performance, Catalysis Today, 361 (2021) 183-190.
[35] M. Tayebi, A. Tayyebi, T. Soltani, B.-K. Lee, pH-Dependent photocatalytic performance of modified bismuth vanadate by bismuth ferrite, New Journal of Chemistry, 43 (2019) 9106-9115.

[36] B. Lei, D. Xu, B. Wei, T. Xie, C. Xiao, W. Jin, L. Xu, In Situ Synthesis of α-Fe2O3/Fe3O4 Heterojunction Photoanode via Fast Flame Annealing for Enhanced Charge Separation and Water Oxidation, ACS Applied Materials & Interfaces, 13 (2021) 4785-4795.
[37] Y. Guo, T. Liu, N. Wang, Q. Luo, H. Lin, J. Li, Q. Jiang, L. Wu, Z. Guo, Ni-doped α-Fe2O3 as electron transporting material for planar heterojunction perovskite solar cells with improved efficiency, reduced hysteresis and ultraviolet stability, Nano Energy, 38 (2017) 193-200.
[38] H. Zhang, W.Y. Noh, F. Li, J.H. Kim, H.Y. Jeong, J.S. Lee, Three Birds, One-Stone Strategy for Hybrid Microwave Synthesis of Ta and Sn Codoped Fe2O3@FeTaO4 Nanorods for Photo-Electrochemical Water Oxidation, Adv. Funct. Mater., 29 (2019) 1805737.
[39] S.Y. Lee, U.J. Kim, J. Chung, H. Nam, H.Y. Jeong, G.H. Han, H. Kim, H.M. Oh, H. Lee, H. Kim, Y.-G. Roh, J. Kim, S.W. Hwang, Y. Park, Y.H. Lee, Large Work Function Modulation of Monolayer MoS2 by Ambient Gases, ACS Nano, 10 (2016) 6100-6107.

Chapter 4 - Section 2 - Multi Heterojunction

Unified surface modification by double heterojunction of MoS_2 nanosheets and $BiVO_4$ nanoparticles to enhance the photoelectrochemical water splitting of hematite photoanode

Abstract:

Metal oxide semiconductors are among the most promising photoelectrode materials for solar water splitting, mainly due to their robustness in aqueous solutions. In this work, a multi heterojunction with metal oxides is fabricated to enhance the photoelectrochemical (PEC) water splitting through unified surface modification. The two-dimensional MoS_2 nanosheets are synthesized through the liquid-phase exfoliation (LPE) process. The characteristics of the MoS_2 nanosheets for improving light harvest and charge separation, including thickness, number of layers, and concentration, are all estimated using the proper techniques. The best photocurrent density of the α-Fe_2O_3/$BiVO_4$/MoS_2 at 1.23V vs. RHE under 100 mW/cm^2 (AM 1.5) illumination that was identified around 15 times greater than that of the α-Fe_2O_3 photoanode. The α-Fe_2O_3/$BiVO_4$/MoS_2 electrode shows the highest donor concentration value (4.36E+26 m^3) with the lowest flat band potential (0.15 V) among all the prepared electrodes. Furthermore, the obtained hydrogen and oxygen production in 2h irradiation for α-Fe_2O_3/$BiVO_4$/MoS_2 is 46.5 and 22.3 μmol.cm^{-2}, respectively.

4.2.1. Introduction:

Finding the proper solutions to mitigate both environmental pollution and energy shortage is a high priority when researching best way to support the sustainable growth of modern societies [1]. Recently, photoelectrochemical (PEC) techniques have become increasingly attractive methods for the overcoming of serious problems related to many chemical and environmental applications and sustainable energy generation, such in chemical synthesis [2], biosensing , organic pollutant degradation [3], water splitting fuel generation [4], and solar rechargeable battery [5]. For PEC water splitting, semiconductors can make clean chemical fuels by converting solar energy into oxygen and hydrogen through the splitting of water [6]. Among the different semiconductors, metal oxides such as TiO_2[7], α-Fe_2O_3 [8], WO_3 , and $BiVO_4$ [9] are among the most promising photoanode materials for usage in this process, as they are stable, non-toxic, low-cost, and have a suitable bandgap for generating electron-hole pairs for usage in photocatalysis applications [10]. To enhance the water oxidation in a half-reaction at the surface of the photoanodes, it is required to build a narrow and suitable bandgap with a proper valence band position [11].

Hematite (α-Fe_2O_3) has many advantages, including the possession of a small bandgap (2.0–2.2 eV), the fact that it exists in abundant quantities, and its strong stability in PEC efficiency [12]. The predicted theoretical efficiency of α-Fe_2O_3 is 12.4%; however, its short hole diffusion length (~2-4 nm), positive conduction band edge, and slow charge carrier mobility are few of the drawbacks that occur while achieving this high efficiency [13]. Bismuth vanadate ($BiVO_4$) is also utilized for water oxidation, as it is a properly visible light photocatalyst with high theoretical conversion efficiency (9.1%) and a suitable band gap (2.4 eV) [14]. Two-dimensional (2D) Molybdenum disulfide (MoS_2) nanosheets have an optical band gap around 1.8 eV which can

easily extract the holes from a photoexcited absorber within the visible range through the fabrication of heterojunction with an n-type semiconductor [15]. Due to its unique optical, mechanical, and electronic properties, it has received great attention for its usage in various applications particularly through photo-electrocatalysis and electrocatalysis fields [16].

It should be noted that one of the most important limiting factors effects on PEC efficiency, is the recombination of charge carriers. Efficient strategies for enhancing PEC performance focus on the construction of a heterojunction between two or more semiconductors [17]. The forming of multicomponent heterojunctions can therefore facilitate the separation and transportation of charge carriers [18]. Furthermore, the heterojunction of semiconductors can enhance the efficiency of electron-hole separation by increasing the $\eta_{injection}$ and kinetics of charge carriers [19]. Therefore, charge carriers are generated in one photocatalyst, and then transferred vectorially to the other material through an offset in the energies of the conduction and valance band edges, thereby allowing for interfacial charge transfer from one semiconductor to another [20].

In this study, we fabricated the multi heterojunction of monoclinic $BiVO_4$ and MoS_2 nanosheet on the surface of the hematite photoanode with high PEC performance. The thickness, number of layers, and concentration parameters of the prepared MoS_2 precursor were investigated through AFM, UV-vis, and HRTEM analyses. The PEC properties of the α-Fe_2O_3/$BiVO_4$/MoS_2 photoelectrode were systematically studied which demonstrated a great enhancement of the PEC performance, containing incident photon conversion efficiency (IPCE), donor concentration (N_D), space charge layer thickness (W_{SCL}), flat band potential (V_{fb}), and applied bias photon-to-current efficiency (ABPE) are all analyzed and discussed based on the engineering multi-metal oxide heterojunction.

4.2.2. Experimental section:

4.2.2.1. Chemical and reagents:

For the purposes this study, Sodium nitrate ($NaNO_3$), iron (III) chloride hexahydrate ($FeCl_3 \cdot 6H_2O$), Bismuth nitrate pentahydrate ($Bi(NO_3)_3 \cdot 5H_2O$), Ammonium metavanadate (NH_4VO_3), acetic acid (CH_3COOH), nitric acid (HNO_3), and Hydrochloric acid (HCl) were all purchased from Daejung Chemical & Metal Co., Ltd (Korea). The bulk powder of molybdenum disulfide (MoS_2) was procured from the company Sigma-Aldrich. Deionized water was used to prepare all the aqueous solutions used in this study.

4.2.2.2. Preparation α-Fe_2O_3 photoanode:

The α-Fe_2O_3 thin film was fabricated on fluorine tin oxide (FTO) through a hydrothermal method. An aqueous solution consisting of a mixture of 1 M sodium nitrate ($NaNO_3$) and 0.15M ferric chloride ($FeCl_3.6H_2O$) was prepared as a precursor. Hydrochloric acid (HCl) was used to adjust towards a pH=1.5 with a slow drop wising to the solution. The clean FTO was put at the bottom of a Teflon container and then 80ml of the prepared precursor was added to it and was placed in the oven at 100°C for 6 hours. The residues on the coated FTO were washed with DI water and became the β-FeOOH. It was put in a furnace at 550°C for 3 hours and then a reddish orange α-Fe_2O_3 thin film was prepared.

4.2.2.3. Preparation of α-Fe_2O_3/$BiVO_4$:

The $BiVO_4$ thin film was fabricated through a dip-coating process. The precursor solution was prepared by mixing 6 mmol or 2.94 g of $Bi(NO_3)_3 \cdot 5H_2O$, 2.52 g citric acid, and 6 mmol or 0.702 g of NH_4VO_3 in 5 mL acetic acid, 30 mL of distilled water, and 15 mL of nitric acid. Furthermore, 3 g polyvinyl alcohol of Mw 89,000–98,000 was added into the solution slowly and then stirred for 4 hours at room temperature. To prepare the α-Fe_2O_3/$BiVO_4$ photoanode, the α-Fe_2O_3 electrode

was placed into the prepared precursor for the dip-coating process at a constant speed. The heating treatment was done at 330°C for 5 minutes in the air to improve the crystallinity between every cycle. The calcination process was completed after the optimized four dip-coating cycles and α-Fe_2O_3/$BiVO_4$ electrode was placed into the furnace at 450 °C for 10 hours.

4.2.2.3. Preparation of α-Fe_2O_3/$BiVO_4$/MoS_2:

The fabricating of the MoS_2 nanosheets was done through liquid-phase exfoliation (LPE) method and MoS_2 was then loaded onto the α-Fe_2O_3/$BiVO_4$ photoanode by drop-casting precursor. The precursor of the MoS_2 nanosheets was prepared by mixing 300 mg of MoS_2 bulk powder into 55 mL water, in addition to 45 mL Ethanol, to form an aqueous solution. They were exfoliated through continuous sonication for a period of 5 days. The dispersed solution was centrifuged at 3500 rpm for a period of 1 hour to create a monolayer, and then the top of the solution was collected for use. Finally, the optimized values (800 μL) of the MoS_2 nanosheets precursor were then dropped onto the α-Fe_2O_3/$BiVO_4$ electrode surface and the α-Fe_2O_3/$BiVO_4$/MoS_2 sample was placed into the furnace to calcinate for 2 hours at 450°C.

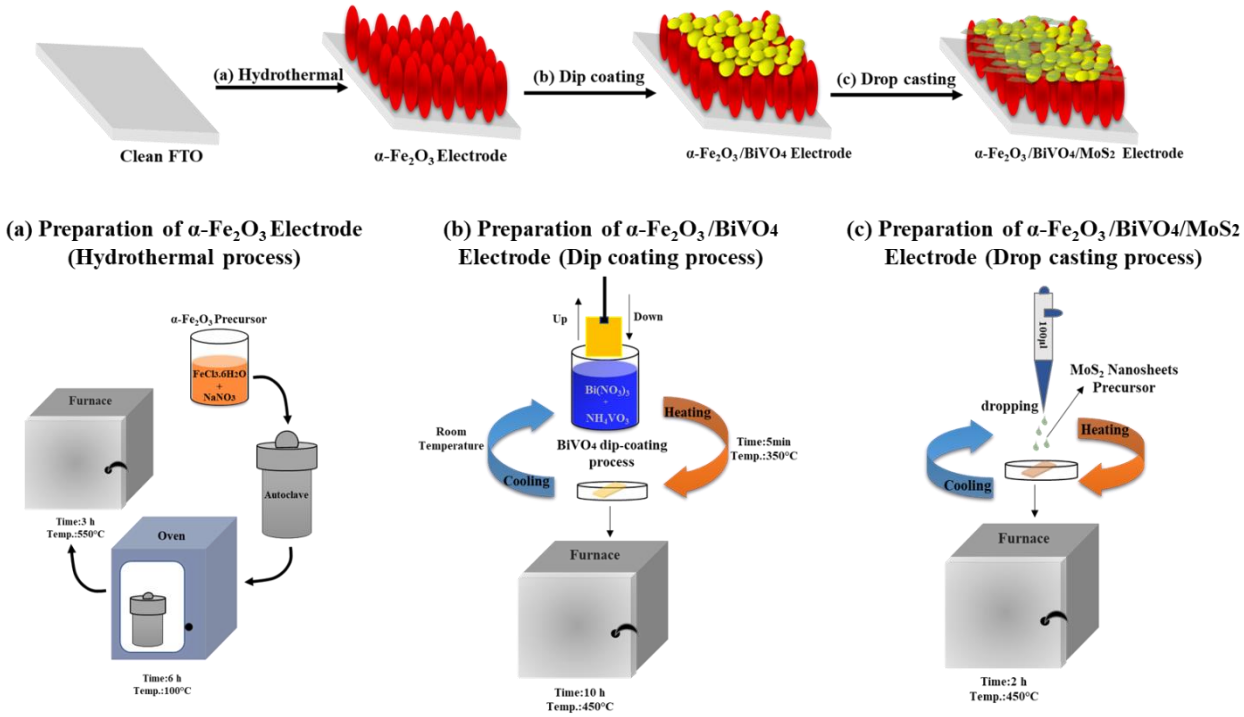

Fig. 1. The preparation processes of pure α-Fe_2O_3, α-Fe_2O_3/$BiVO_4$, and α-Fe_2O_3/$BiVO_4$/MoS_2 photoanodes.

4.2.2.4. Characterization Measurement:

The scanning electron microscope (SEM, Model Quanta 250 FEG) and transmission electron microscopy (TEM, JEOL, JEM-2100F) was used for morphological investigation of the α-Fe_2O_3, α-Fe_2O_3/$BiVO_4$, α-Fe_2O_3/$BiVO_4$/MoS_2 photoanodes. The structure and crystallinity of each catalytic electrodes were characterized by X-ray diffraction (XRD). Raman spectra (Bruker, model: Senteraa 2009, Germany) were used with the laser line in 785 nm as the excitation source at room temperature. The X-ray source was Bruker D8Advance with monochromatic Cu Kα radiation (λ=1.5406 Å) in 2θ range of 10–55°. Thermo Scientific Sigma Probe spectrometer, with a monochromatic AlKα source (photon energy 1486.6 eV), spot size of 400 µm, energy step size of 1.0 eV and pass energy of 200 eV, was used for detecting the chemical state of component elements in the electrodes. The optical properties of the thin films were measured by Perkin Elmer UV-Vis-NIR model Lambda 950. Photoluminescence (PL) spectra were detected at a room temperature

using Edinburgh F-4600 NF900 (FLS920) fluorescence spectrophotometer at an excitation on 400 nm.

4.2.2.5. Photoelectrochemical (PEC) Measurement:

In the PEC performance part, all data were measured with a standard three-electrode. The working electrodes that were prepared consist of α-Fe_2O_3, α-Fe_2O_3/$BiVO_4$, and α-Fe_2O_3/$BiVO_4$/MoS_2 photoanodes. A counter electrode is a platinum wire that was applied with an RHE reference electrode in 0.5 M Na_2SO_4 (pH≈7) aqueous solution as an electrolyte. The PEC measurements were done under 100 mW/cm^2 illumination of the front-side of the electrodes with a power intensity coming from 300W Xe lamp in the voltage range from 0.3 to 1.5 V (vs. RHE). The electrochemical impedance spectroscopy (EIS) was measured through the usage of potentiating with the identical electrode formation within the formation under light conditions whose frequency ranged from 10000 Hz to 0.1 Hz. Mott-Schottky analysis was also conducted under light conditions in 0.5 M Na_2SO_4 electrolyte with applied potential from 0.3 to 1.5V (vs. RHE) at 15 scan points. Incident Photon-to-electron Conversion Efficiency (IPCE) was measured by using different filters at 1.23V (vs. RHE) under the illumination level of 100 mW/cm^2 (AM 1.5). Furthermore, the applied bias photon-to-current efficiency (ABPE) was also displayed at the RHE scale using the following Eq. 1:

$$V_{RHE} = V_{Ag/AgCl} + 0.197 + 0.059\ pH \quad (1)$$

4.2.2.6. Hydrogen and Oxygen Evolution Measurement:

For overall water splitting of of α-Fe_2O_3, α-Fe_2O_3/$BiVO_4$ and α-Fe_2O_3/$BiVO_4$/MoS_2 photoanodes was evaluated by measuring the H_2 and O_2 evolution at 1.23 V versus RHE under 100 mW.cm^{-2} irradiations in 1M of NaOH electrolyte. The produced hydrogen and oxygen gas amounts were

measured using the gas chromatography (GC). Before starting the water splitting reaction nitrogen gas was purged into cell for 2 h to remove the air remaining in the reaction vessel. The light source was turned on and the amounts of evolved oxygen and hydrogen were measured by a tight syringe every 20 min using a gas chromatograph for 2h. The gas samples were injected in the GC, and the resulting peak areas ($AreaH_2$, $AreaO_2$) were recorded. The evolved hydrogen-oxygen gases were calculated according to the following formula[21]:

$$H_2(O_2)\mu mol.cm^{-2} = \left(\frac{Area\ of\ H_2 peak}{Slope\ of\ calibration\ curve}\right) \times (Head\ space\ volume) \times \left(\frac{1mol}{24.2\ L}\right) \quad (1)$$

The detailed calculation process for the Faradaic efficiency was shown as following:

Faradic efficiency = Actual photocurrent density/ Theoretical photocurrent density (2)

Actual photocurrent density = $N \times nH_2/O_2 \times F$ (3)

F is the Faraday constant which is 0.096487 C/μmol). nH_2/O_2 (μmol) is amount of H_2 or O_2 evolution determined by gas chromatography. N is number of electrons needed to evolve one molecule of H_2 or O_2. It is assumed that 2 electrons are needed to produce one molecule of H_2, and 4 electrons are needed for one molecule of O_2.

Theoretical photocurrent density= $Q = I \times t$ (4)

Q is quantity of charge (electricity) in coulombs (C). I is current in amperes (amps, A) and t is time (seconds).

4.2.3. Results and Discussion

4.2.3.1 Morphology and Structure of the Exfoliated MoS_2 Nanosheets

Fig. 4.2.2a indicates TEM images of prepared MoS_2 nanosheets using the LPE method with a lateral size between 100~150 nm. A high-resolution TEM image (Fig. 4.2.2b) shows that the lattice structure of the MoS_2 nanosheet was not damaged during the synthesis process. The electron

diffraction pattern (inset in Fig. 4.2.2b) indicates that a polycrystalline film of MoS_2 contains (0002), $\{10\bar{1}0\}$, and additionally $\{11\bar{2}0\}$ lattice fringes are visible. These few layers of MoS_2 nanosheets with a thickness (~6 nm), possessed an acceptable crystallinity during the synthesis process [22]. The UV-vis and AFM of the exfoliated MoS_2 nanosheets are shown in Figs. 4.2.2c and d. Due to the electronic band structure of MoS_2, optical absorption was measured by UV-Vis spectroscopy between the ultraviolet region to the near-infrared region. Points A, B, and C show in Fig. 4.2.2d represent the existence of a few layers of the MoS_2 nanosheets in the prepared precursor. The point C in MoS_2 is centered at 397.46 nm, while the B and A transitions are respectively placed at 609.36 nm and 669.92 nm, with these results indicating the significant contribution of the few-layered nanosheets. The concentration, length, and thickness of the exfoliated MoS_2 were calculated using equations 1, 2, and 3, which can be viewed in the chapter 2 part 1 [23].

AFM results can prove the estimate values for the number of MoS_2 layers based on the deposited height measurement. The average thickness from the height profile diagram was estimated at approximately 6 nm (Fig. 4.2.2c). Further, the length and the concentration of the few layers MoS_2 on each photoanode were calculated at 174.63 nm and 0.02 mg/ml, respectively.

The Raman analysis for MoS_2 nanosheets shows strong signals at around 388.7 and 413.2 (cm^{-1}) which corresponds to both the in-plane E^1_{2g} and the out-of-plane A_{1g} vibration (Fig. 4.2.2e). These two peaks were consistent with the observed peaks observed in exfoliated MoS_2 nanosheets. The Raman spectra of the MoS_2 nanosheets also display a frequency difference around 24.5 cm^{-1}, which can be attributed to the presence of four and five monolayers, respectively [24].

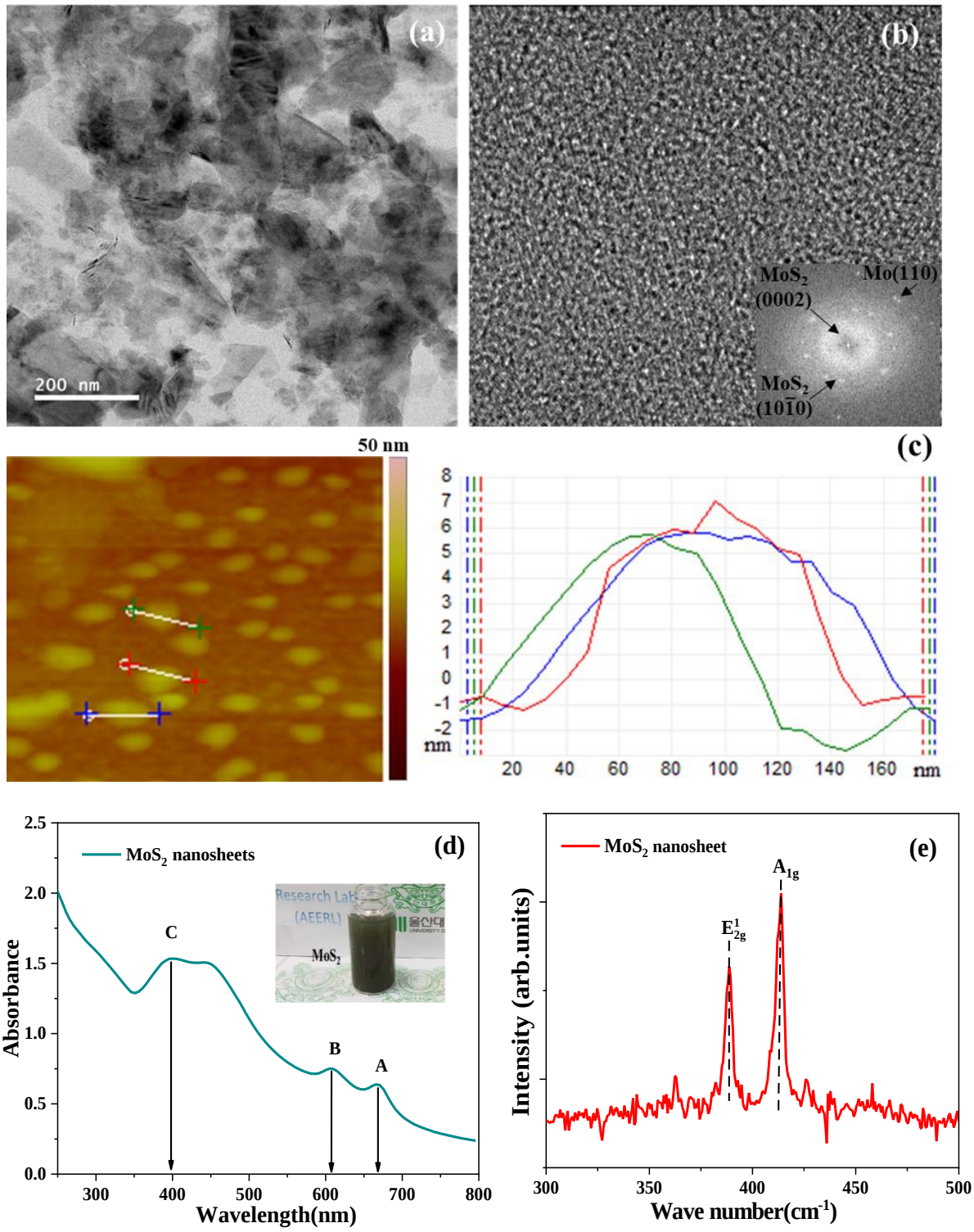

Fig. 4.2.2. (a, b) TEM images, (c) AFM, (d) UV-Vis, and (e) Raman analysis for MoS_2 nanosheets.

4.2.3.2 The Characterization of the Prepared Photoelectrodes

Fig. 4.2.3(a-c) shows the morphologies of the α-Fe_2O_3, α-Fe_2O_3/$BiVO_4$, and α-Fe_2O_3/$BiVO_4$/MoS_2 electrodes, which were analyzed using scanning electron microscopy (SEM) [25]. The Fig. 4.2.3a shows that the SEM of the prepared α-Fe_2O_3 is composed of many irregular rice-shape nanorods with a random size vertically aligned on the FTO substrate. After the first heterojunction with $BiVO_4$ the thickness increased ~50 nm, which is shown in the cross-section view of the α-Fe_2O_3/$BiVO_4$ thin film (Fig. 4.2.3b). However, the porous structure in the α-Fe_2O_3/$BiVO_4$ photoanode was greater, when compared to the pure α-Fe_2O_3 , mainly due to the depositing of a homogenous layer of $BiVO_4$ into a densely arranged structure on the surface of the α-Fe_2O_3 photoanode. In Fig. 4.2.3c, the MoS_2 nanosheets covered the surface of the α-Fe_2O_3/$BiVO_4$ thin film in the form of a shell, resulting in the growth of the nanorod's longer thickness (~520nm). The α-Fe_2O_3/$BiVO_4$/MoS_2 was shaped more densely when compared to the pure α-Fe_2O_3 and α-Fe_2O_3/$BiVO_4$ photoelectrodes. The α-Fe_2O_3/$BiVO_4$/MoS_2 photoelectrode with denser core-shell structure can harvest more light, which can therefore generate more electron-hole pairs, thereby leading to increased PEC performance [26]. The elemental composition of α-Fe_2O_3/$BiVO_4$ and α-Fe_2O_3/$BiVO_4$/MoS_2 photoelectrodes was confirmed using EDS and SEM mapping (Fig. 4.2.3g and 3h), which confirmed the existence of Fe, O, Bi, V, and Mo elements, and which generally aligns with their XPS results. [27].

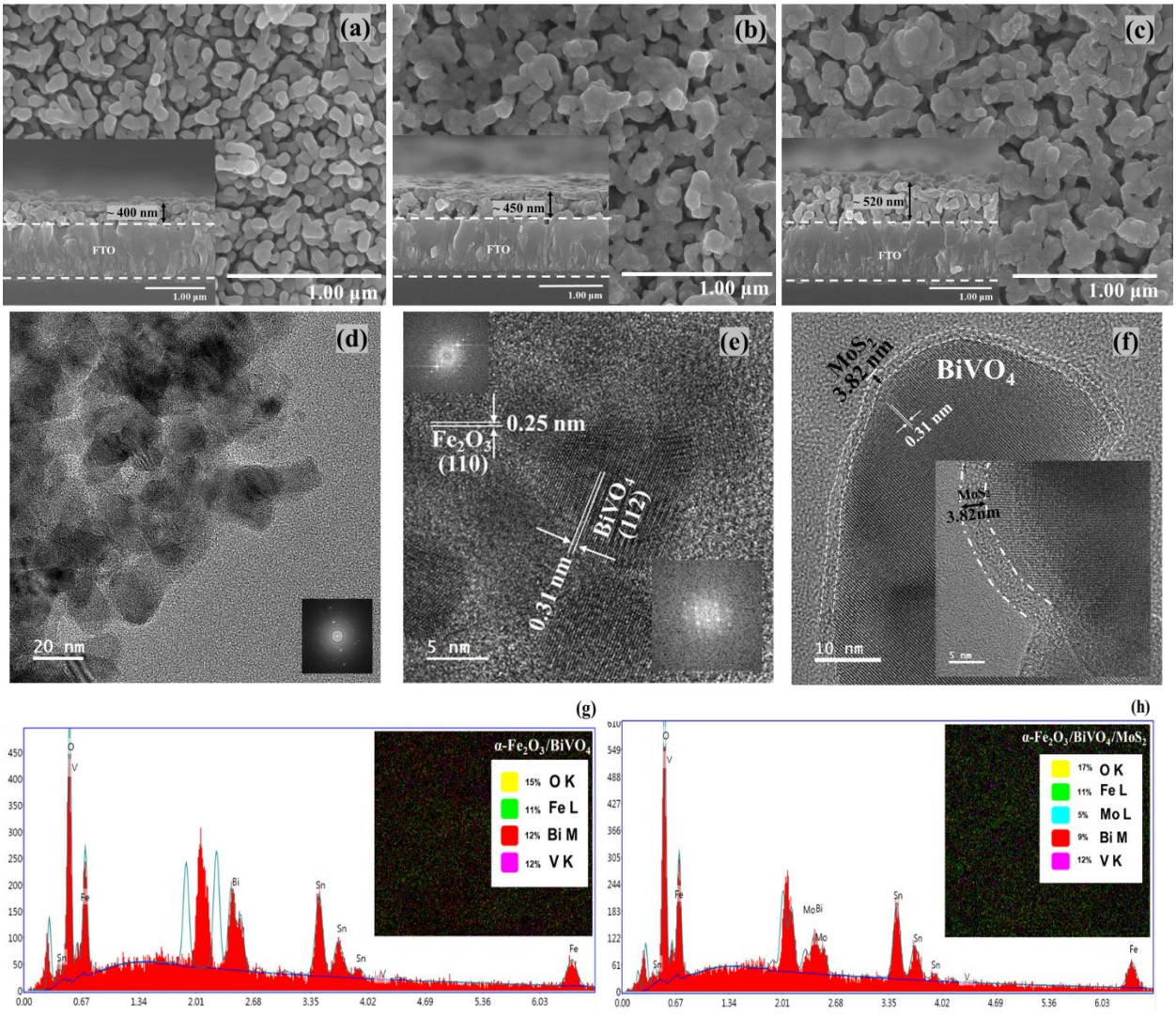

Fig. 4.2.3. The FE-SEM top-view and cross-sectional images of the surface of (a) α-Fe_2O_3, (b) α-Fe_2O_3/$BiVO_4$, (c) α-Fe_2O_3/$BiVO_4$/MoS_2 electrodes, respectively. The HRTEM of (d and e) α-Fe_2O_3/$BiVO_4$/MoS_2 structure, and (f) the thickness of deposited MoS_2 layers on α- $BiVO_4$. EDS and SEM mapping for (g) α-Fe_2O_3/$BiVO_4$, and (h) α-Fe_2O_3/$BiVO_4$/MoS_2 electrodes.

The HRTEM image of the α-Fe_2O_3/$BiVO_4$/MoS_2 sample was shown in Figs. 4.2.3(d-f). The rice-shape α-Fe_2O_3 and $BiVO_4$ nanoparticle can be observed in Fig. 4.2.3d. The lattice space 0.31 nm and 0.25 nm reveals the (112) plane of the monoclinic $BiVO_4$ structure and (110) plane of the α-Fe_2O_3 nanorods, respectively (Fig. 4.2.3e) [28]. Further, an apparent interface between MoS_2 nanosheets layer and covered α-Fe_2O_3/$BiVO_4$ structure is clearly observed in Fig. 4.2.3f. The thickness of the MoS_2 nanosheets layer can be estimated at around 3.82 nm using the existence of

interface (Fig. 4.2.3f) [25].

X-ray photoelectron spectroscopy (XPS) was used to investigate the chemical and electronic state of the elements in the composition. Fe2p, O1s, Bi4f, V2p, and Mo3d for use as photocatalysts are presented in Fig. 4.2.4. The XPS spectra of the pure α-Fe_2O_3 of all prepared electrodes are shown in two peaks for Fe2p (Fig. 4.2.4b). The two distinguished peaks were detected at around 710 eV and 724 eV banding energies, which corresponds to $Fe2p_{3/2}$ and $Fe2p_{1/2}$, respectively. The high-resolution XPS Fe 2p spectra (Fig. 4.2.4d) are deconvoluted into seven peaks. The peaks located around binding energy of 710 eV and 723 eV are assigned as the Fe^{2+}, which are attributed to the coexistence of Fe^{3+} as well as Fe^{2+} of Fe ($2p_{3/2}$) and the oxidation state of Fe (2p1/2), respectively. Two peaks with binding energies around 713 eV and 725 eV are allocated to the Fe^{3+} oxidation state of Fe ($2p_{1/2}$) and Fe ($2p_{3/2}$). The higher or lower binding energy peak at 709 eV and 703 eV may be possibly due to the electron-deficient Fe^{2+} sites, created by the breaking of Fe-O bonds. [29]. Fig. 4.2.4c shows the high-resolution XPS for O1s in the α-Fe_2O_3, α-Fe_2O_3/$BiVO_4$, and α-Fe_2O_3/$BiVO_4$/MoS_2 photoanodes. The O1s peaks of α-Fe_2O_3 deconvoluted into two peaks at 529.3 and 530.6 eV, which are assigned to the Fe-O and OH^-, respectively. After fabricating the multi heterojunctions, the peak around 532 eV corresponds to the metal bonds with oxygen (Bi-O or Bi/Mo-O), which confirms the successful formation of heterojunction [30]. There are two peaks at 163.92 eV and 158.6 eV for α-Fe_2O_3/$BiVO_4$ (Fig. 4.2.4d) which is determined to be $Bi4f_{5/2}$ and $Bi4f_{7/2}$ [31]. The binding energy values of Bi4f shift to a lower amount after loading the MoS_2 nanosheets onto the surface of the photoanode. This reduction can be attributed to the partial reduction of Bi^{3+} ions with the migration of electrons bound to oxygen toward metal ions resulting in oxygen vacancies [32]. Fig. 4.2.4e shows the two peaks of the V2p related to $BiVO_4$ in the α-Fe_2O_3/$BiVO_4$ and α-Fe_2O_3/$BiVO_4$/MoS_2 samples at 515.98 and 523.68 eV, which are assigned to

$V2p_{3/2}$ and $V2p_{1/2}$, respectively [33]. Furthermore, there are two peaks in the α-Fe_2O_3/$BiVO_4$/MoS_2 photoelectrode at 231.6 and 234.9 eV, which respectively correspond to Mo $3d_{5/2}$ and Mo $3d_{3/2}$ and therefore confirm the existence of Mo^{4+}, Mo^{6+} cations in MoS_2 (Fig. 4.2.4f). The appeared Mo^{6+} peaks in α-Fe_2O_3/$BiVO_4$/MoS_2 photoelectrode are deconvoluted at 231.5 eV ($Mo3d_{5/2}$) and 234.7 eV ($Mo3d_{3/2}$) and simultaneously correspond to Mo-metals bonds and the Mo bonds with the oxygen vacancy existing at the surface of the α-Fe_2O_3/$BiVO_4$/MoS_2 photoelectrode. The deconvoluted Mo^{4+} peaks are also detected at 231.9 eV ($Mo3d_{5/2}$) and 235.3 eV ($Mo3d_{3/2}$), thereby implying the Mo-S bonds at MoS_2 nanosheets [34]. Therefore, the Mo peaks represent the natural metal ion and oxygen vacancy existing on surface defects [35]. The XPS analysis for the sulfur element detection were very noisy with the smooth line showing S2p3/2 and S2p1/2 at 159.3 and 164.5 eV, respectively. This may be related to the high annealing temperature. This analysis can support the conversion of MoS_2 into MoO_3 during the calcination process [36]. The survey spectrum confirmed the coexisted of Fe, O, Bi, V, and Mo elements on the surface (Fig. 4.2.4a), while the C 1s peak at around 285 eV was shown to be related to adventitious carbon from the XPS equipment.

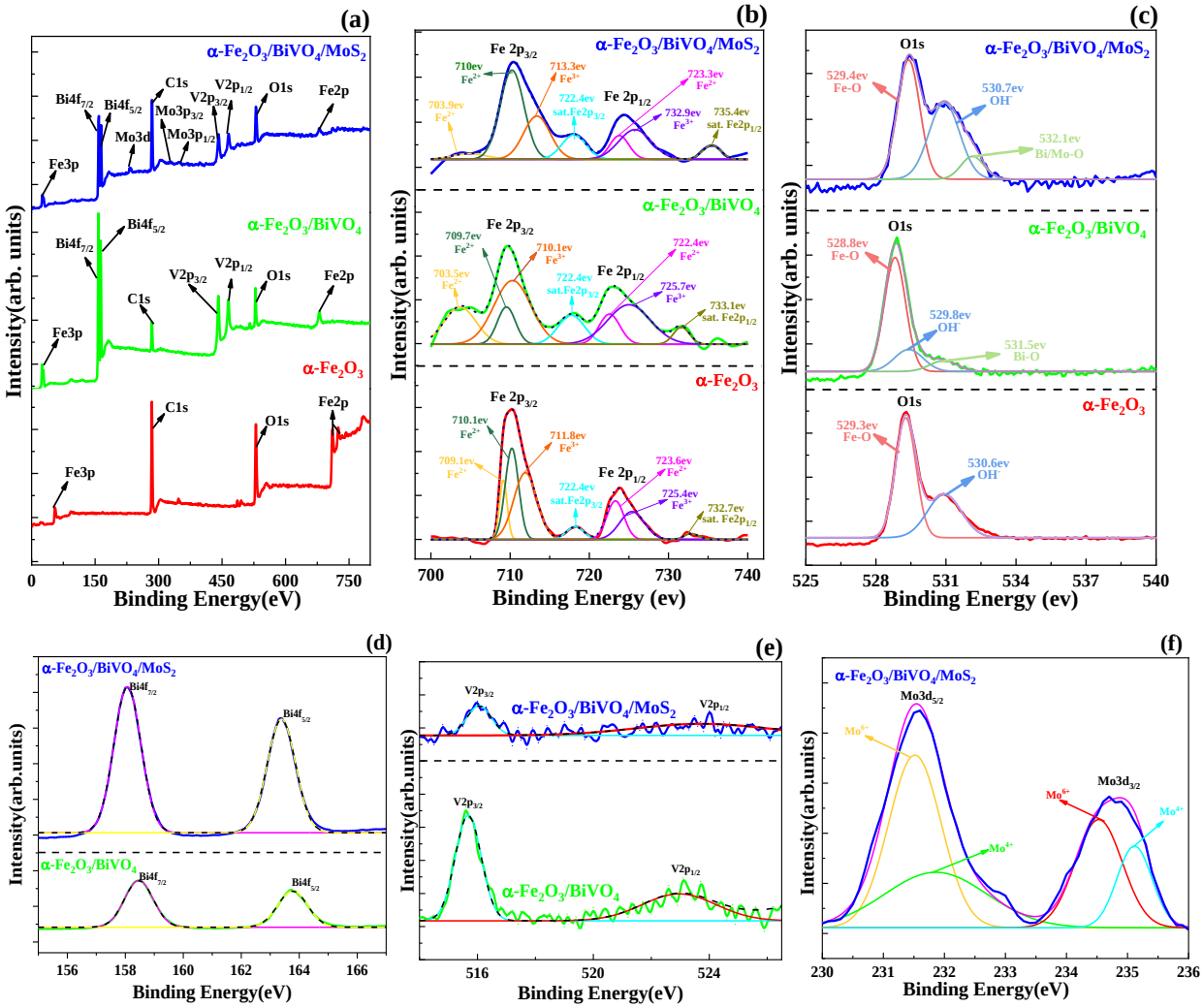

Fig. 4.2.4. The XPS spectra for (a) survey, (b)Fe2p, (c)O1s, (d)Bi4f, (e)V2p, and (f) Mo3d for all the α-Fe2O3 based electrodes.

The crystallographic structure of the α-Fe_2O_3, α-Fe_2O_3/$BiVO_4$, and α-Fe_2O_3/$BiVO_4$/MoS_2 photoanodes were analyzed using an X-ray diffraction (XRD) technique (Fig. 4.2.5a). The diffraction peaks corresponding to FTO as a substrate are consistent with the JCPDS data card (PDF 99-0024). The peaks related to α-Fe_2O_3 were detected within the XRD data containing 33, 36, 62, and 66° which belonged to the 104, 110, 214, and 300 lattice planes, respectively, thereby confirming the existence of the α-Fe_2O_3's strong crystalline structure in all three samples (PDF 02-0915)[37]. It is notable that double heterojunction into α-Fe_2O_3 lattice has no effect on the crystallization of α-Fe_2O_3, and that all samples present similar diffraction peaks, which can be

indexed to the α-Fe_2O_3 phase. The characteristic peaks of $BiVO_4$ exist at around 23, 28, 31, and 33° are related to the 200, 112, 200, and 020 lattice planes, respectively, thereby confirming the existence of the $BiVO_4$ thin layer in the α-Fe_2O_3/$BiVO_4$ and α-Fe_2O_3/$BiVO_4$/MoS_2 samples (PDF 14–0688) [38]. The diffraction patterns of α-Fe_2O_3/$BiVO_4$/MoS_2 thin film shows a peak at around 22°, which corresponds to 100 lattice plane of the MoS_2 nanosheets on the surface of the α-Fe_2O_3/$BiVO_4$/MoS_2 electrode (PDF 73-1508)[39]. The Raman spectra of the α-Fe_2O_3, α-Fe_2O_3/$BiVO_4$, and α-Fe_2O_3/$BiVO_4$/MoS_2 photoanodes are presented in Fig. 4.2.5b. The Raman bands for the α-Fe_2O_3 photoanode were reported at about 293, 496, 608, and 1309 cm^{-1}, which can be specified to the surface disorder of the α-Fe_2O_3 films that were detected in all samples [40]. The most important Raman bands of the $BiVO_4$ can provide structural information at around 712, and 828 cm^{-1}, and were observed in the α-Fe_2O_3/$BiVO_4$ and α-Fe_2O_3/$BiVO_4$/MoS_2 samples. These two bands can be attributed to the symmetric and antisymmetric stretching vibration modes of the VO_4 tetrahedra and V-O... Fe stretching [41]. There were not any extra peaks related to the MoS_2 nanosheets because it is difficult to detect molecules at low concentration in the Raman spectra.

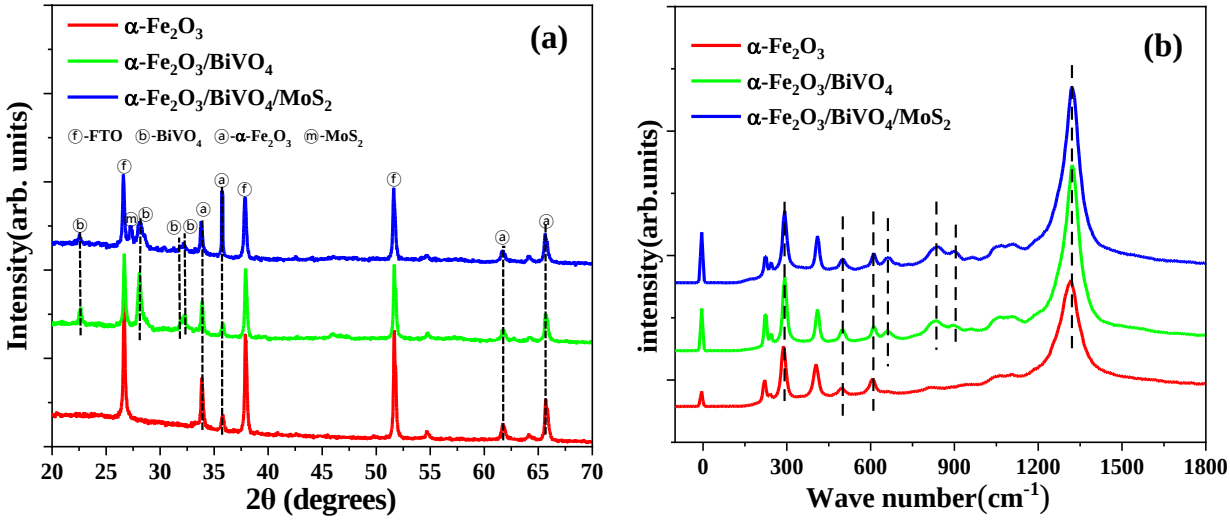

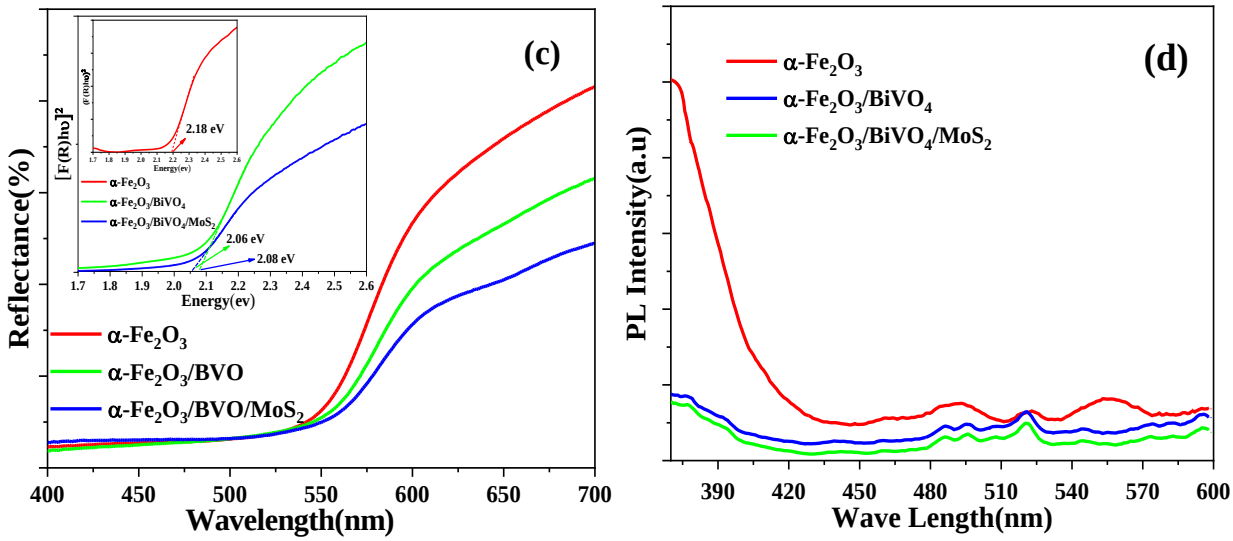

Fig. 4.2.5. (a) The X-ray diffraction (XRD) patterns, (b) Raman spectroscopy, (c) UV–vis reflectance spectra (inside: the band gap of pure α-Fe_2O_3), and (d) PL, of the α-Fe_2O_3, α-Fe_2O_3/$BiVO_4$ and α-Fe_2O_3/$BiVO_4$/MoS_2 electrodes.

The light reflectance of all samples is shown in Fig. 4.2.5c, along with UV–vis spectroscopy measurement. The reflectance was slightly reduced from that of pure α-Fe_2O_3 through the engineering heterojunction of α-Fe_2O_3 with $BiVO_4$ and $BiVO_4$/MoS_2. This reduction could allow the prepared photoelectrodes to absorb greater energy from photons and thereby generate a greater number of electron-hole pairs as compared with those of the pure α-Fe_2O_3 electrode. The bandgap for pure hematite shown in Fig. 4.2.5c is estimated at 2.18 eV. The bandgap of α-Fe_2O_3 /$BiVO_4$ was approximately calculated to be 2.08 eV from the absorbance (inside Fig. 4.2.5c). Furthermore, the bandgap of photoanode in the presence of the MoS_2 nanosheets was also estimated to be at 2.06 eV with the use of UV absorption, which is shown inside of Fig. 4.2.5c.

The recombination of photogenerated electron-hole pairs and the charge trapping can be identified with photoluminescence (PL) spectrum analysis. The PL spectra of the prepared photoelectrodes are shown in Fig. 4.2.5d. The high PL intensity of pure α-Fe_2O_3 can be attributed to the high electron–hole pair recombination. In the first heterojunction (α-Fe_2O_3/$BiVO_4$), the intensity of the peaks is lower, which indicates that the charge carrier recombination is significantly decreased in

the first heterojunction when compared to that of the pure α-Fe_2O_3. The second heterojunction (α-Fe_2O_3/$BiVO_4$/MoS_2) shows a lower PL intensity than that of α-Fe_2O_3/$BiVO_4$ indicating a high charge separation efficiency in the α-Fe_2O_3/$BiVO_4$/MoS_2 photoanode (Fig. 4.2.5d). This reduced PL intensity supports that the construction of the multi heterojunction can facilitate charge transfer pathway for the α-Fe_2O_3/$BiVO_4$/MoS_2 photoelectrode [23].

4.2.3.3. The PEC performance of the photoelectrodes

Figs. 4.2.6a and b exhibit the linear scan voltammetry (LSV) of pure α-Fe_2O_3, α-Fe_2O_3/$BiVO_4$, and α-Fe_2O_3/$BiVO_4$/MoS_2 photoelectrodes under continuous and on-off cycles between -0.3 to 1.5 V vs. RHE. The photocurrent density for all the samples is around zero in dark conditions. Pure α-Fe_2O_3 photoelectrode shows a weak photo response due to the high rate of the charge carriers' recombination. The modified α-Fe_2O_3 photocurrent density reaches approximately 0.7 and 1.67 $mA.cm^{-2}$ for α-Fe_2O_3/$BiVO_4$ and α-Fe_2O_3/$BiVO_4$/MoS_2 at 1.23 V vs. RHE, respectively (Fig. 4.2.6a). After designed multi heterojunction, the onset potential in α-Fe_2O_3/$BiVO_4$/MoS_2 photoelectrode shifts to a notably lower applied voltage, and the photocurrent density increased 15 times as when compared to that of the pure α-Fe_2O_3 thin film (Fig. 4.2.6a). This efficiency can be attributed to the double heterojunction of α-Fe_2O_3 with $BiVO_4$ nanoparticle and 2D MoS_2 nanosheets, which increased the photogenerated electron-hole pairs, thereby reducing the rate of the charge carriers' recombination, and facilitating the hole transfer to the surface photoanode [42]. Fig. 4.2.6b represents the chopped LSV which scans the photocurrent prompt, resulting in a quick reaction to the light in 2s on-off. This is consistent with the photocurrent density of LSV.

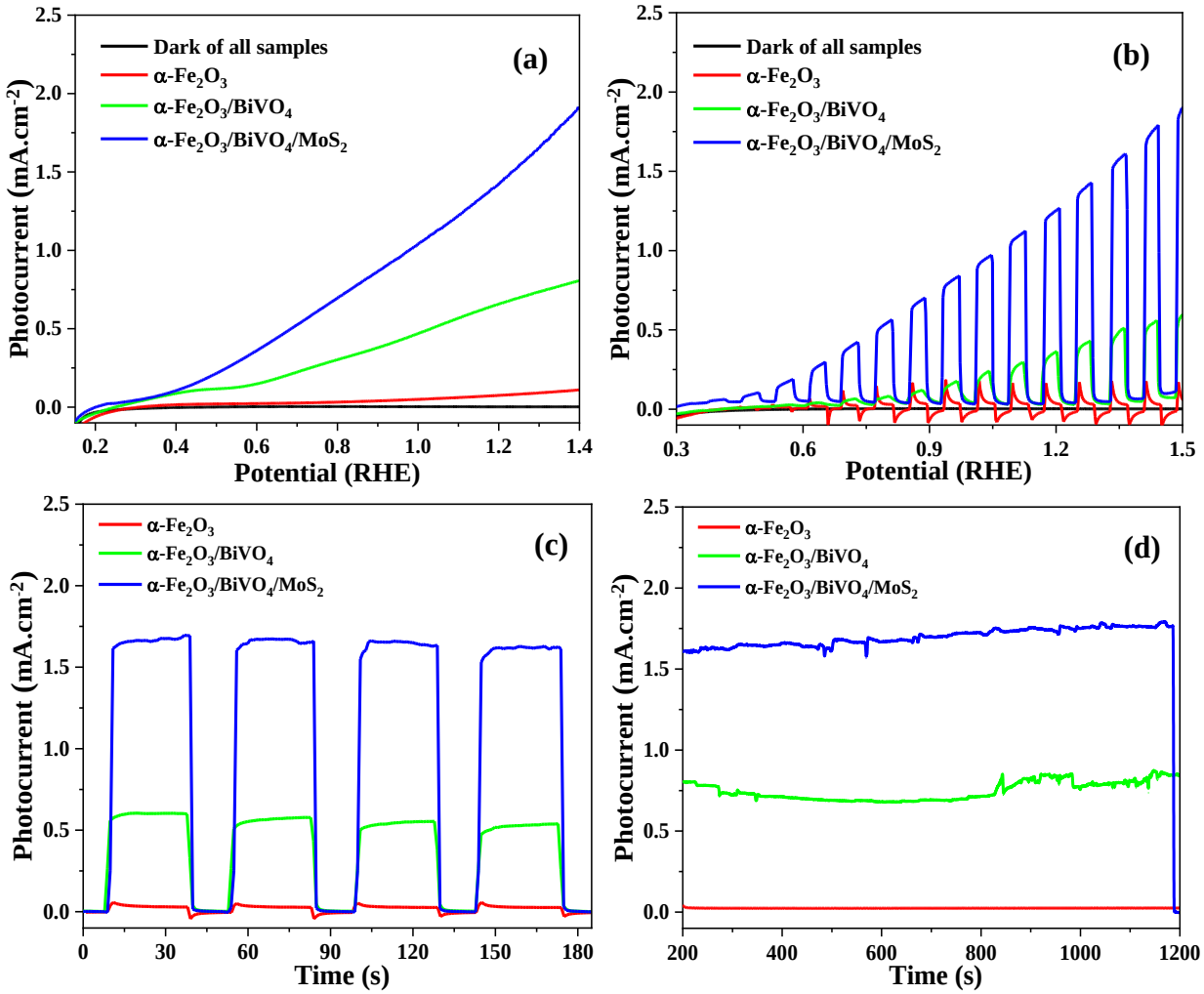

Fig. 4.2.6 (a) A linear scan voltammetry and (b) chopped LSV, (c) photocurrent response, and (d) photocurrent stability at 1.23 RHE for α-Fe_2O_3/$BiVO_4$ and α-Fe_2O_3/$BiVO_4$/MoS_2 electrodes under 100 mW/cm^2 illuminations. The electrolyte was a 0.5 M Na_2SO_4.

Figs. 4.2.6c and d exhibit the photocurrent response and stability through the chronoamperometry analysis of the α-Fe_2O_3, α-Fe_2O_3/$BiVO_4$, and α-Fe_2O_3/$BiVO_4$/MoS_2 electrodes at a constant potential of 1.23 V vs. RHE. In Fig. 6c, the photocurrent vs. time (i-t) was measured under an illumination level of 100 mW/cm^2 for 4 on-off cycles consisting of 30 seconds on and 15 seconds off. Fig. 4.2.6d shows that the photocurrent of α-Fe_2O_3/$BiVO_4$/MoS_2 has stability under 15 minutes of continuous illumination, which exhibits stable photocurrent without any significant downturn. The applied bias photon-to-current conversion efficiency (ABPE), as shown in Fig. 4.2.7a, was

estimated under the different applied potentials from LSV using Eq. (2) [42].

$$\text{ABPE (\%)} = \left(\frac{J\left(\frac{mA}{cm2}\right)\times(1.23-Vbias)(V)}{P\left(\frac{mW}{cm2}\right)}\right) \quad (2)$$

In this equation, V represents the applied potential, P represents the power density of the incident light, 100mW/cm^2 (AM 1.5), and J is the net photocurrent density at different potentials. The ABPE values of the α-Fe_2O_3/$BiVO_4$/MoS_2 photoanode are higher than those of the pure α-Fe_2O_3 and α-Fe_2O_3/$BiVO_4$ over the measured potential range. The highest ABPE value was around 0.28% at 0.85 V (RHE) for the α-Fe_2O_3/$BiVO_4$/MoS_2 photoelectrode, which is around 18.7 and 4 times higher than that of pure α-Fe_2O_3 (0.015%) and α-Fe_2O_3/$BiVO_4$ (0.071%) at 0.98 V (RHE), respectively. The significant shift to the lower potential took place through the occurrence of double heterojunction, which could be related to the shifting of the onset potential and the improvement of the conductivity of the α-Fe_2O_3/$BiVO_4$/MoS_2 electrode due to the reduction in recombination rate [42].

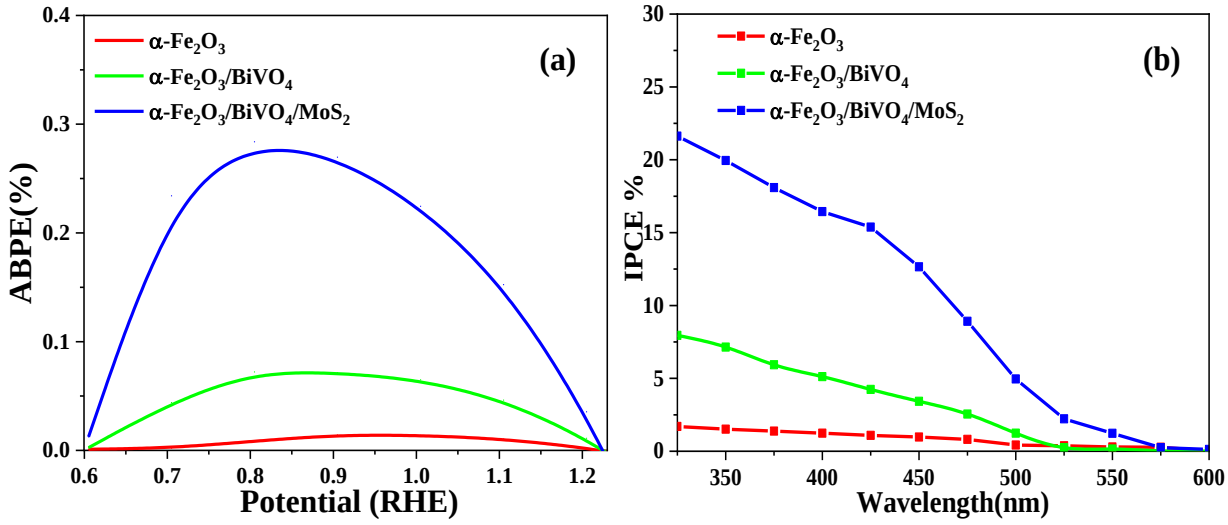

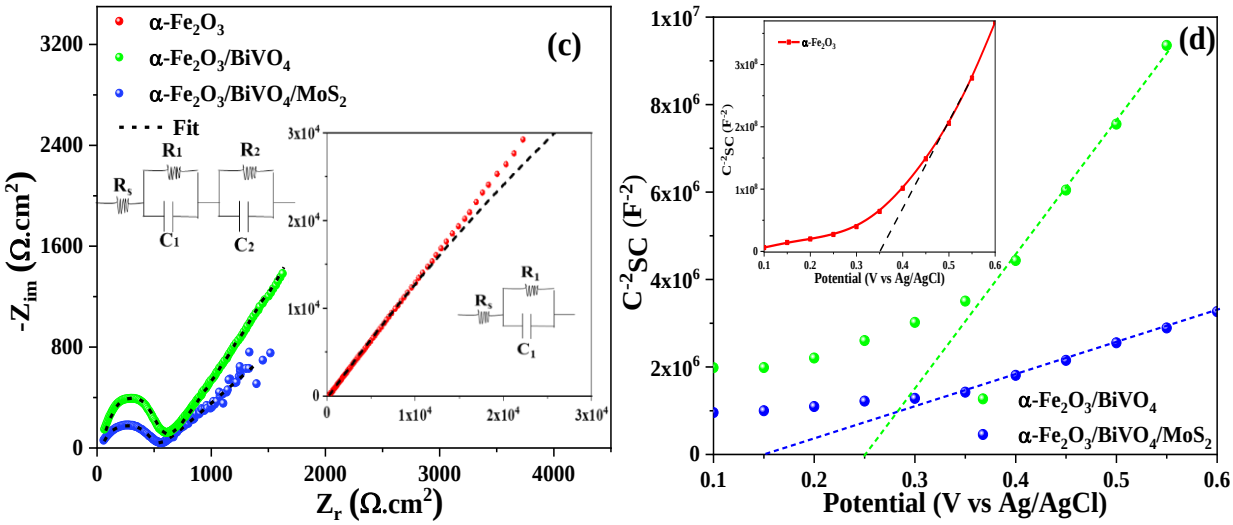

Fig. 4.2.7 (a) ABPE, and (b) IPCE, (c) Nyquist plot with equivalent circuit model inside, and (d) Mott–Schottky plot for α-Fe_2O_3, α-Fe_2O_3/$BiVO_4$ and α-Fe_2O_3/$BiVO_4$/MoS_2 electrodes. The supporting electrolyte was a 0.5 M aqueous solution of Na_2SO_4.

The efficiency of the prepared photoanodes to convert the incident light into photocurrent at different wavelengths, IPCE (%) was measured for α-Fe_2O_3, α-Fe_2O_3/$BiVO_4$, and α-Fe_2O_3/$BiVO_4$/MoS_2 photoelectrodes (Fig. 4.2.7b). Eq. (3) was used to calculate IPCE values:

$$IPCE\ (\%) = \left[\frac{1240}{\lambda(nm)} \times \frac{J_{light} - J_{dark}}{P(\lambda)}\right] \times 100 \qquad (3)$$

The α-Fe_2O_3 possessing a high recombination rate of charge carriers converted only 1.8% of the incident light in the wavelength range of 300 to 600nm at 1.23 V vs. RHE. The IPCE of α-Fe_2O_3 decreased to around zero at a wavelength higher than 450 nm due to its band edge at a wavelength of around 550 nm. The IPCE result showed that the photon conversion efficiency increased around 4 to 11 times for α-Fe_2O_3/$BiVO_4$ (8%) and α-Fe_2O_3/$BiVO_4$/MoS_2 (22%), respectively, as compared to that of pure α-Fe_2O_3. The IPCE results indicate a notable increase after double heterojunction, which aids in supporting the enhancement of the quantum efficiency of the α-Fe_2O_3/$BiVO_4$/MoS_2 photoanode, the significant reduction in the recombination rate, and the increase in the photocurrent density [43].

The charge carrier mobility is investigated in the pure α-Fe_2O_3, α-Fe_2O_3/$BiVO_4$, and α-Fe_2O_3/$BiVO_4$/MoS_2 photoanodes with the use of the Electrochemical Impedance Spectroscopy (EIS) analysis as shown in Fig. 4.2.7c. On the Nyquist diagram for pure α-Fe_2O_3, the impedance can be represented using the Randles model (inside of Fig. 4.2.7c). After fabricating the heterojunction, the α-Fe_2O_3/$BiVO_4$ and α-Fe_2O_3/$BiVO_4$/MoS_2 photoanodes changed to mixed kinetic and diffusion control circuit. The slope of the linear part in the impedance of the α-Fe_2O_3/$BiVO_4$ and α-Fe_2O_3/$BiVO_4$/MoS_2 photoanodes can be attributed to the diffusion inside the electrode. The lower slope of the linear part indicates more diffusion and high kinetics of metal ions inside of the electrodes. Based on the equivalent model, the values of the solution resistance and the charge transfer resistance at the bulk and interfaces for the α-Fe_2O_3/$BiVO_4$ and α-Fe_2O_3/$BiVO_4$/MoS_2 photoanodes were summarized at Table S2. The semicircle radius decreases in the following order: α-Fe_2O_3/$BiVO_4$/MoS_2 < α-Fe_2O_3/$BiVO_4$ < pure α-Fe_2O_3. A lower semicircle radius reveals a higher efficient charge carrier transport at the photoanode-electrolyte interface due to a lower charge transfer resistance or photo resistance [44]. Therefore, the heterojunction of the $BiVO_4$ and MoS_2 on the surface of the α-Fe_2O_3 was effective in improving the charge transfer by increasing interfacial charge transfer velocity with lower charge transfer resistance [45].

The Mott-Schottky (MS) curves of the α-Fe_2O_3, α-Fe_2O_3/$BiVO_4$, and α-Fe_2O_3/$BiVO_4$/MoS_2 are shown in Fig. 4.2.6f. The slope of the MS plot decreases significantly in the linear region which is attributed to the decreased depletion in the photoanodes after the double heterojunction. The MS analysis conducts for the estimation of the donor concentration (N_D), flat band potential (V_{fb}), and the length of depletion layer (W_{SCL}) for the prepared photoelectrodes. The α-Fe_2O_3/$BiVO_4$/MoS_2 electrode shows the highest donor concentration value (4.36E+26 m^3), the lowest flat band

potential (0.15 V), and the lowest depletion layer (W_{SCL}=2.96 nm) among the prepared electrodes. It also shows that the multi heterojunction decreased the recombination rate and facilitation of the hole transfer pathway to the electrode/electrolyte interface.

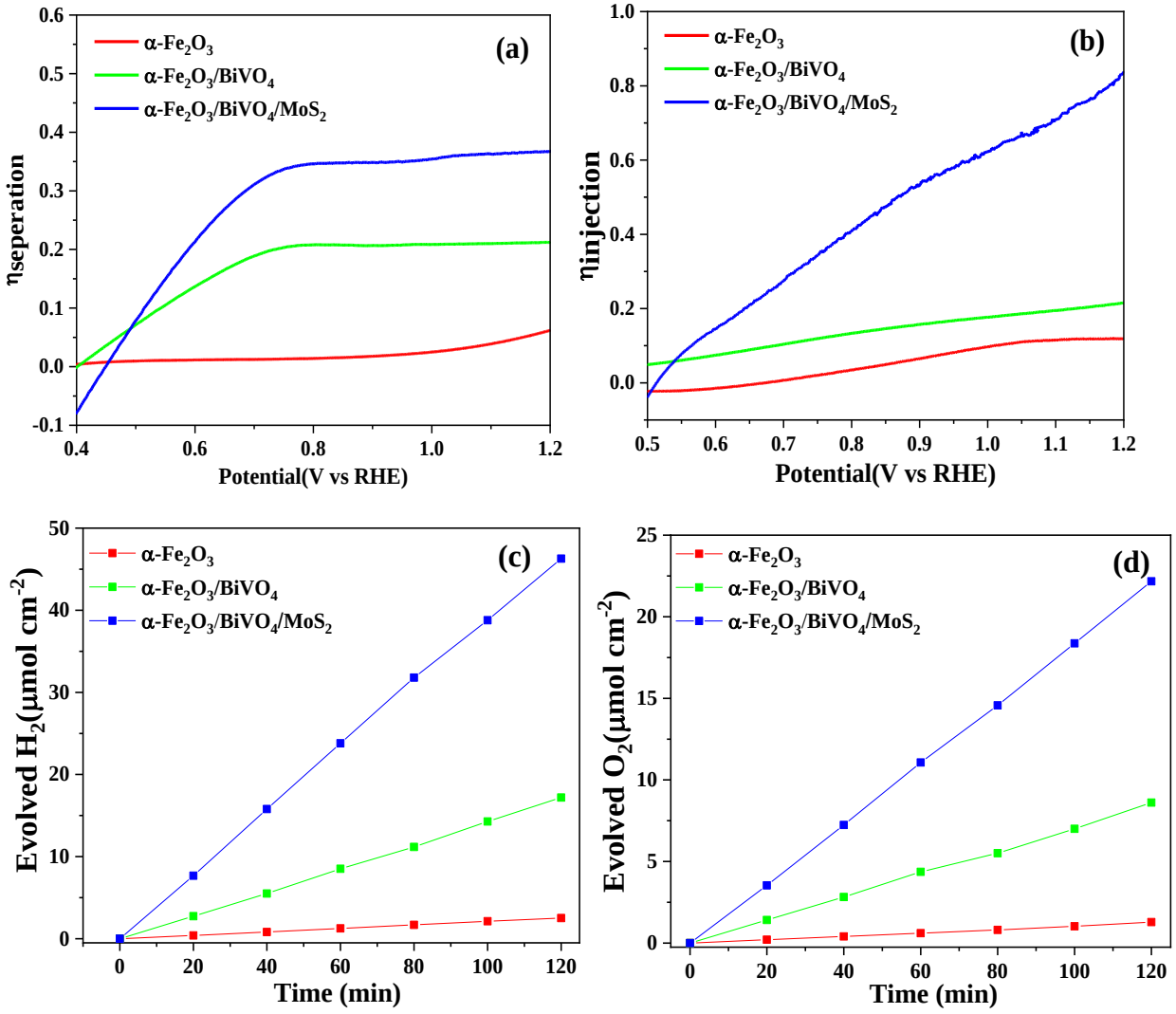

Fig. 4.2.8. (a) The charge separation, (b) charge injection efficiencies, (c) H_2, and (d) O_2 evolution vs. reaction time for α-Fe_2O_3, α-Fe_2O_3/$BiVO_4$, and α-Fe_2O_3/$BiVO_4$/MoS_2 photoanodes at a potential of 1.23 V versus RHE, under 100 mW/cm^2 irradiations, the electrolyte was a 0.5M aqueous solution of Na_2SO_4.

The modified α-Fe_2O_3/$BiVO_4$/MoS_2 photoelectrode overcame the reaction barrier and impressively improved the hole transport through the electrode/electrolyte interface. As shown in Fig. 4.2.8a, there is a significant enhancement in the photocurrent density an obvious shift in the

onset potential in the presence of H_2O_2 for α-Fe_2O_3, α-Fe_2O_3/$BiVO_4$, and α-Fe_2O_3/$BiVO_4$/MoS_2 photoelectrodes, mainly due to the faster oxidation kinetics [46]. The photocurrent commonly occurs through the light absorption of the semiconductor, the separation of the photogenerated charge carriers, and the surface charge injection for PEC performance. The charge separation efficiency (η_{sep}) and the surface charge injection efficiency (η_{inj}) of the pure α-Fe_2O_3, α-Fe_2O_3/$BiVO_4$, and α-Fe_2O_3/$BiVO_4$/MoS_2 photoanodes are shown in Figs. 4.2.8a and b, respectively. The values of η_{sep} and η_{inj} at 1.2 V vs. RHE for the pure α-Fe_2O_3, α-Fe_2O_3/$BiVO_4$, and α-Fe_2O_3/$BiVO_4$/MoS_2 electrodes were obviously enhanced through the fabrication of the double heterojunction.

In comparison, the overall water splitting of α-Fe_2O_3, α-Fe_2O_3/$BiVO_4$, and α-Fe_2O_3/$BiVO_4$/MoS_2 photoanodes were evaluated through the measurement of the H_2 and O_2 evolution at 1.23 V versus RHE under 100 mW/cm^2 irradiations in 0.5M of Na_2SO_4 electrolyte. Fig. 4.2.8c and d indicate the total H_2 values generated after 2 hours of irradiation for α-Fe_2O_3, α-Fe_2O_3/$BiVO_4$, and α-Fe_2O_3/$BiVO_4$/MoS_2 were determined 2.5, 17.2 and 46.5 μmol/cm^2, respectively, and the total O_2 generated are 1.55, 8.6, and 22.3 μmol/cm^2, respectively, indicating at 2:1 ratio in the water splitting reaction. In addition, the Faradaic efficiency of O_2 and H_2 evolution for Fe_2O_3/$BiVO_4$/MoS_2 photoanode was determined to be 80−83%, indicating that the majority of the photogenerated holes were used for the water oxidation reaction.

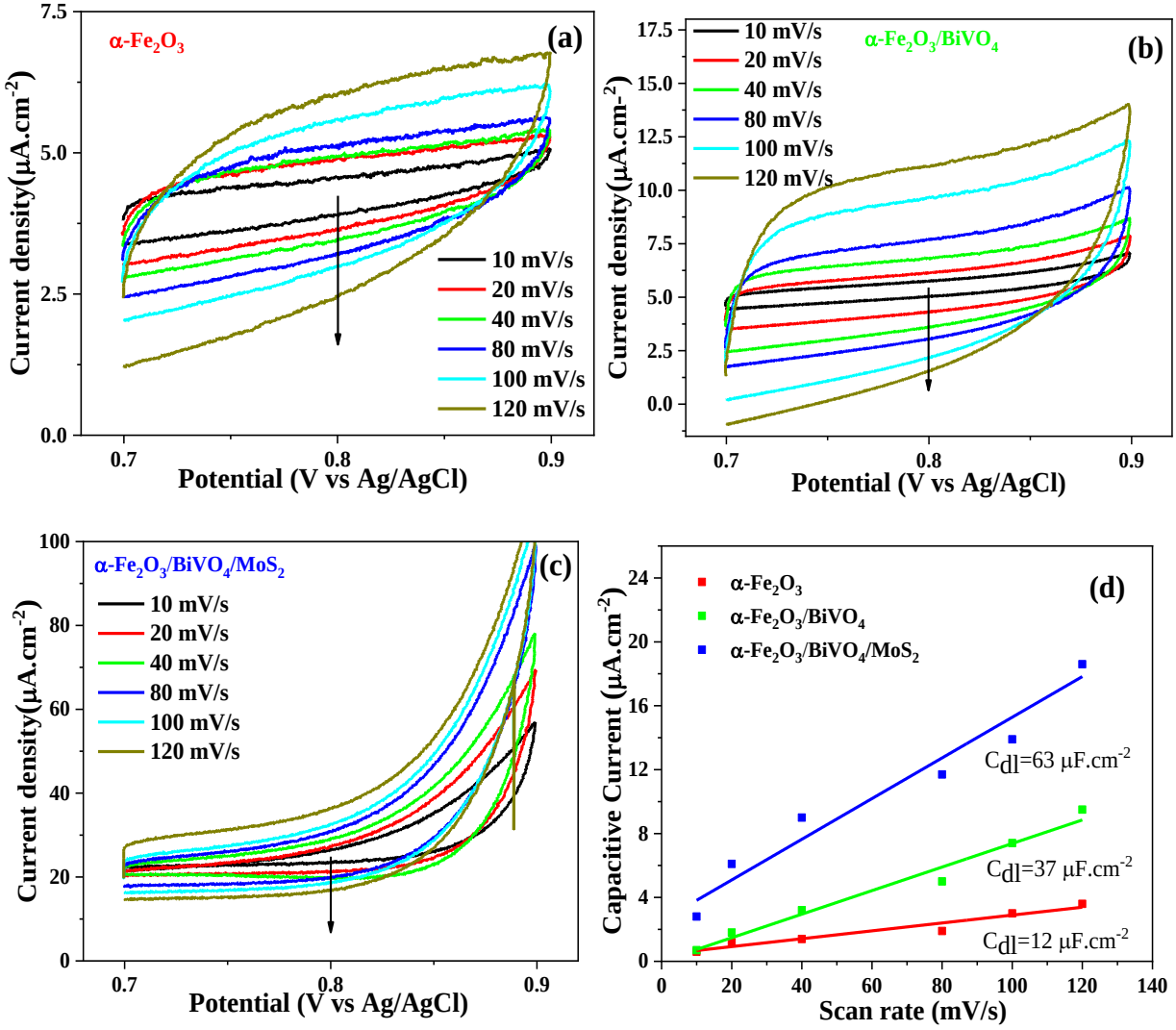

Fig. 4.2.9. Effective electrochemical active surface area tests (ECSA) of (a) α-Fe_2O_3, (b) α-Fe_2O_3/$BiVO_4$ and (c) α-Fe_2O_3/$BiVO_4$/MoS_2; (d) electrochemical double-layer capacity (C_{dl}) of α-Fe_2O_3, α-Fe_2O_3/$BiVO_4$ and α-Fe_2O_3/$BiVO_4$/MoS_2.

The relative electrochemical surface area (ECSA) of the α-Fe_2O_3, α-Fe_2O_3/$BiVO_4$ and α-Fe_2O_3/$BiVO_4$/MoS_2 samples was determined by the capacitive region of the cyclic voltammogram. As shown in Fig. 4.2.9a-c, cyclic voltammograms (CV) were carried out at scan rates of 10, 20, 40, 80, 100 and 120 mV/s in 0.5M Na_2SO_4 (pH≈7). The electrochemically active surface area was then determined by measuring the capacitive current associated with double layer charging from the scan rate dependence of the CV. The double layer capacitance (C_{dl}) was estimated from the

relationship between $\Delta J=(J_a-J_c)$ of Ag/AgCl at 0.8 V and different scan rates. The linear slope is equivalent to twice the C_{dl} and can be used to represent the ECSA (Fig. 4.2.9a-c). The double layer capacitance (C_{dl}) of α-Fe_2O_3/$BiVO_4$/MoS_2 is 63 μF cm^{-2}, which is higher than that of α-Fe_2O_3/$BiVO_4$ (37 μF cm^{-2}) and pure α-Fe_2O_3 (12 μF cm^{-2}). The plots in Fig. 4.2.9d show that the α-Fe_2O_3/$BiVO_4$/MoS_2 have a large active surface area, which can be attributed to the heterostructure with rich active edge sites [47].

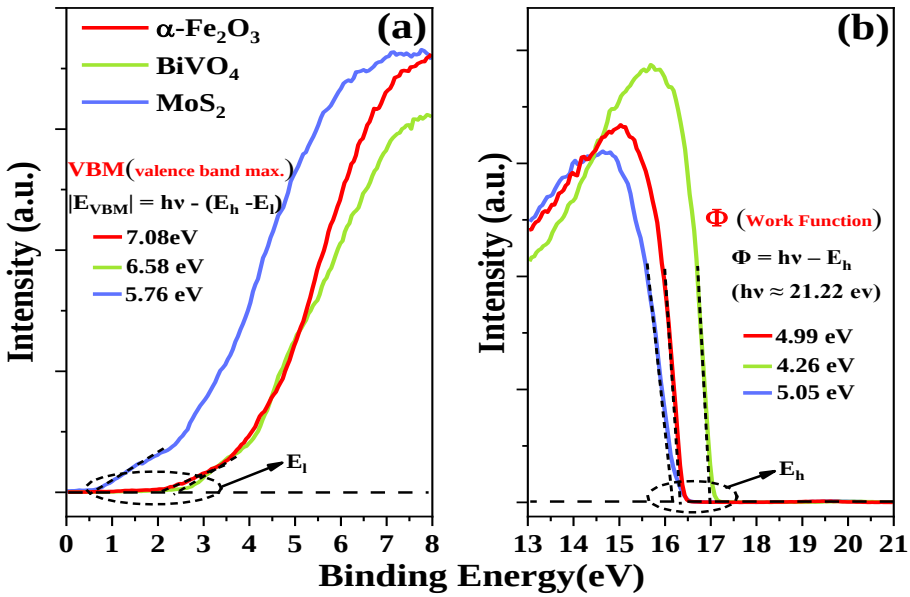

Fig. 4.2.10. UPS spectra for estimation of (a) valence band maximum and (b) work function for α-Fe_2O_3, $BiVO_4$ and MoS_2 photoelectrodes.

The ultraviolet photoelectron spectroscopy (UPS) spectra were measured to know how the bands line up at compositional junctions. Energies of the Fermi levels (E_F) and the valence band maximum (E_{VBM}) were estimated from UPS spectra shown in Figs. 4.2.10a and b. The work function (Φ) gives the energy of the Fermi level with respect to the vacuum level by subtracting the high cutoff (E_h) in UPS spectra from the excitation energy (hv) (Fig. 4.2.10b). The valence band energy (E_V) can be calculated by adding the low cutoff (E_L) in UPS spectra to the Φ value (Fig. 4.2.10a). These values are important for the determination of the semiconductor's junction

properties. The valence band energies (Ev) were 7.08, 6.58, and 5.76 eV for the α-Fe_2O_3, $BiVO_4$, and MoS_2, respectively. The conduction band energies (Ec) were estimated at 4.9, 4.12, and 3.84 eV from E_{VBM}-E_g for the α-Fe_2O_3, $BiVO_4$, and MoS_2 respectively.

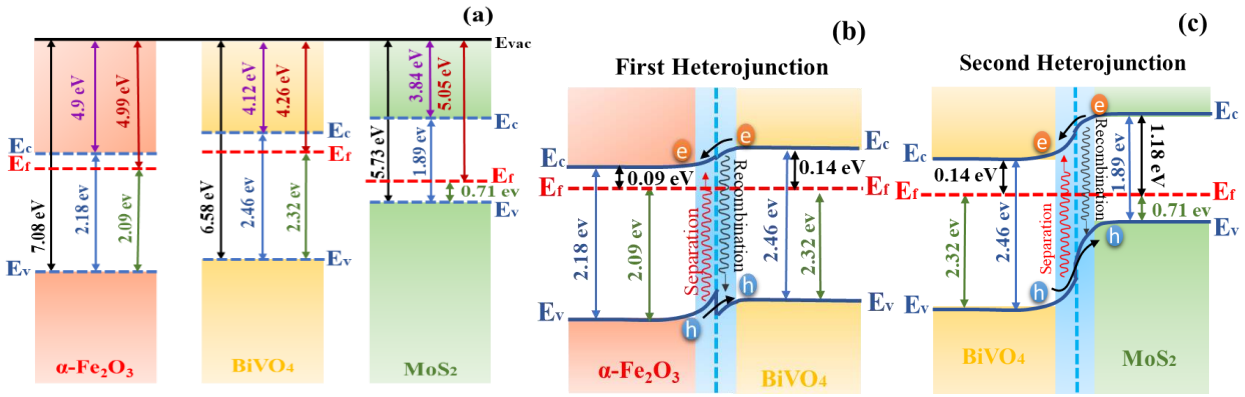

Fig. 4.2.11. A schematic illustration of the band alignment at (a) α-Fe_2O_3, $BiVO_4$, and MoS_2 before heterojunction and (b) after contact of the α-Fe_2O_3/$BiVO_4$ as a first heterojunction and (c) the $BiVO_4$/MoS_2 as a second heterojunction.

Suitable band alignment of the conduction band (CB) and valence band (VB) is required for effective photogeneration of the charge carriers. Obviously, before contact, there are separate Fermi levels for the semiconductors, but after they are in contact, the energy bands adjust to align the Fermi levels. In equilibrium, the final structure is characterized by a single Fermi level. Fig. 4.2.11a shows schematic illustration of the band alignment at the α-Fe_2O_3, $BiVO_4$, and MoS_2 before heterojunction. Figs. 4.2.11b and c show the junction of the α-Fe_2O_3 and the $BiVO_4$ as a first heterojunction and the junction of $BiVO_4$ and MoS_2 as a second heterojunction. The electron-hole pairs are generated in the semiconductors after visible light irradiation. Then, the electrons are transferred from the higher conduction band (CB) to the lower one and the holes are moved from the lower valence band (VB) to the higher valence band energy. The PEC efficiency in the pure α-Fe_2O_3 is very low due to the high recombination rate of charge carriers and short diffusion length. In the α-Fe_2O_3/$BiVO_4$ electrode, the recombination decreased due to the electron's movements from the CB of $BiVO_4$ to the CB of the α-Fe_2O_3 and the holes simultaneously transfer

from the VB of α-Fe_2O_3 to the VB of $BiVO_4$ [25]. After designing the multi heterojunction, the difference in energy levels makes electrons move from the CB of MoS_2 to the CB of $BiVO_4$ and then to the CB of α-Fe_2O_3 in the α-Fe_2O_3/$BiVO_4$/MoS_2 photoanode. The holes were driven by the electrostatic field from the VB of α-Fe_2O_3 to the VB of $BiVO_4$ and then to the VB of MoS_2 which occurs in the oxidation reaction on the surface of the photoanode. Thus, the construction of these heterojunctions can enhance the photogeneration of the charge carriers at the depletion layer and lead to higher PEC performance [48].

4.2.4. Conclusion

The heterojunction of α-Fe_2O_3 nanorod with $BiVO_4$ and MoS_2 nanosheets, were prepared using dip-coating and drop casting processes respectively and served to enhance the PEC performance. By loading the MoS_2 nanosheets as a 2D material onto the surface of the electrode, the highest photocurrent density was approached for the fabricated α-Fe_2O_3/$BiVO_4$/MoS_2 photoanode among all electrodes. The best photocurrent density was 7, and 15 times higher than those of the α-Fe_2O_3/$BiVO_4$ and pure α-Fe_2O_3 electrodes, respectively. The incident photon current efficiency (IPCE) and applied-bias photon-to-current conversion efficiency (ABPE) results indicated that the multi heterojunction of α-Fe_2O_3/$BiVO_4$/MoS_2 increased around 11 and 18.7 times compared to that of pure α-Fe_2O_3, respectively. The heterojunction of α-Fe_2O_3/$BiVO_4$ improved the efficiency of photo-generated electron-hole pairs and reduced the recombination rate due to the decrease in resistance and facilitated the hole transfer pathway. Furthermore, the exfoliated MoS_2 nanosheets were deposited on the surface of the α-Fe_2O_3/$BiVO_4$ photoelectrode, leading to increased light harvesting and the enhancement of electrical conductivity through heterojunction, mainly because of the improved efficient charge transport at the α-Fe_2O_3/$BiVO_4$/MoS_2 interfaces.

Reference:

[1] C. Guan, H. Wu, W. Ren, C. Yang, X. Liu, X. Ouyang, Z. Song, Y. Zhang, S.J. Pennycook, C. Cheng, J. Wang, Metal–organic framework-derived integrated nanoarrays for overall water splitting, Journal of Materials Chemistry A, 6 (2018) 9009-9018.
[2] B. Hui, J. Li, Y. Lu, K. Zhang, H. Chen, D. Yang, L. Cai, Z. Huang, Boosting electrocatalytic hydrogen generation by a renewable porous wood membrane decorated with Fe-doped NiP alloys, Journal of Energy Chemistry, 56 (2021) 23-33.
[3] V. Vinesh, M. Ashokkumar, B. Neppolian, rGO supported self-assembly of 2D nano sheet of (g-C3N4) into rod-like nano structure and its application in sonophotocatalytic degradation of an antibiotic, Ultrasonics Sonochemistry, 68 (2020) 105218.
[4] K. Dashtian, S. Shahbazi, M. Tayebi, Z. Masoumi, A review on metal-organic frameworks photoelectrochemistry: A headlight for future applications, Coord. Chem. Rev., 445 (2021) 214097.
[5] G. Kim, M. Oh, Y. Park, Solar-rechargeable battery based on photoelectrochemical water oxidation: Solar water battery, Scientific Reports, 6 (2016) 33400.
[6] M. Kolaei, M. Tayebi, Z. Masoumi, A. Tayyebi, B.-K. Lee, Decoration of CdS nanoparticles on dense and multi-edge sodium titanate nanorods to form a highly efficient and stable photoanode with great enhancement in PEC performance, Environmental Science: Nano, 8 (2021) 1667-1679.
[7] H. Yoo, D. Lee, J.H. Kim, High performance of TiO2/CuxO photoelectrodes for regenerative solar energy storage in a vanadium photoelectrochemical cell, Green Energy & Environment, (2020).
[8] S. Farhoosh, B. Eftekharinia, M. Tayebi, B.-K. Lee, N. Naseri, Newly designed ternary hematite-based heterojunction for PEC water splitting, Applied Surface Science, 550 (2021) 149374.
[9] M. Tayebi, A. Tayyebi, T. Soltani, B.-K. Lee, pH-Dependent photocatalytic performance of modified bismuth vanadate by bismuth ferrite, New Journal of Chemistry, 43 (2019) 9106-9115.
[10] K. Sivula, F. Le Formal, M. Grätzel, Solar Water Splitting: Progress Using Hematite (α-Fe2O3) Photoelectrodes, ChemSusChem, 4 (2011) 432-449.
[11] V. Vignal, R. Oltra, M. Verneau, L. Coudreuse, Influence of an elastic stress on the conductivity of passive films, Materials Science and Engineering: A, 303 (2001) 173-178.
[12] S. Gao, D. Wang, Y. Wang, C. Li, Y. Liu, N. Suzuki, C. Terashima, A. Fujishima, X. Zhang, Activating titanium dopants in hematite photoanode by rapid thermal annealing for enhancing photoelectrochemical water oxidation, Electrochimica Acta, 318 (2019) 746-753.
[13] Y. Xue, Y. Wang, A review of the α-Fe2O3 (hematite) nanotube structure: recent advances in synthesis, characterization, and applications, Nanoscale, 12 (2020) 10912-10932.
[14] S.-H. Chen, Y.-S. Jiang, H.-y. Lin, Easy Synthesis of BiVO4 for Photocatalytic Overall Water Splitting, ACS Omega, 5 (2020) 8927-8933.
[15] H.-J. Ahn, K.-Y. Yoon, M.-J. Kwak, J.-S. Lee, P. Thiyagarajan, J.-H. Jang, MoSx supported hematite with enhanced photoelectrochemical performance, Journal of Materials Chemistry A, 3 (2015) 21444-21450.
[16] X. Ma, Z. Ma, D. Lu, Q. Jiang, L. Li, T. Liao, B. Hou, Enhanced photoelectrochemical cathodic protection performance of MoS2/TiO2 nanocomposites for 304 stainless steel under visible light, Journal of Materials Science & Technology, 64 (2021) 21-28.
[17] A. Kudo, Y. Miseki, Heterogeneous photocatalyst materials for water splitting, Chemical Society Reviews, 38 (2009) 253-278.
[18] S.J.A. Moniz, S.A. Shevlin, D.J. Martin, Z.-X. Guo, J. Tang, Visible-light driven heterojunction photocatalysts for water splitting – a critical review, Energy & Environmental Science, 8 (2015) 731-759.
[19] H. Bai, X. Li, Y. Zhao, W. Fan, Y. Liu, Y. Gao, D. Xu, J. Ding, W. Shi, Fabrication of BiVO4-Ni/Co3O4 photoanode for enhanced photoelectrochemical water splitting, Applied Surface Science, 538 (2021) 148150.
[20] N. Kondekar, M.G. Boebinger, M. Tian, M.H. Kirmani, M.T. McDowell, The Effect of Nickel on MoS2 Growth Revealed with in Situ Transmission Electron Microscopy, ACS Nano, 13 (2019) 7117-7126.
[21] M. Tayebi, B.-K. Lee, The effects of W/Mo-co-doped BiVO4 photoanodes for improving photoelectrochemical water splitting performance, Catalysis Today, 361 (2021) 183-190.
[22] F.M. Pesci, M.S. Sokolikova, C. Grotta, P.C. Sherrell, F. Reale, K. Sharda, N. Ni, P. Palczynski, C. Mattevi, MoS2/WS2 Heterojunction for Photoelectrochemical Water Oxidation, ACS Catalysis, 7 (2017) 4990-4998.
[23] Z. Masoumi, M. Tayebi, B.-K. Lee, Ultrasonication-assisted liquid-phase exfoliation enhances photoelectrochemical performance in α-Fe2O3/MoS2 photoanode, Ultrasonics Sonochemistry, 72 (2021) 105403.

[24] B. Adilbekova, Y. Lin, E. Yengel, H. Faber, G. Harrison, Y. Firdaus, A. El-Labban, D.H. Anjum, V. Tung, T.D. Anthopoulos, Liquid phase exfoliation of MoS2 and WS2 in aqueous ammonia and their application in highly efficient organic solar cells, Journal of Materials Chemistry C, 8 (2020) 5259-5264.
[25] S. Bai, H. Chu, X. Xiang, R. Luo, J. He, A. Chen, Fabricating of Fe2O3/BiVO4 heterojunction based photoanode modified with NiFe-LDH nanosheets for efficient solar water splitting, Chemical Engineering Journal, 350 (2018) 148-156.
[26] S.S.M. Bhat, S.A. Pawar, D. Potphode, C.-K. Moon, J.M. Suh, C. Kim, S. Choi, D.S. Patil, J.-J. Kim, J.C. Shin, H.W. Jang, Substantially enhanced photoelectrochemical performance of TiO2 nanorods/CdS nanocrystals heterojunction photoanode decorated with MoS2 nanosheets, Applied Catalysis B: Environmental, 259 (2019) 118102.
[27] M. Tayebi, Z. Masoumi, B.-K. Lee, Ultrasonically prepared photocatalyst of W/WO3 nanoplates with WS2 nanosheets as 2D material for improving photoelectrochemical water splitting, Ultrasonics Sonochemistry, 70 (2021) 105339.
[28] L. Yu, Y. Zhang, J. He, H. Zhu, X. Zhou, M. Li, Q. Yang, F. Xu, Enhanced photoelectrochemical properties of α-Fe2O3 nanoarrays for water splitting, Journal of Alloys and Compounds, 753 (2018) 601-606.
[29] M. Padervand, B. Rhimi, C. Wang, One-pot synthesis of novel ternary Fe3N/Fe2O3/C3N4 photocatalyst for efficient removal of rhodamine B and CO2 reduction, Journal of Alloys and Compounds, 852 (2021) 156955.
[30] T. Zhang, H. Zhang, Y. Ji, N. Chi, Y. Cong, Preparation of a novel Fe2O3-MoS2-CdS ternary composite film and its photoelectrocatalytic performance, Electrochimica Acta, 285 (2018) 230-240.
[31] L. Xia, J. Bai, J. Li, Q. Zeng, L. Li, B. Zhou, High-performance BiVO4 photoanodes cocatalyzed with an ultrathin α-Fe2O3 layer for photoelectrochemical application, Applied Catalysis B: Environmental, 204 (2017) 127-133.
[32] T. Soltani, A. Tayyebi, B.-K. Lee, Efficient promotion of charge separation with reduced graphene oxide (rGO) in BiVO4/rGO photoanode for greatly enhanced photoelectrochemical water splitting, Sol. Energy Mater. Sol. Cells, 185 (2018) 325-332.
[33] M. Tayebi, A. Tayyebi, B.-K. Lee, Photocharged molybdenum-doped BiVO4 photoanodes for simultaneous enhancements in charge transport and surface passivation, Solar Energy, 191 (2019) 427-434.
[34] J.-I. Park, Y. Jang, J.-S. Bae, J.-H. Yoon, H.U. Lee, Y. Wakayama, J.-P. Kim, Y. Jeong, Effect of thickness-dependent structural defects on electrical stability of MoS2 thin film transistors, Journal of Alloys and Compounds, 814 (2020) 152134.
[35] X. Fan, Y. Zhou, G. Zhang, T. Liu, W. Dong, In situ photoelectrochemical activation of sulfite by MoS2 photoanode for enhanced removal of ammonium nitrogen from wastewater, Applied Catalysis B: Environmental, 244 (2019) 396-406.
[36] A.A. Bortoti, A. de Freitas Gavanski, Y.R. Velazquez, A. Galli, E.G. de Castro, Facile and low cost oxidative conversion of MoS2 in α-MoO3: Synthesis, characterization and application, Journal of Solid State Chemistry, 252 (2017) 111-118.
[37] C. Dai, X. Tian, S. Feng, Y. Nie, Y. Li, L. Lu, Insight into bicarbonate involved efficient heterogeneous Fenton-like degradation of sulfamethoxazole over a CuFeO2 based composite under alkaline conditions, Environmental Science: Nano, (2021).
[38] G. Wang, X. Xie, X. Cui, J. Liu, L. Jiang, Photoinduced Pt/BiVO4/Bi2O3 Heterostructures for Methanol Oxidation and New Insights on the Photo-/Electrocatalysis Coupling Mechanism, ACS Sustainable Chemistry & Engineering, 9 (2021) 4271-4281.
[39] Z. Shi, Y. Zhang, G. Duoerkun, W. Cao, T. Liu, L. Zhang, J. Liu, M. Li, Z. Chen, Fabrication of MoS2/BiOBr heterojunctions on carbon fibers as a weaveable photocatalyst for tetracycline hydrochloride degradation and Cr(vi) reduction under visible light, Environmental Science: Nano, 7 (2020) 2708-2722.
[40] Y. Zheng, X. Zhang, J. Zhao, P. Yang, Assembled fabrication of α-Fe2O3/BiOCl heterojunctions with enhanced photocatalytic performance, Applied Surface Science, 430 (2018) 585-594.
[41] S. Ju, J. Jun, S. Son, J. Park, H. Lim, W. Kim, D. Chae, H. Lee, Structured BiVO4 Photoanode Fabricated via Sputtering for Large Areas and Enhanced Photoelectrochemical Performance, ACS Sustainable Chemistry & Engineering, 8 (2020) 17923-17932.
[42] H. Zhang, H. Wang, J. Xuan, Rational design of photoelectrochemical cells towards bias-free water splitting: Thermodynamic and kinetic insights, Journal of Power Sources, 462 (2020) 228113.
[43] R. Yalavarthi, R. Zbořil, P. Schmuki, A. Naldoni, Š. Kment, Elucidating the role of surface states of BiVO4 with Mo doping and a CoOOH co-catalyst for photoelectrochemical water splitting, Journal of Power Sources, 483 (2021) 229080.
[44] A. Ahmad, F. Tezcan, G. Yerlikaya, R. Zia ur, H. Paksoy, G. Kardaş, Three dimensional rosette-rod TiO2/Bi2S3 heterojunction for enhanced photoelectrochemical water splitting, Journal of Alloys and Compounds, 868 (2021)

159133.
[45] J.H. Kim, J.-W. Jang, Y.H. Jo, F.F. Abdi, Y.H. Lee, R. Van De Krol, J.S. Lee, Hetero-type dual photoanodes for unbiased solar water splitting with extended light harvesting, Nature communications, 7 (2016) 1-9.
[46] P.S. Bassi, R.P. Antony, P.P. Boix, Y. Fang, J. Barber, L.H. Wong, Crystalline Fe2O3/Fe2TiO5 heterojunction nanorods with efficient charge separation and hole injection as photoanode for solar water oxidation, Nano Energy, 22 (2016) 310-318.
[47] H. She, P. Yue, X. Ma, J. Huang, L. Wang, Q. Wang, Fabrication of BiVO4 photoanode cocatalyzed with NiCo-layered double hydroxide for enhanced photoactivity of water oxidation, Applied Catalysis B: Environmental, 263 (2020) 118280.
[48] A. Iqbal, K.H. Bevan, The impact of boundary conditions on calculated photovoltages and photocurrents at photocatalytic interfaces, MRS Communications, 8 (2018) 466-473.

Chapter 5- Conclusion

5.1. Summary

Solar water-splitting is a promising approach to produce sustainable clean fuels, with high theoretical efficiencies for converting solar energy to a dense, portable chemical energy form. To date, the achieved efficiencies of water-splitting by semiconductor-based photoelectrochemical cells have been still lower than those needed in a practical device, due to either a lack of suitable candidate materials, or stability limitations under harsh reaction conditions. Among the various water splitting photoanode materials, hematite (a-Fe_2O_3) has several promising properties, including a smaller band gap (1.9–2.2 eV) that maximizes absorption of the solar spectrum, stability in an aqueous environment under typical operating conditions, abundance, and affordability. Therefore, it is the best candidate for the proof-of-concept demonstrations for use as a practical water splitting photocatalyst. However, to date the maximum solar-to-hydrogen efficiency (STH) of hematite achieved is nearly 5%, which is by far from its theoretical STH (15.3, at the band gap of 2.1 eV).

In this thesis, we have critically discussed the factors that limit the water splitting efficiency of hematite and various approaches used to overcome the limitations. We discussed four different approaches to minimize the oxygen evolution overpotential, using metal doping, Z-scheme heterojunction with TMDs as a 2D semiconductor materials, using doping-heterojunction and using multi-heterojunction techniques. The PEC performances of doped hematite thin films were measured under the same synthetic and measurement condition. In the first section of chapter one, the optimum doping percentage of Mo, 10% Mo-α-Fe_2O_3 electrode with drop casting process, showed greatly improved PEC performance, which comprised 10-fold higher photocurrent density

than that of pure α-Fe_2O_3. Furthermore, optimizing the atomic percentage of W for doping is described in the second section of chapter one in the same conditions. The optimum 0.5W:α-Fe_2O_3 photoanode exhibited the greatest improvement in the PEC performance, at about 7-fold higher than that of pure α-Fe_2O_3 (0.5 mA.cm^{-2} at 1.23 V vs. RHE), which demonstrated its significant light-harvesting and charge transport characteristics. Samples doped with Mo and W elements were further investigated for their morphological and electronic properties. The result showed that the doping greatly improves photocurrent, decreases the resistance, and generates more charge carriers.

Z-scheme heterojunction systems based on multi-step photoexcitation liberate the semiconducting materials from thermodynamic limitations and enable the application of a variety of materials to water splitting. The heterojunction of α-Fe_2O_3 with exfoliated two-dimensional MoS_2 and WS_2 nanosheets, prepared through the ultrasonication process showed an improved PEC performance caused by the facile electron-hole transfer due to the formation of an electrostatic field. The optimized α-Fe_2O_3/MoS_2 with a thin 8-MoS_2 layer (3.3 nm thickness), labeled α-Fe_2O_3/8-MoS_2, showed photocurrent densities of 0.86 and 1.52 mA.cm^{-2} at 0.6 V (vs. Ag/AgCl) in front- and back-side illumination, respectively, which were 7.85 and 13.81 times higher than those of pure α-Fe_2O_3, respectively. Further, the optimum heterojunction with WS_2 (α-Fe_2O_3@4WS_2/WO_x) photoanode had a photocurrent density of 0.98 and 2.1 mA.cm^{-2} (with lowest onset potential 0.45 and 0.38 V vs. RHE) in front and back-side illumination, respectively at 1.23 V vs. RHE under 100 mW.cm^{-2} which are ~ 13 and 30 times higher than that of the α-Fe_2O_3 photoanode. The efficient and stable PEC water splitting of the α-Fe_2O_3 heterojunction with TMDs was greatly enhanced, due to the increased efficiency of photogenerated charge carriers, facile hole extraction through the optimum shell heterojunction, and the reduced resistance caused by the decreased recombination rate of the

electron-hole pairs.

The combination of the heterojunction and metal doping on the pure α-Fe_2O_3 increased its donor concentration, reduced the space charge layer, and decreased the flat band potential, which could all have contributed to the improved photoelectrochemical efficiency. The optimized incorporation of 0.5%W doping and 2D nanosheets of MoS_2 (0.5W:α-Fe_2O_3/MoS_2 photoanode) showed IPCE of 37% and ABPE 26% at 0.96 V vs. RHE, which are around 5.2 and 13 times higher than those of 0.5W:α-$Fe_2O_3$and pure α-Fe_2O_3, respectively.

In the last technique, the forming of multicomponent heterojunctions can therefore facilitate the separation and transportation of charge carriers. Furthermore, the heterojunction of semiconductors can enhance the efficiency of electron-hole separation by increasing the kinetics of charge carriers. Therefore, charge carriers are generated in one photocatalyst and then transferred vectorially to the other material through an offset in the energies of the conduction and valance band edges, thereby allowing for interfacial charge transfer from one semiconductor to another. The multi heterojunction of α-Fe_2O_3 nanorod with monoclinic $BiVO_4$ and MoS_2 nanosheets, were prepared through dip-coating and drop casting processes respectively and served to enhance photocurrent density 7, and 15 times higher than those of the α-Fe_2O_3/$BiVO_4$ and pure α-Fe_2O_3 electrodes, respectively. Moreover, the incident photon current efficiency (IPCE) and applied-bias photon-to-current conversion efficiency (ABPE) results indicated that the multi heterojunction of α-Fe_2O_3/$BiVO_4$/MoS_2 increased around 11 and 18.7 times compared to that of pure α-Fe_2O_3, respectively.

Photocatalytic and photoelectrochemical water splitting under irradiation by sunlight has received much attention for production of renewable hydrogen from water on a large scale. Many challenges

remain in improving energy conversion efficiency yet, such as utilizing longer-wavelength photons for hydrogen production, enhancing the reaction efficiency at any given wavelength, and increasing the lifetime of the semiconductor materials. Researchers working on semiconductor materials and catalysts for water splitting are responsible for achieving adequate performance in solar to hydrogen conversion, because there are also many challenges in separation, purification, transportation, and utilization of solar hydrogen fuel as well as in scale-up. All the above-mentioned research fields are essential to establish a sustainable society based on solar hydrogen.

5.2. Future work

Future directions in PEC water splitting are myriad and there are many opportunities to discover cost-effective methods for the conversion of solar energy to chemical energy. Although an emerging trend in water splitting is the development of nanostructured photoelectrodes, the full potential of nanostructures can only be achieved when the limitations of a specific material are accounted for, such as high recombination rates or poor charge transport. Therefore, works on materials to prepare photoelectrodes with the proper PEC performance is the priority for other steps. The material such as: Semiconductor Materials ($BiVO_4$, Ta_3N_5 , and Fe_2TiO_5) and 2D materials (graphene, boron nitride, and MAX phases nanosheets).

Upgrading the photocatalytic efficiency to the required level while using narrow bandgap photocatalysts consisting of inexpensive and abundant elements will be challenging, given our present level of knowledge and technology. More advanced material designs are needed, ideally in conjunction with breakthrough discoveries stemming from a broad range of research areas. Therefore, it is our sincere hope that collaborations in this exciting research field will speed the adoption of this technology on an industrial scale.

Publications and conference

List of publication

1. First Author

[1] **Zohreh Masoumi[1]**, Meysam Tayebi[1], Byeong-Kyu Lee[1,*]. The role of doping molybdenum (Mo) and back-front side illumination in enhancing the charge separation of α-Fe_2O_3 nanorod photoanode for solar water splitting. **Solar Energy** 205 (2020) 126–134, **(IF:5.742).** https://doi.org/10.1016/j.solener.2020.05.044

[2] **Zohreh Masoumi[1]**, Meysam Tayebi[1], Byeong-Kyu Lee[1,*]. Study effect of sonochemical assisted synthesis of MoS_2 nanosheets on α-Fe_2O_3 photoanode for enhancing photoelectrochemical water splitting, **Ultrasonic-Sonochemistry**, 72 (2021) 105403, **(IF:7.491).** https://doi.org/10.1016/j.ultsonch.2020.105403

[3] **Zohreh Masoumi[1],** Meysam Tayebi[1], Morteza Kolaei[1], Ahmad Tayyebi[2], Hongsun Ryu[3] and Joon I. Jang[3], Byeong-Kyu Lee[1,*] Simultaneous Enhancement of Charge Separation and Hole Transportation in a W:α-Fe_2O_3/MoS_2 Photoanode: The Collaborative Approach of MoS_2 as a Heterojunction and W as Metal Doping, **ACS Appl. Mater. Interfaces**, 2021, 13, 39215−39229, **(IF: 9.229).** https://doi.org/10.1021/acsami.1c08139

[4] **Zohreh Masoumi[1],** Meysam Tayebi[1], Morteza Kolaei[1], Byeong-Kyu Lee*. Unified surface modification by double heterojunction of MoS_2 nanosheets and $BiVO_4$ nanoparticles to enhance the photoelectrochemical water splitting of hematite photoanode. **Journal of Alloys and Compounds, (IF:5.316).** https://doi.org/10.1016/j.jallcom.2021.161802

2. Co-Author:

[1] Meysam Tayebi; Morteza Kolaei; Ahmad Tayyebi; **Zohreh Masoumi**; Zeynab Belbasi; Byeong-Kyu Lee*. Reduced Graphene Oxide (RGO) on TiO_2 for an Improved Photoelectrochemical (PEC) and Photocatalytic activity. **Solar Energy** 190 (2019) 185–194, (**IF:5.170**). https://doi.org/10.1016/j.solener.2019.08.020

[2] Meysam Tayebi, Ahmad Tayyebi, **Zohreh Masoumi**, Byeong-Kyu Lee*. Photo corrosion Suppression and Photoelectrochemical (PEC) Enhancement of ZnO via Hybridization with Graphene Nanosheets. **Applied Surface Science,** 502 (2020) 1441892, (**IF:6.707**). https://doi.org/10.1016/j.apsusc.2019.144189

[3] Meysam Tayebi, **Zohreh Masoumi,** Byeong-Kyu Lee*. Ultrasonically prepared photocatalyst of W/WO_3 nanoplates with WS_2 nanosheets as 2D material for improving photoelectrochemical water splitting **Ultrasonic-Sonochemistry.** Volume 70, January 2021, 105339, (**IF:7.630**). https://doi.org/10.1016/j.ultsonch.2020.105339

[4] Morteza Kolaei, Meysam Tayebi, **Zohreh Masoumi**, Byeong-Kyu Lee*. Decoration of CdS nanoparticle on dense and multi edge sodium titanate nanorods to form a highly efficient and stable photoanode with great enhancement in PEC performance, ***Environ. Sci.: Nano***, 2021,8, 1667-1679, (**IF: 8.131**). https://doi.org/10.1039/D1EN00221J

Solar Energy 205 (2020) 126–134

Contents lists available at ScienceDirect

Solar Energy

journal homepage: www.elsevier.com/locate/solener

The role of doping molybdenum (Mo) and back-front side illumination in enhancing the charge separation of α-Fe_2O_3 nanorod photoanode for solar water splitting

Zohreh Masoumi, Meysam Tayebi, Byeong-Kyu Lee*

Department of Civil and Environment Engineering, University of Ulsan, Daehakro 93, Namgu, Ulsan 44610, Republic of Korea

Ultrasonics Sonochemistry 72 (2021) 105403

Contents lists available at ScienceDirect

Ultrasonics Sonochemistry

journal homepage: www.elsevier.com/locate/ultson

Ultrasonication-assisted liquid-phase exfoliation enhances photoelectrochemical performance in α-Fe_2O_3/MoS_2 photoanode

Zohreh Masoumi, Meysam Tayebi , Byeong-Kyu Lee *

Department of Civil and Environment Engineering, University of Ulsan, Daehakro 93, Namgu, Ulsan 44610, Republic of Korea

ACS APPLIED MATERIALS & INTERFACES

www.acsami.org Research Article

Simultaneous Enhancement of Charge Separation and Hole Transportation in a W:α-Fe_2O_3/MoS_2 Photoanode: A Collaborative Approach of MoS_2 as a Heterojunction and W as a Metal Dopant

Zohreh Masoumi, Meysam Tayebi, Morteza Kolaei, Ahmad Tayyebi, Hongsun Ryu, Joon I. Jang, and Byeong-Kyu Lee*

Cite This: *ACS Appl. Mater. Interfaces* 2021, 13, 39215–39229 Read Online

Journal of Alloys and Compounds 890 (2021) 161802

Contents lists available at ScienceDirect

Journal of Alloys and Compounds

journal homepage: www.elsevier.com/locate/jalcom

Unified surface modification by double heterojunction of MoS_2 nanosheets and $BiVO_4$ nanoparticles to enhance the photoelectrochemical water splitting of hematite photoanode

Zohreh Masoumi, Meysam Tayebi , Morteza Kolaei, Byeong-Kyu Lee*

Department of Civil and Environment Engineering, University of Ulsan, Daehakro 93, Namgu, Ulsan 44610, Republic of Korea

List of conference:

[1] **Zohreh Masoumi**, Meysam Tayebi, Byeong-Kyu Lee. Mo-$BiVO_4$/Fe_2TiO_5 Heterojunction Photoanodes for Improving Photoelectrochemical Water Splitting Performance. The 6th International Conference on New Photocatalytic Materials for Environment, Energy and Sustainability (NPM-5), Oral presentation, May.27.2021 Hungary.

[2] **Zohreh Masoumi**, Meysam Tayebi, Byeong-Kyu Lee. Simultaneous Enhancement of light harvesting and Charge Separation in α-Fe_2O_3 Nanorod: A Collaborative Approach of MoS_2 as 2D material and $BiVO_4$ as Heterojunction. 6th International Conference on Nanoscience and Nanotechnology (ICONN 2021), Oral presentation, Feb. 1.3, 2021, SRM Institute of Science and Technology, India.

[3] **Zohreh Masoumi**, Meysam Tayebi, Byeong-Kyu Lee. W Doped α-Fe_2O_3 Heterojunction with MoS_2 Nanosheet for Improving Photoelectrochemical Performance. 4th International Conference on Bioresources, Energy, Environment, and Materials Technology (BEEM 2020), Oral presentation, Sep 6-9, 2020, Incheon, Korea.

[4] **Zohreh Masoumi**, Meysam Tayebi, Byeong-Kyu Lee. Enhancement of photoelectrochemical performance of α-Fe_2O_3/$BiVO_4$ heterojunction based photoanode with 2D material nanosheets for efficient solar water splitting. Korean Society of Environmental Engineers IEEC & BWR 2019, poster presentation, Dec 10-13, 2019, Busan, Korea.

[5] **Zohreh Masoumi**, Byeong-Kyu Lee. Improvement of photoelectrochemical performance of Hematite (α-Fe_2O_3) nanorod electrode by MoS_2 and WS_2 heterojunction. Korean Society for Atmospheric Environment (KOSAE) 2019, Oral presentation, Nov 7-9, 2019, Changwon, Korea.

[6] **Zohreh Masoumi**, Meysam Tayebi, Byeong-Kyu Lee. Enhancement of photoelectrochemical performance of Hematite (α-Fe_2O_3) nanorod electrode by heterojunction 2D material. Asia-Oceanic Sonochemical Society Conference (AOSS4), Oral presentation, Sep 19-21, 2019, Nanjing, China.

[7] **Zohreh Masoumi**, Byeong-Kyu Lee. Enhancement of photoelectrochemical performance of Hematite (α-Fe_2O_3) nanorod electrode by doping Molybdenum. International Conference on Photocatalysis and Photoenergy 2019, Oral presentation, May 22-25, 2019, Incheon, Korea.